

THE RADIO CONTINUUM–STAR FORMATION RATE RELATION IN WSRT SINGS GALAXIES

VOLKER HEESSEN^{1,2}, ELIAS BRINKS¹, ADAM K. LEROY³, GEORGE HEALD⁴, ROBERT BRAUN⁵, FRANK BIGIEL⁶,
AND RAINER BECK⁷

(Dated: Received 2013 August 1 / accepted 2014 February 4)
Draft version April 7, 2014

ABSTRACT

We present a study of the spatially resolved radio continuum–star formation rate (RC–SFR) relation using state-of-the-art star formation tracers in a sample of 17 THINGS galaxies. We use SFR surface density (Σ_{SFR}) maps created by a linear combination of *GALEX* far-UV (FUV) and *Spitzer* 24 μm maps. We use RC maps at $\lambda\lambda$ 22 and 18 cm from the WSRT SINGS survey and H α emission maps to correct for thermal RC emission. We compare azimuthally averaged radial profiles of the RC and FUV/mid-IR (MIR) based Σ_{SFR} maps and study pixel-by-pixel correlations at fixed linear scales of 1.2 and 0.7 kpc. The ratio of the integrated SFRs from the RC emission to that of the FUV/MIR-based SF tracers is $\mathcal{R}_{\text{int}} = 0.78 \pm 0.38$, consistent with the relation by Condon. We find a tight correlation between the radial profiles of the radio and FUV/MIR-based Σ_{SFR} for the entire extent of the disk. The ratio \mathcal{R} of the azimuthally averaged radio to FUV/MIR-based Σ_{SFR} agrees with the integrated ratio and has only quasi-random fluctuations with galactocentric radius that are relatively small (25%). Pixel-by-pixel plots show a tight correlation in log-log diagrams of radio to FUV/MIR-based Σ_{SFR} , with a typical standard deviation of a factor of two. Averaged over our sample we find $(\Sigma_{\text{SFR}})_{\text{RC}} \propto (\Sigma_{\text{SFR}})_{\text{hyb}}^{0.63 \pm 0.25}$, implying that data points with high Σ_{SFR} are relatively radio dim, whereas the reverse is true for low Σ_{SFR} . We interpret this as a result of spectral aging of cosmic-ray electrons (CREs), which are diffusing away from the star formation sites where they are injected into the interstellar medium. This is supported by our finding that the radio spectral index is a second parameter in pixel-by-pixel plots: those data points dominated by young CREs are relatively radio dim, while those dominated by old CREs are slightly more RC bright than what would be expected from a linear extrapolation. We studied the ratio \mathcal{R} of radio to FUV/MIR-based integrated SFR as a function of global galaxy parameters and found no clear correlation. This suggests that we can use RC emission as a universal star formation tracer for galaxies with a similar degree of accuracy as other tracers, if we restrict ourselves to global or azimuthally averaged measurements. We can reconcile our finding of an almost linear RC–SFR relation and sub-linear resolved (on 1 kpc scale) RC– Σ_{SFR} relation by proposing a non-linear magnetic field–SFR relation, $B \propto \text{SFR}_{\text{hyb}}^{0.30 \pm 0.02}$, which holds both globally and locally.

Keywords: cosmic rays – galaxies: fundamental parameters – galaxies: ISM – galaxies: magnetic fields – galaxies: star formation – galaxies: structure

1. INTRODUCTION

Radio continuum (RC) emission in galaxies stems from massive stars, allowing us to use it as a star formation (SF) tracer. Ionizing UV radiation from massive stars creates H II regions where thermal electrons give rise to RC radiation through the process of *bremsstrahlung* or thermal (free–free) emission. These same stars, upon reaching the end of their lives, are the source of cosmic-ray electrons (CREs) that are accelerated in supernova shock waves. When these CREs encounter a magnetic field, they generate non-thermal (synchrotron) emission. If all CREs lose their energy exclusively *within* the galaxy, it can be considered a *calorimeter* (Völk

1989; Lisenfeld et al. 1996). More realistically, a galaxy is a leaky box, and models become far more involved (Bell 2003; Lacki et al. 2010). The relative success of theoretical models lends confidence that massive SF and RC emission are indeed closely tied together.

RC can act as tracers for the star formation rate (SFR) with the added advantage over other tracers—such as the optical Balmer H α line emission, far-UV (FUV) emission as measured by the *GALEX* satellite, and hybrid combination of these (e.g., Leroy et al. 2012)—that they are unaffected by dust attenuation. The advantage offered by probing SF via radio astronomical means is that this does not rely on the availability of (cryogenically cooled) IR satellites. The motivation of this paper is to deepen our understanding of the relation between the SFR and the RC luminosity of normal star-forming galaxies, hereafter the RC–SFR relation, as originally explored by Condon (1992).

RC emission observed at 33 GHz is an almost ideal SF tracer (Murphy et al. 2011). The reason is that thermal free–free emission is the dominating emission mechanism in the 20–40 GHz range. However, galaxies can be a factor of 10 brighter at lower frequencies such as between 1 and 2 GHz than at 33 GHz, where the non-thermal emission dominates. This frequency range is hence potentially more valuable, especially for cosmological studies. For this to work, the non-

¹ Centre for Astrophysics Research, University of Hertfordshire, Hatfield AL10 9AB, UK; e.brinks@herts.ac.uk

² School of Physics & Astronomy, University of Southampton, Southampton SO17 1BJ, UK; v.heesen@soton.ac.uk

³ National Radio Astronomy Observatory, 520 Edgemont Road, Charlottesville, VA 22903-2475, USA; aleroy@nrao.edu

⁴ Netherlands Institute for Radio Astronomy (ASTRON), Postbus 2, 7990 AA Dwingeloo, The Netherlands; heald@astron.nl

⁵ CSIRO Astronomy and Space Science, P.O. Box 76, Epping, NSW 1710, Australia; Robert.Braun@csiro.au

⁶ Institut für theoretische Astrophysik, Zentrum für Astronomie der Universität Heidelberg, Albert-Ueberle-Str. 2, D-69120 Heidelberg, Germany; bigiel@uni-heidelberg.de

⁷ Max-Planck-Institut für Radioastronomie, Auf dem Hügel 69, D-53121 Bonn, Germany; rbeck@mpifr-bonn.mpg.de

thermal component needs to be calibrated as successfully as the thermal RC against other SF indicators (see Kennicutt & Evans 2012, for a recent review of SF tracers). A properly calibrated RC–SFR for non-thermal continuum emission would offer a powerful method to probe the cosmic SFR, initially with the Very Large Array (VLA) and with Square Kilometre Array (SKA) precursors, and eventually with the SKA (e.g., Murphy 2009; Lacki & Thompson 2010). At the highest redshifts inverse Compton losses could dominate to such an extent that only the (weaker) thermal RC is expected to survive, although opinion on this remains divided (e.g., Murphy 2009; Lacki & Thompson 2010; Schleicher & Beck 2013).

A semi-empirical model was introduced by Condon (1992) to quantify the RC–SFR relation. It assumes that the RC luminosity is proportional to the CRE production rate, which itself is proportional to the supernova rate and hence to the SFR. The Condon relation is a *calorimetric model*, which requires at a minimum the following two assumptions to hold (Völk 1989; Lisenfeld et al. 1996): (1) galaxies act as a calorimeter both for the CREs and for the ionizing UV-photons: and (2) although CREs have competing energy losses to synchrotron radiation such as inverse Compton (IC) radiation, ionization, bremsstrahlung, and adiabatic losses, the fraction of these additional losses to the synchrotron radiation should remain constant. The assumption of a CRE calorimeter does hold in starburst galaxies (e.g., Paglione & Abrahams 2012; Yoast-Hull et al. 2013), but probably not in normal spiral galaxies. Therefore, as alternatives, there are *non-calorimetric* models that do account for a possible CRE escape (Helou & Bica 1993; Niklas & Beck 1997; Lacki et al. 2010; Dumas et al. 2011; Tabatabaei et al. 2013b). The models of Helou & Bica (1993) and Lacki et al. (2010) were proposed to explain the RC–far-IR (FIR) correlation, allowing for a possible escape of dust heating FUV photons to compensate the escape of CREs. These models are hence not strictly applicable to the RC–SFR relation, because, as we will see, we are using SF tracers that do account for the escape of FUV photons. Hence, we do not consider them any further. The model by Niklas & Beck (1997) and their spatially resolved derivatives (Dumas et al. 2011; Tabatabaei et al. 2013b), however, although again posed to explain the RC–FIR correlation, do assume a direct proportionality between the FIR luminosity and the SFR. Hence, they are essentially models for the RC–SFR relation and thus relevant for our study.

We will use Condon’s relation as the basis of our study and investigate whether it holds for our sample for integrated SFRs, as well as for SFR surface densities (Σ_{SFR}). Two emission processes contribute to the RC emission: massive stars contribute to both the thermal and the non-thermal emission. The thermal emission originates from free–free emission of electrons in the H II region surrounding these stars. The H α emission can be used as a proxy for the thermal emission; the radio spectral index of the thermal emission is flat with $\alpha = -0.1$ ($S_\nu \propto \nu^\alpha$). The non-thermal emission is generated by young CREs accelerated in supernova shockwaves. They emit synchrotron emission in the magnetized interstellar medium with a non-thermal spectral index of typically $\alpha_{\text{nt}} = -0.83$ (Niklas et al. 1997). Tabatabaei et al. (2007b,c) separated the thermal and non-thermal RC emission in M33 based on a novel method to correct Balmer H α emission for internal extinction by dust. They found that the non-thermal emission is distributed more smoothly than the thermal emission, as expected from cosmic-ray transport (Tabatabaei et al. 2007a).

Young supernova remnants are visible as strong non-thermal sources but contribute only about 10% to the instantaneous non-thermal RC emission at wavelengths around $\lambda 20$ cm (Condon 1992; Lisenfeld & Völk 2000). The main contribution to the RC emission comes from diffuse emission in the interstellar medium. Cosmic rays diffuse along magnetic field lines or are advected in galactic outflows. The electrons lose their energy and remain visible typically for as long as 10^8 yr after the SF event that generated them, depending on the magnetic field strength (for a strong field, this time can be shorter). The non-thermal RC distribution can therefore be understood as a smeared-out version of the SFR distribution (Bica et al. 1989; Murphy et al. 2006a,b, 2008). As we can see, the thermal RC and non-thermal RC behave in different ways, motivating a separation of the RC emission in order to study them separately. Even though the non-thermal RC dominates at wavelengths around $\lambda 20$ cm, the thermal RC can become more important for local measurements (1 kpc scale). In the following, RC refers to the *total* RC, i.e., the sum of the thermal and non-thermal RC, except when we specifically refer to one of the components.

Studies of the RC–SFR relation started out based on integrated properties of the galaxies under study. Often, no allowance could be made for contaminating background sources within the fairly large beams of single-dish telescopes. Likewise, single-dish radio flux densities can be contaminated by the presence of an active galactic nucleus (AGN). Condon et al. (2002) tried to separate AGNs from their sample by taking out the outliers with too high a radio luminosity compared to the SFR observed, but that selection is obviously not able to detect some of the weaker AGNs. Spatially resolved studies circumvent this problem as an AGN can be readily identified as an excess of radio brightness in the center of a galaxy. Similarly, background radio sources can be identified and their contribution removed.

Recent observational efforts have concentrated on studies of the RC–FIR or RC–mid-infrared (RC–MIR) correlation rather than the RC–SFR relation at ever higher spatial resolutions. Using wavelet correlation spectra, Dumas et al. (2011) show that the correlation between $\lambda 20$ cm RC and $24 \mu\text{m}$ MIR emission in M51 (NGC 5194) holds well down to a scale of 1.8 kpc (the typical width of a spiral arm) and to a less extent to a scale of 500 pc (the CRE diffusion length), but breaks down at smaller scales. A study of the spatially resolved RC–FIR correlation in the Small Magellanic Cloud by Levrenz & Filipović (2013) found a good correlation down to a scale of 15 pc; however, this galaxy has a high thermal RC fraction, meaning that cosmic-ray diffusion is of less importance. Other papers dealing with spatially resolved studies of the RC–FIR correlation are those by Tabatabaei et al. (2007a) on M33 and Tabatabaei et al. (2013b) on NGC 6946, among others.

But until recently, no studies of the RC–SFR have been forthcoming. Obviously, such studies should have sufficient angular resolution in order to be able to isolate any AGN activity or unrelated background sources from the area under study. Moreover, spatially resolved studies allow one to probe the RC–SFR relation as a function of location within a galaxy, such as arm versus inter-arm. Thanks to the THINGS (The H I Nearby Galaxy Survey, Walter et al. 2008) collaboration—making use of SINGS (SIRTF Nearby Galaxy Survey; Kennicutt et al. 2003) and the “GALEX Ultraviolet Atlas of Nearby Galaxies” (Gil de Paz et al. 2007)—spatially resolved SFR maps have become available of a significant sample of nearby

Table 1
Basic Data of the Galaxies in Our Sample.

Galaxy	FWHM	i	D	D_{25}	M_B	M_{HI}	M_{H2}	$\log_{10}(M_s)$	PI	Type	z	Z
			(Mpc)			($10^8 M_\odot$)	($10^8 M_\odot$)	(M_\odot)	(%)		(10^{-2})	
(1)	(2)	(3)	(4)	(5)	(6)	(7)	(8)	(9)	(10)	(11)	(12)	(13)
Ho II	13'5	41°	3.4	6'61	-16.87	6.0	< 0.4	8.3	< 1.8	10	0.05	7.68
IC 2574	13'5	53°	4.0	12'88	-18.11	14.8	< 0.8	8.7	< 9	9	0.02	7.94
NGC 628	46'0	7°	7.3	9'77	-19.97	38.0	10.0	10.1	12	5	0.22	8.33
NGC 925	23'0	66°	9.2	10'72	-20.04	45.8	2.5	9.9	< 0.8	7	0.18	8.24
NGC 2403	13'6	63°	3.2	15'85	-19.43	25.8	0.2	9.7	7.8	6	0.04	8.31
NGC 2841	16'1	73°	14.1	6'92	-21.21	85.8	3.2	10.9	6.2	3	0.21	8.52
NGC 2903	34'1	65°	8.9	11'75	-20.93	43.5	21.8	10.0	4.0	4	0.19	9.12
NGC 2976	13'3	65°	3.6	7'24	-17.78	1.4	0.6	9.1	4.4	5	0.00	8.30
NGC 3184	18'6	16°	11.1	7'41	-19.92	30.7	15.9	10.3	6.4	6	0.20	8.48
NGC 3198	17'6	72°	13.8	6'46	-20.75	101.7	6.3	10.1	< 1.4	5	0.22	8.32
NGC 3627	55'6	62°	9.3	10'23	-20.74	8.2	12.6	10.6	2.5	3	0.24	8.43
NGC 4736	19'1	41°	4.7	7'76	-19.80	4.0	4.0	10.3	4.3	2	0.10	8.31
NGC 4826	33'6	65°	7.5	10'47	-20.63	5.5	18.1	10.4	1.0	2	0.14	8.59
NGC 5055	18'6	59°	10.1	11'75	-21.12	91.0	50.1	10.8	4.7	4	0.17	8.42
NGC 5194	17'1	42°	8.0	7'76	-21.04	25.4	25.1	10.6	6.9	4	0.15	8.54
NGC 6946	14'1	33°	5.9	11'48	-20.61	41.5	39.8	10.5	10	6	0.02	8.40
NGC 7331	22'1	76°	14.7	9'12	-21.67	91.3	50.1	10.9	3.8	3	0.27	8.36

Note. — Column 1: galaxy name; Column 2: resolution of the radio map as full-width-half-mean in arcsec; Column 3: inclination angle in degree; Column 4: distances in Mpc; Column 5: optical size in arcmin; Column 6: B -band absolute magnitude from Walter et al. (2008); Column 7: hydrogen mass from Walter et al. (2008); Column 8: molecular hydrogen mass from Leroy et al. (2008), NGC 2903 is from Leroy et al. (2009), NGC 4826 from Wilson et al. (2012); Column 9: decadal logarithm of stellar mass from Leroy et al. (2008), NGC 2841 and NGC 2903 are from de Blok et al. (2008), NGC 4826 was determined from *IRAS* data as in Leroy et al. (2008); Column 10: fractional polarization at $\lambda 22$ cm from Heald et al. (2009) with respect to our integrated flux density; Column 11: galaxy type from Walter et al. (2008); Column 12: redshift; Column 13: metallicity defined by $\log_{10}(\text{O}/\text{H}) + 12$ from Moustakas (2006).

galaxies. In this paper, we present a sample of 17 galaxies where we compare the RC brightness and the SFR surface density (Σ_{SFR}). We use Σ_{SFR} maps based on a combination of *Spitzer* MIR and *GALEX* FUV maps (see Leroy et al. 2008, for details). The RC data are from the Westerbork Synthesis Radio Telescope (WSRT) SINGS sample (Braun et al. 2007), taken at $\lambda 22$ and 18 cm.

The paper is organized as follows: Section 2 explains the selection of the sample and briefly summarizes the data processing applied to the maps that we used. Section 3 deals among other things with the azimuthally (Section 3.3) averaged plots where we compare the RC brightness with the Σ_{SFR} as a function of galactocentric radius. In Section 3.4 we produce pixel-by-pixel plots of our sample at a fixed resolution. The results are analyzed in Section 4 and discussed in Section 5 where we explore the dependence of the RC–SFR relation on various galaxy parameters. We present our conclusions in Section 6.

2. OBSERVATIONS

2.1. The Galaxy Sample

The overlap between the THINGS and the WSRT SINGS sample consists of 17 galaxies that we included in our analysis. All maps were transformed to the same coordinate system and convolved to the same angular resolutions before any comparison. Table 1 summarizes the properties of the objects used in this study. In Figure 1(a) we show the radio brightness at $\lambda 22$ cm in NGC 6946 and in Figure 1(b) the SFR surface density in the same galaxy.

2.2. Radio Continuum Maps

The RC maps come from the WSRT SINGS survey (Braun et al. 2007). This survey contains 28 galaxies observed at $\lambda 22$ and 18 cm in radio continuum. Observations were obtained in the “maxi-short” configuration, which is optimized for imaging extended emission. All data were cali-

brated in AIPS,⁸ with subsequent imaging and self-calibration in Miriad. All maps were primary beam corrected using the task LINMOS in Miriad (Sault et al. 1995). Because the WSRT is an east–west interferometer (with 2.7 km extent), the resolution in the north–south direction is declination dependent. This results in an elliptical Gaussian kernel for the restoration after the maps were cleaned (Högbom 1974). We convolved the maps with a further Gaussian kernel to obtain circular beam shapes. In Table 1 we present the resolution of the maps expressed by the full width at half maximum (FWHM). The resolution can be as high as 13'1 and is better than 20'' for most of our sample galaxies.

The RC maps were observed with an interferometer, which is not sensitive for emission on angular scales larger than about half the diameter of the primary beam ($\approx 30'$ for the WSRT at $\lambda 20$ cm). This figure is, however, dependent on the (u, v) -coverage and also on the source structure. In particular, some of our RC maps, notably at $\lambda 18$ cm, are affected by a lack of observed spacings shorter than 27 m, which results in the emission sitting within a negative “bowl”.⁹ The depth of the bowl can be up to $0.5 \times$ the rms noise level in some cases. As the $\lambda 18$ cm maps are more severely affected than the $\lambda 22$ cm maps, the effect on the measured radio spectral index is thus that it becomes too steep, particularly in the outskirts of galaxies where the emission levels drop to the rms noise level. As a first-order correction we applied a constant offset prior to calculating integrated flux densities, integrated spectral indices, and the radio spectral index maps.

2.3. Hybrid SFR Surface Density Maps

Leroy et al. (2008, 2012) motivated the use of combined

⁸ AIPS is free software released by the National Radio Astronomy Observatory (NRAO).

⁹ The shortest physical baseline length at the WSRT is 36 m. However, the shortest projected baseline lengths are typically 27 m before the data are flagged due to antenna shadowing at low elevations.

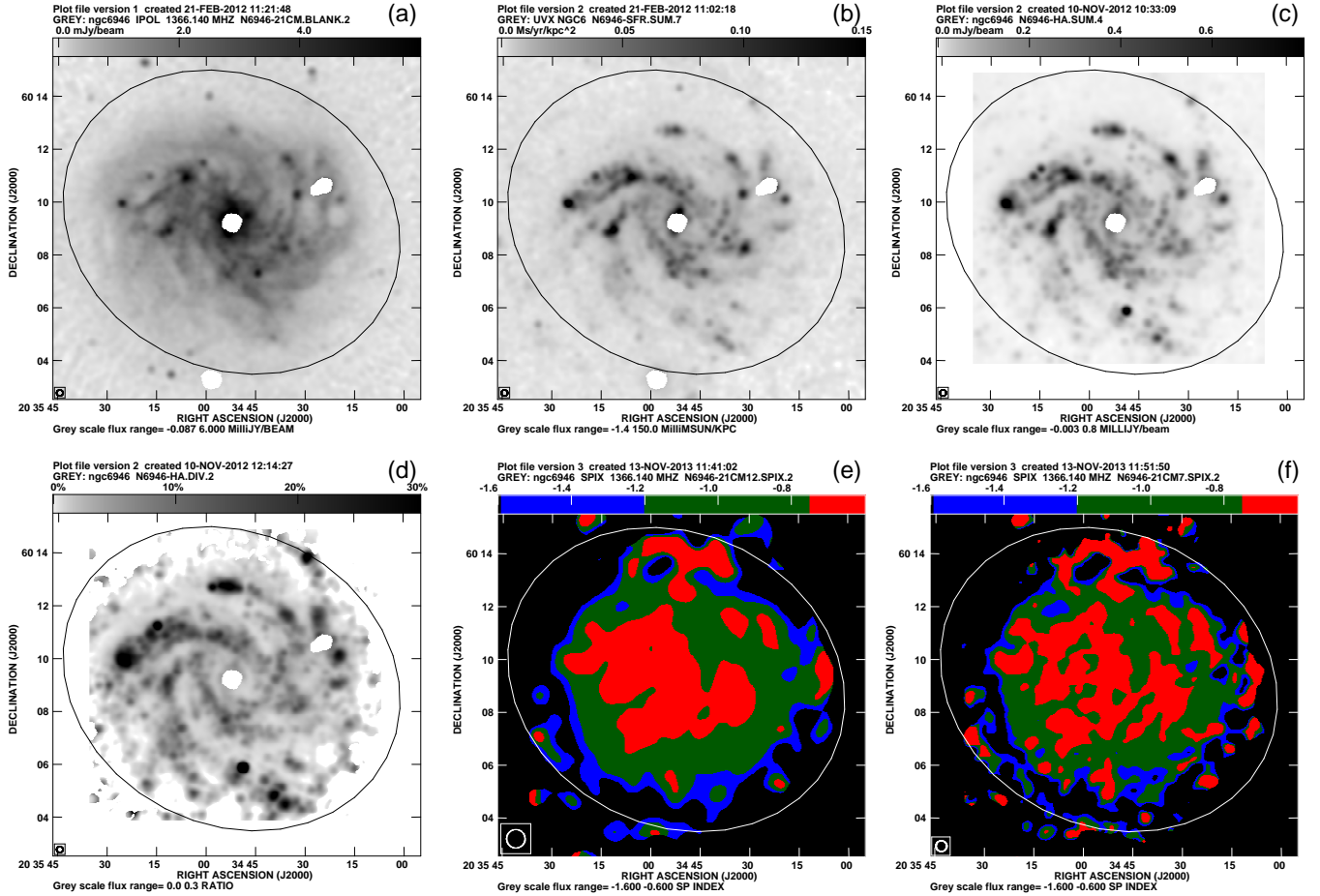


Figure 1. NGC 6946. (a) RC emission at $\lambda 22$ cm. (b) Hybrid SFR surface density ($\Sigma_{\text{SFR}}_{\text{hyb}}$). (c) Thermal RC emission as derived from $H\alpha$. (d) Predicted thermal RC fraction. (e) Radio spectral index at 1.2 kpc resolution. (f) Radio spectral index at 0.7 kpc resolution. The total RC intensity maps were clipped at $3 \times$ the rms noise level prior to combination resulting in a spectral index error of 0.6, which is lower in areas of higher intensities.

Spitzer 24 μm and *GALEX* FUV maps as a tracer for SF and the resolved SFR surface density. Their study was based on the THINGS sample, which consists of 34 galaxies observed with the NRAO¹⁰ VLA in B-, C-, and D-configuration in the $\lambda 21$ cm line of neutral hydrogen (H I). These galaxies were part of the SINGS survey by the *Spitzer* satellite consisting of 75 nearby galaxies (Kennicutt et al. 2003). They were also part of the *GALEX* FUV survey (Gil de Paz et al. 2007). The FUV traces the young SF via the UV radiation of massive stars. The dust absorbs the UV light efficiently, which gets re-radiated in the infrared. Therefore, the Multiband Imaging Photometer for *Spitzer* (MIPS) 24 μm maps trace the embedded SF. In massive spiral galaxies the inner region shows little FUV but strong 24 μm emission due to the locally higher dust content. The two tracers for SF are complementary and can be linearly combined to give the total SFR. The MIPS maps were convolved with a custom kernel to $13''.5$ resolution referred to as the half-power beam width of the Gaussian beam. The FUV maps were convolved to the same Gaussian beam before the combination with the MIPS maps; the Σ_{SFR} maps therefore have a resolution of $13''.5$. A detailed description of the motivation for the construction of the Σ_{SFR} maps can be found in Leroy et al. (2008).

We refer to these maps as *hybrid* Σ_{SFR} maps in order to dis-

tinguish them from the radio maps, which can be converted to *radio* Σ_{SFR} maps using Condon’s relation (see Section 3.1). We use the hybrid Σ_{SFR} maps by Leroy et al. (2008) as an absolute reference of the SFR against which we compare our radio-derived Σ_{SFR} maps. We note that Leroy et al. (2012) suggested that the hybrid combination of *Spitzer* 24 μm MIR emission and Balmer $H\alpha$ emission is a more accurate SF tracer than the hybrid FUV/MIR combination. FUV maps provided by *GALEX* are much more sensitive, though, and have revealed current SF extending throughout the outskirts of galaxies as traced by H I (e.g., see Thilker et al. 2005; Bigiel et al. 2010; Kennicutt & Evans 2012). It is for that reason that we prefer to use the FUV/MIR hybrid Σ_{SFR} maps.

2.4. $H\alpha$ Maps

We are using $H\alpha$ emission as a tracer for thermal RC emission (see Section 3.2). Maps for the galaxies in our sample were obtained from the Local Volume Legacy (LVL) survey, which covers all galaxies within a distance of 11 Mpc (Kennicutt et al. 2008). The remaining maps were obtained from the SINGS legacy program (Kennicutt et al. 2003) with the exception of NGC 2903 (from Hoopes et al. 2001), NGC 4736 (from Sánchez-Gallego et al. 2012), and NGC 6946 (from Ferguson et al. 1998).

All maps were continuum subtracted using a broad R -band continuum image. LVL maps were found to be in agreement to within 5%–10% of the flux densities published by Ken-

¹⁰ The National Radio Astronomy Observatory is a facility of the National Science Foundation operated under cooperative agreement by Associated Universities, Inc.

nicutt et al. (2008). For the SINGS legacy maps, however, background levels fluctuated and were not always properly adjusted. Sánchez-Gallego et al. (2012) reprocessed some of the SINGS maps, which resulted in an improved background subtraction. Where possible, we used their maps. We typically got flux densities within 30% of the published values. This is of sufficient accuracy, because the $H\alpha$ maps are only used to correct for the thermal component to the radio continuum emission and the typical contribution to the radio continuum flux density by the thermal emission is less than 30%. We used $E(B-V)$ values as published by Schlegel et al. (1998) to correct for foreground absorption by the Galaxy. We note that we correct for foreground absorption only and not for *internal* absorption by dust within the observed galaxies (see also Section 3.2). With the exception of NGC 6946 the emission maps include the contribution from the [N II] line, which lies within the filter coverage (see Section 3.2 for further details).

2.5. Masking of AGNs and Background Sources

Our resolved study allows us to identify regions of radio emission in our maps that is coming from an AGN or from background radio galaxies. AGNs are visible as compact nuclear sources. Background radio galaxies are significant sources in radio emission but weak in the Σ_{SFR} maps. The preferred way of dealing with the above-mentioned objects, is to mask them in the maps, so they do not influence our results.

This can be done by “blinking” the radio and hybrid Σ_{SFR} maps, which clearly highlights those objects. Sources are blanked within AIPS with the task `BLANK`, which basically creates a mask by selecting regions on a display. This mask is then applied to all maps (RC, Σ_{SFR} , $H\alpha$) in order to remain consistent. In general, we masked all significant sources that are in the center of any given galaxy. Only galaxies that do not have a significant central source are not masked. Secondly, we masked background radio galaxies that are showing up as strong radio sources while no counterpart is visible in the Σ_{SFR} maps. Thirdly, we masked sources in the Σ_{SFR} maps that do not show up in the radio. These sources are relatively rare and could be stars or possibly submillimeter galaxies.

Nuclear sources are easy to identify, but background sources in either the radio or hybrid Σ_{SFR} maps can be somewhat ambiguous. We stress that the number of sources that are removed in each galaxy is small, typically less than five. Therefore, we expect the accuracy of the masking to be sufficient. As an example we quote NGC 628, which is the galaxy most affected by background radio sources. The difference between integrated luminosity with or without this correction is smaller than 15%. In all other galaxies the difference is yet smaller. For spurious sources in the hybrid Σ_{SFR} maps, the difference is considerably smaller than in the radio maps. Therefore again, we expect errors or omissions in the masking procedure not to influence our analysis or conclusions.

3. METHODOLOGY

3.1. Resolved RC–SFR Relation

As discussed in Section 1, Condon’s relation states that the integrated SFR and the RC luminosity of a galaxy are proportional to each other. In this section we explain how we can derive resolved radio Σ_{SFR} maps. According to Equation (27) in Condon et al. (2002), the SFR can be expressed as

$$\frac{\text{SFR}_{\text{RC}}}{M_{\odot} \text{ yr}^{-1}} \Big|_{>0.1 M_{\odot}} = 0.75 \times 10^{-21} \left(\frac{L_{1.4 \text{ GHz}}}{\text{W Hz}^{-1}} \right), \quad (1)$$

where $L_{1.4 \text{ GHz}}$ is the RC luminosity at 1.4 GHz of an unresolved galaxy. We note that Condon used a Salpeter initial mass function (IMF) to extrapolate from the massive stars ($M > 5 M_{\odot}$) that show up in the RC to that of all stars formed ($0.1 < M/M_{\odot} < 100$). The hybrid Σ_{SFR} maps of Leroy et al. (2008) are based on a broken power-law IMF as described in Calzetti et al. (2007), so their derived SFRs are a factor of 1.59 lower than using the Salpeter IMF. We have thus scaled Condon’s relation in this paper accordingly.

Condon (1992) derived the above relation by adding the thermal and non-thermal RC contribution. For the non-thermal emission it was assumed that one can scale the non-thermal luminosity of the Milky Way as modeled by Beuermann et al. (1985) based on the 408 MHz observations by Haslam et al. (1982) to the observed Type II supernova rate of Tammann (1982). The thermal RC contribution was derived from the Balmer $H\alpha$ line emission following the SFR relation as presented in Kennicutt (1983). As Condon’s relation is widely used in the literature, we will use it as the basis of our analysis.

If we use $L_{1.4 \text{ GHz}} = 4\pi A I_{1.4 \text{ GHz}}$, where A is the area observed, we obtain for resolved emission the relation converted to the SFR surface density measured in the plane of the sky, Σ'_{SFR} as

$$\frac{(\Sigma'_{\text{SFR}})_{\text{RC}}}{M_{\odot} \text{ yr}^{-1} \text{ kpc}^{-2}} \Big|_{>0.1 M_{\odot}} = 8.8 \times 10^{-8} \left(\frac{I_{1.4 \text{ GHz}}}{\text{Jy ster}^{-1}} \right), \quad (2)$$

where $I_{1.4 \text{ GHz}}$ is the RC intensity at 1.4 GHz. The RC intensity is measured in units of Jy beam^{-1} , where the area of the synthesized beam is prescribed by the FWHM, effectively the resolution of the radio map. The solid angle a Gaussian beam subtends is $\Omega = 1.133 \times (\text{FWHM})^2 \text{ ster}$ or $\Omega = 2.66 \times 10^{-11} \times (\text{FWHM}[\text{arcsec}])^2 \text{ ster}$, where the FWHM is measured in arcsec. Thus, the Σ_{SFR} can be expressed as

$$\frac{(\Sigma'_{\text{SFR}})_{\text{RC}}}{M_{\odot} \text{ yr}^{-1} \text{ kpc}^{-2}} \Big|_{>0.1 M_{\odot}} = 3.31 \times 10^3 \cdot \left(\frac{\text{FWHM}}{\text{arcsec}} \right)^{-2} \cdot \left(\frac{I_{1.4 \text{ GHz}}}{\text{Jy beam}^{-1}} \right). \quad (3)$$

Because the hybrid Σ_{SFR} maps are inclination corrected, we need to correct the radio Σ_{SFR} for inclination angle as well and as follows: $(\Sigma_{\text{SFR}})_{\text{RC}} = \cos(i) \times (\Sigma'_{\text{SFR}})_{\text{RC}}$, where $0^\circ \leq i \leq 90^\circ$ is the inclination angle of the galaxy in question, and $i = 0^\circ$ is defined as face-on.

3.2. Thermal Radio Continuum Emission

The RC emission consists of non-thermal synchrotron and thermal free-free emission. As eventually we wish to also study the resolved non-thermal RC–SFR relation, we need to subtract a map of the thermal RC emission alone. A standard technique is to use $H\alpha$ emission for estimating the free-free RC emission. We use the $H\alpha$ maps described in Section 2.4 to create spatially resolved distributions of the thermal RC emission. According to Deeg et al. (1997),

$$\frac{S_{\text{th}}(\nu)}{\text{erg cm}^{-2} \text{ s}^{-1} \text{ Hz}^{-1}} = 1.14 \times 10^{-14} \left(\frac{\nu}{\text{GHz}} \right)^{-0.1} \cdot \left(\frac{T_e}{10^4 \text{ K}} \right)^{0.34} \left(\frac{F_{H\alpha}}{\text{erg cm}^{-2} \text{ s}^{-1}} \right), \quad (4)$$

where S_{th} is the thermal RC flux density and $F_{H\alpha}$ is the Balmer $H\alpha$ emission line flux. We use an electron temper-

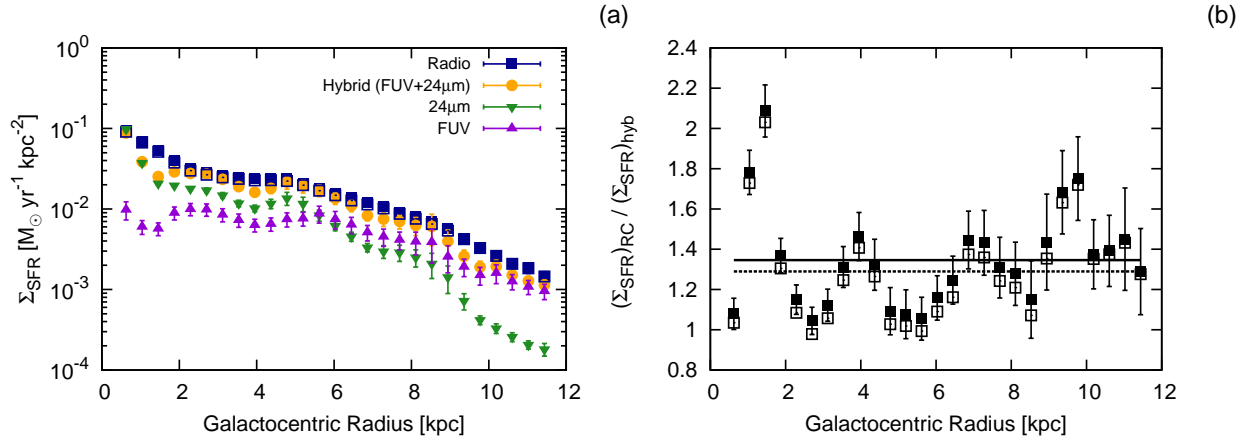


Figure 2. NGC 6946. (a) Radial distribution of the $(\Sigma_{\text{SFR}})_{\text{RC}}$ from $\lambda 22$ cm RC emission (dark blue), hybrid (FUV + $24 \mu\text{m}$) $(\Sigma_{\text{SFR}})_{\text{hyb}}$ (orange), $24 \mu\text{m}$ alone (green), and FUV alone (violet). (b) Ratio \mathcal{R} of RC to hybrid Σ_{SFR} as a function of galactocentric radius. Open symbols represent the non-thermal RC emission alone. The solid line shows a least-squares fit to the data points assuming a constant ratio (dashed line for the non-thermal RC emission alone).

ature of $T_e = 10^4$ K, which is a good approximation for most cases. The thermal contribution was then subtracted from the radio data before further analysis (Sections 3.3 and 3.4). We did not correct for the contribution by [N II], which according to Kennicutt et al. (2008) is typically 40% in our sample. Kennicutt et al. (2008) provided only global estimates of the [N II]/ $\text{H}\alpha$ ratio, so we do not have any spatial information of the [N II] contribution. On the other hand, as mentioned in Section 2.4, we did not correct the $\text{H}\alpha$ emission for internal extinction, which in normal galaxies is typically in the 0–1 mag range at $\text{H}\alpha$. In Figures 1(c) and (d) we present the distribution of the thermal RC emission and the fraction of thermal emission in NGC 6946, respectively.

These maps can be compared with the those by Beck (2007), who separated thermal and non-thermal emission based on observations at $\lambda\lambda$ 20 and 3 cm, assuming a constant non-thermal spectral index of $\alpha_{\text{nt}} = -1.0$ in NGC 6946. Another approach to derive maps of the thermal emission was taken by Tabatabaei et al. (2013b), who de-redden the $\text{H}\alpha$ maps by first modeling the dust spectral energy distribution. Qualitatively these maps of the thermal RC are all quite similar. Given that the integrated thermal fraction is on average less than 10% across the angular scales discussed here, we consider our estimate for the thermal RC contribution at $\lambda 20$ cm adequate. In Appendix B we present relevant maps for the entire sample.

We notice that we did correct for thermal RC emission to measure the integrated non-thermal spectral index, but not for the spectral index on a 1 kpc scale. This is because in the pixel measurements, the uncertainty in the $\text{H}\alpha$ maps would contribute to the already relatively high error of the radio spectral index. The integrated non-thermal radio spectral index is typically only 0.1 steeper than the integrated radio spectral index.

3.3. Radial Profiles

As the first step we analyzed the data using azimuthal averaging. We convolved the radio and hybrid Σ_{SFR} maps with a Gaussian kernel to bring them to the same resolution and regridded the maps to a common coordinate system. The resolution is either $13''.5$, set by the hybrid Σ_{SFR} maps, or limited by the resolution of the radio maps. We used inclination and position angles for the elliptical annuli as given in Table 1. We created azimuthal averages by using elliptical annuli spaced by one FWHM using the task `IRING` of AIPS. This results in plots of the Σ_{SFR} based on the RC emission at $\lambda 22$ cm or the

hybrid Σ_{SFR} maps as a function of galactocentric radius.

The two dwarf irregular galaxies, Holmberg II and IC 2574, are only barely detected in RC emission, even though they are quite prominent in SFR maps based on UV or optical/IR wavelengths. For these two galaxies we chose the center of the elliptical annuli to be centered on the brightest emission visible in the RC maps. For all other galaxies we chose the center of the elliptical annuli to coincide with the center of the galaxies.

We converted the averaged RC brightnesses into averaged Σ_{SFR} in each annulus using Equation (3). For the hybrid Σ_{SFR} we integrated them in the same annuli and calculated again the averaged Σ_{SFR} . We note that the Σ_{SFR} are inclination corrected. In Figure 2 we show the results for NGC 6946 as an example. We present both the radial distributions of the radio and hybrid Σ_{SFR} and their ratio. The results for the entire sample are shown in Appendix B.

We also use `IRING` to measure integrated values of the RC flux densities, hybrid SFRs, and thermal RC flux densities. We use an ellipse with the major axis of the galaxy and a minor axis corresponding to an aspect ratio for an inclination angle of 40° . This ensures that we include the RC emission in the halos of the galaxies. These integrated values are listed in Table 2. We note that these values are usually lower than the values given in Braun et al. (2007), because we masked the maps to exclude AGNs and background galaxies (see Section 2.5). The values we present should represent the best estimate of the RC emission in each galaxy that originates from SF.

3.4. Pixel-by-pixel Analysis

We subsequently investigated the relation between the radio and hybrid Σ_{SFR} by averaging in “pixels”, for which we chose squares with a constant linear scale for all galaxies. Taking into account the various angular resolutions and distances across our sample, we chose two linear scales of 0.7 kpc and 1.2 kpc, respectively. These scales are chosen in order to be able to analyze most galaxies at a set resolution. We can analyze six galaxies at 0.7 kpc, and this number increases to 12 for a scale of 1.2 kpc. These linear scales are similar to recent studies of resolved Σ_{SFR} in THINGS galaxies (Leroy et al. 2008; Bigiel et al. 2008).

The maps were convolved with a circular Gaussian kernel to the angular resolution corresponding to the linear scale studied. A grid with the corresponding resolution was overlaid,

Table 2
Measured Properties of the Galaxies in Our Sample.

Galaxy	$S_{22\text{ cm}}$ (Jy)	f_{th} (%)	SFR_{RC} ($M_{\odot} \text{ yr}^{-1}$)	SFR_{hyb} ($M_{\odot} \text{ yr}^{-1}$)	\mathcal{R}_{int}	$\langle \mathcal{R} \rangle$	$\mathcal{R}_{\text{int}}^{\text{nth}}$	$\langle \mathcal{R}^{\text{nth}} \rangle$	δ
(1)	(2)	(3)	(4)	(5)	(6)	(7)	(8)	(9)	(10)
Ho II	0.027 ± 0.001	16	0.028 ± 0.002	0.033 ± 0.002	0.87 ± 0.09	0.80 ± 0.38	0.68 ± 0.07	0.67 ± 0.40	0.26 ± 0.06
IC 2574	0.007 ± 0.001	41	0.010 ± 0.001	0.033 ± 0.002	0.31 ± 0.03	0.29 ± 0.09	0.02 ± 0.00	0.17 ± 0.07	1.21 ± 0.27
NGC 628	0.192 ± 0.010	9	0.929 ± 0.047	0.848 ± 0.042	1.10 ± 0.11	1.56 ± 0.81	0.99 ± 0.10	1.50 ± 0.86	...
NGC 925	0.079 ± 0.004	12	0.608 ± 0.031	1.417 ± 0.071	0.43 ± 0.04	0.40 ± 0.06	0.37 ± 0.04	0.33 ± 0.05	0.62 ± 0.04
NGC 2403	0.357 ± 0.018	22	0.331 ± 0.017	0.868 ± 0.043	0.38 ± 0.04	0.35 ± 0.09	0.31 ± 0.03	0.26 ± 0.09	0.64 ± 0.03
NGC 2841	0.093 ± 0.005	11	1.677 ± 0.086	2.464 ± 0.123	0.68 ± 0.07	0.64 ± 0.07	0.57 ± 0.06	0.51 ± 0.10	0.42 ± 0.03
NGC 2903	0.351 ± 0.018	6	2.514 ± 0.126	2.999 ± 0.150	0.84 ± 0.08	0.83 ± 0.19	0.79 ± 0.08	0.87 ± 0.19	...
NGC 2976	0.068 ± 0.003	11	0.080 ± 0.004	0.205 ± 0.010	0.39 ± 0.04	0.34 ± 0.09	0.34 ± 0.03	0.29 ± 0.10	0.50 ± 0.03
NGC 3184	0.078 ± 0.004	10	0.868 ± 0.044	0.835 ± 0.042	1.04 ± 0.10	1.06 ± 0.24	1.04 ± 0.10	0.95 ± 0.21	0.56 ± 0.03
NGC 3198	0.036 ± 0.002	6	0.614 ± 0.033	2.138 ± 0.107	0.29 ± 0.03	0.25 ± 0.02	0.29 ± 0.03	0.22 ± 0.02	0.27 ± 0.04
NGC 3627	0.501 ± 0.025	3	3.928 ± 0.197	4.916 ± 0.246	0.80 ± 0.08	0.80 ± 0.06	0.77 ± 0.08	0.77 ± 0.06	...
NGC 4736	0.265 ± 0.013	12	0.530 ± 0.027	0.503 ± 0.025	1.05 ± 0.11	1.38 ± 0.56	0.97 ± 0.10	1.23 ± 0.52	0.75 ± 0.03
NGC 4826	0.072 ± 0.004	9	0.368 ± 0.019	0.753 ± 0.038	0.49 ± 0.05	0.53 ± 0.08	0.41 ± 0.04	0.47 ± 0.06	...
NGC 5055	0.372 ± 0.019	4	3.437 ± 0.172	3.778 ± 0.189	0.91 ± 0.09	0.87 ± 0.05	0.86 ± 0.09	0.83 ± 0.05	0.79 ± 0.02
NGC 5194	1.185 ± 0.059	5	6.870 ± 0.344	3.929 ± 0.196	1.75 ± 0.17	1.71 ± 0.89	1.68 ± 0.17	1.63 ± 0.89	0.67 ± 0.02
NGC 6946	1.471 ± 0.074	5	4.637 ± 0.232	3.497 ± 0.175	1.33 ± 0.13	1.35 ± 0.25	1.22 ± 0.12	1.29 ± 0.25	0.80 ± 0.02
NGC 7331	0.381 ± 0.019	4	7.461 ± 0.373	11.765 ± 0.588	0.63 ± 0.06	0.66 ± 0.14	0.63 ± 0.06	0.66 ± 0.14	...

Note. — Column 1: galaxy name; Column 2: RC flux density at $\lambda 22$ cm; Column 3: thermal fraction of the RC emission at $\lambda 22$ cm; Column 4: radio derived star-formation rate at $\lambda 22$ cm; Column 5: star-formation rate from hybrid FUV + $24 \mu\text{m}$ tracer; Column 6: ratio of integrated radio to hybrid SFR; Column 7: radially averaged ratio of radio to hybrid Σ_{SFR} ; Column 8: ratio of integrated non-thermal radio to hybrid SFR; Column 9: radially averaged ratio of non-thermal radio to hybrid Σ_{SFR} ; Column 10: slope of pixel-by-pixel plot at 1.2 kpc resolution for the total RC emission (see text).

and the pixel values were determined in Miriad using *IMSTAT*. We used a cutoff level of three times the rms noise level for the radio and hybrid Σ_{SFR} data. We calculated the radio spectral index between $\lambda\lambda$ 22 and 18 cm using the convention that $S_{\nu} \propto \nu^{\alpha}$, where α is the radio spectral index (of the total RC emission, i.e., not corrected for thermal emission). For this, we again used a cutoff level of three times the rms noise level for the $\lambda 18$ cm RC maps.

Σ_{SFR} values are inclination corrected, as for the azimuthally averaged analysis (Section 3.3). We plot pixel-by-pixel values of the Σ_{SFR} in NGC 6946 in Figure 3, where we used a log-log representation of the Σ_{SFR} of the radio and FUV/MIR data. We show the radio Σ_{SFR} at $\lambda 22$ cm both for the total RC emission and for the non-thermal RC emission only. Data points are color coded according to radio spectral index between $\lambda\lambda$ 22 and 18 cm, where red represents a spectral index corresponding to young CREs, green an intermediate spectral index, and blue data points with a spectral index dominated by old CREs. At wavelengths around $\lambda 20$ cm the RC emission is dominated by non-thermal synchrotron emission. Young CREs have a non-thermal spectral index of $\alpha_{\text{nt}} \approx -0.6$ (Green 2009), which steepens as they age to $\alpha_{\text{nt}} < -1$, referred to as cosmic-ray “aging”. We will refer to the non-thermal spectral index as either “young” or “old” depending on whether it is dominated by young or old CREs. We also present the distribution of the radio spectral index as maps with resolutions of 0.7 kpc and 1.2 kpc matching those of the pixel-by-pixel plots. The colors used for these maps are identical to those of the pixel-by-pixel plots. Results for the entire sample are again shown in Appendix B.

3.5. Estimate of the Uncertainties

We calculated the error in the integrated flux densities from two error contributions. The first is from an absolute calibration uncertainty, which is assumed to be 5% (Braun et al. 2007). We note that the relative calibration error between WSRT $\lambda\lambda$ 22 and 18 cm is much smaller with 0.5%, allowing us to reliably measure the radio spectral index. Secondly, the rms noise of a map needs to be taken into account by

$\sigma_N = \sigma \sqrt{N}$, where N is the number of independent beams and σ the rms noise in the map. This effect becomes important the larger the integrated area and thus the number of independent beams within an annulus is. This error is, however, small in comparison to the intrinsic fluctuations within one individual annulus. We therefore used the standard deviation of the measured intensities within one annulus as our second error contribution. The two error contributions were quadratically added within each annulus. Because the non-thermal RC flux densities are derived by subtracting the thermal RC emission from the total RC emission, we would need to include an additional error term stemming from the $\text{H}\alpha$ flux uncertainty. However, because the thermal RC contributes on average only 11% to the global RC flux density, we neglect this error contribution.

For surface brightness measurements, and hence for extended emission, the estimated uncertainty for the *GALEX* FUV maps is 0.15 mag (Gil de Paz et al. 2007), thus a 15% calibration error. For the *Spitzer* $24 \mu\text{m}$ maps the photometric uncertainty is 2% for both unresolved sources and extended emission (Engelbracht et al. 2007). As the hybrid Σ_{SFR} maps are a combination of FUV and $24 \mu\text{m}$ emission with the latter dominating, we use an average formal calibration error of 5% for our hybrid Σ_{SFR} maps.

We note that these are of course only the formal uncertainties to measure the MIR and FUV flux densities. Converting them into measurements of the SFR introduces further calibration errors. Leroy et al. (2012) compares the hybrid SF tracer we use with various other tracers in order to determine the calibration error. Their best estimate of the calibration error is $\pm 50\%$ for galaxy integrated SFRs and a factor of 2–3 for locally (1 kpc scale) derived hybrid Σ_{SFR} . In the following analysis, we would like to investigate to what degree the RC emission can be used as an SF tracer for both global and local (1 kpc) measurements. In order to do this, we use the formal errors only, for both the radio and hybrid Σ_{SFR} maps, so that we can see how much the radio-derived SFRs are deviating from the hybrid SFRs in comparison with the formally expected uncertainties.

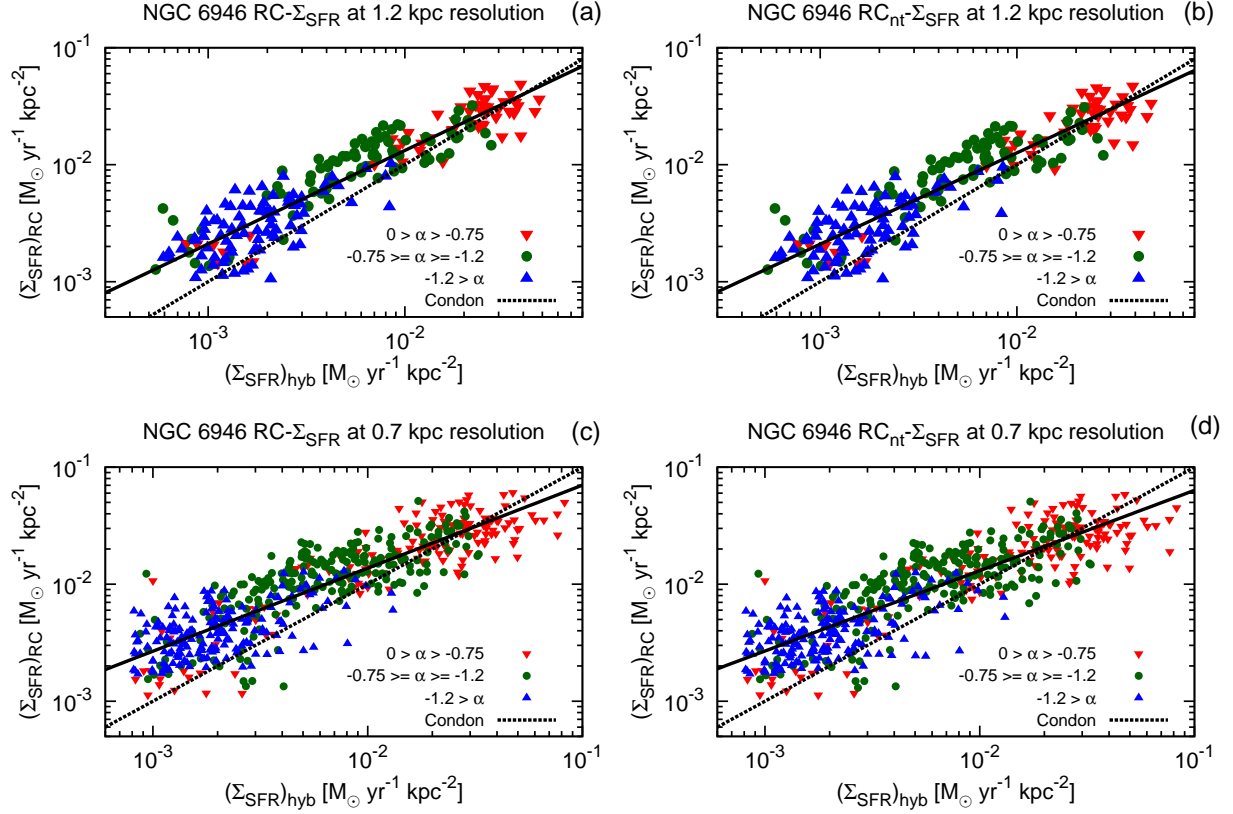


Figure 3. NGC 6946. (a) Radio Σ_{SFR} plotted against hybrid Σ_{SFR} at 1.2 kpc resolution. (b) Same as (a) but for the non-thermal RC emission only based radio Σ_{SFR} . (c) and (d) Same as (a) and (b) but at 0.7 kpc resolution. The dashed line shows the one-to-one Condon relation, and the solid line is a linear least-squares fit to the data points. Red data points indicate a “young” non-thermal spectral index ($\alpha > -0.75$), blue data points an “old” non-thermal spectral index ($\alpha < -1.2$), and green data points a non-thermal spectral index of intermediate age ($-0.75 \geq \alpha \geq -1.2$). The typical uncertainties for the radio spectral index are 0.4, 0.2, and 0.1 for the blue, green, and red data points, respectively.

Leroy et al. (2012) proposed a correction for the so-called cirrus emission in the MIR, which is not related to any recent SF but comes from the background radiation field of the old stellar population. Since we used the hybrid Σ_{SFR} as originally proposed by Leroy et al. (2008), no cirrus correction was applied. We do not expect this to affect our analysis, because the cirrus contribution to the $24 \mu\text{m}$ MIR emission is only 19% for global measurements. Locally, the cirrus contribution becomes only important in the outskirts of galaxies, where the FUV emission is anyway dominating the Σ_{SFR} . The difference between locally (1 kpc scale) derived hybrid Σ_{SFR} values with and without the correction for cirrus emission is typically less than $\approx 25\%$.

4. RESULTS

4.1. Integrated RC–SFR Relation

As a first exercise, we calculate integrated radio luminosities and SFRs for each galaxy and thus test the integrated RC–SFR relation. For this we integrated both the radio intensity and the hybrid Σ_{SFR} in elliptical annuli as explained in Section 3.3. The integrated values are presented in Table 2 for each galaxy, where SFR_{RC} is the radio SFR using the Condon relation from Equation (1) and SFR_{hyb} is the value as defined by the hybrid Σ_{SFR} maps.

We present our result in Figure 4(a) for the total RC emission and in Figure 4(b) for the non-thermal RC emission alone. Clearly, the SFRs as derived from the RC luminosity and the hybrid SF tracers agree well. Our sample covers

2–3 orders of magnitude in SFR. This confirms the validity of the assumption that we can use the RC as an SF tracer. It also confirms that Condon’s relation holds for the integrated SFRs in our galaxy sample. In the plot we show as a black line the relation that we would expect from the Condon relation and in red a line derived from a fit to the data, where we use the following representation:

$$\log_{10}(\text{SFR}_{\text{RC}}) = \zeta \cdot \log_{10}(\text{SFR}_{\text{hyb}}) + \xi. \quad (5)$$

We find $\zeta = 1.11 \pm 0.08$ and $\xi = -0.17 \pm 0.05$ using a standard bivariate least-squares fit for the total RC emission including thermal RC emission. For the non-thermal RC emission we find $\zeta_{\text{nt}} = 1.16 \pm 0.08$ and $\xi_{\text{nt}} = -0.22 \pm 0.06$, very similar to that for the total emission. Strictly speaking, we cannot apply the Condon relation to the non-thermal RC emission only. But we would like to study the relation between the non-thermal RC emission and the hybrid SFR in order to better understand the origin of the former. This relation has important consequences, for instance, for the generation of magnetic fields in galaxies, as we will discuss in Section 5.4. Both fits depend quite heavily on the inclusion of IC 2574, a dwarf galaxy with a weak detection. Excluding IC 2574, the fit to the data becomes linear within the error margin ($\zeta = 1.05 \pm 0.09$).

In Table 2 we also show the ratio of integrated SFRs as calculated from the RC and hybrid SF maps in each galaxy. We will use this ratio in various places throughout the paper.

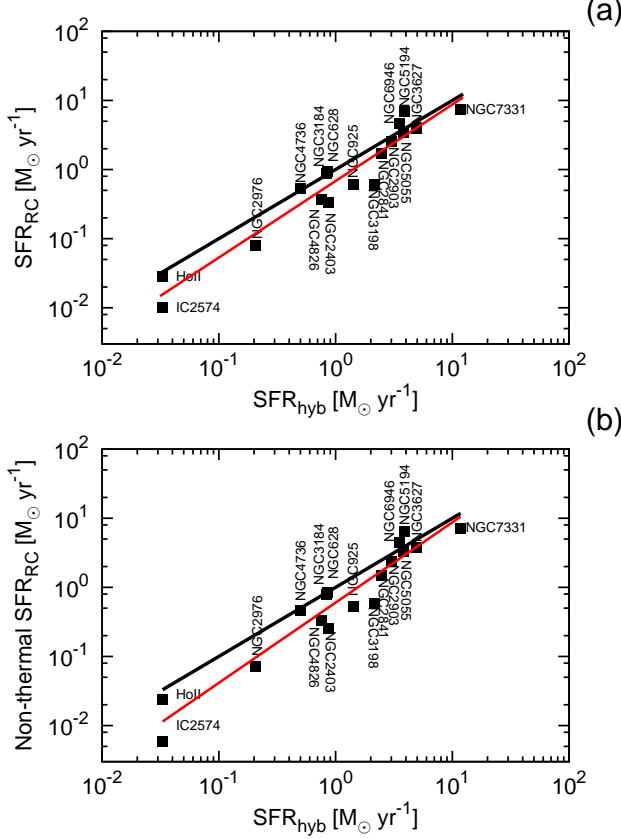


Figure 4. Comparison between the integrated SFRs from the total RC emission and hybrid SF tracers. The black line shows the relation expected from the Condon relation, i.e., would correspond to a linear (one-to-one) relation. The red line is a fit to the data points. (a) For the total RC emission. (b) For the non-thermal RC emission alone. The error bars, in both x- and y-direction, are smaller than the size of the symbols.

Therefore, we define it here as

$$\mathcal{R}_{\text{int}} \equiv \frac{\text{SFR}_{\text{RC}}}{\text{SFR}_{\text{hyb}}}, \quad (6)$$

for the integrated SFRs. Another way of looking at our data is to take the average of this ratio. For the average ratio in our sample we find for the total RC emission:

$$\left\langle \frac{\text{SFR}_{\text{RC}}}{\text{SFR}_{\text{hyb}}} \right\rangle = 0.78 \pm 0.38,$$

where the ratio is the arithmetic average and the quoted error is the standard deviation of our measurement set. Similarly, we find for the non-thermal RC emission only:

$$\left\langle \frac{\text{SFR}_{\text{RC}}}{\text{SFR}_{\text{hyb}}} \right\rangle_{\text{nt}} = 0.70 \pm 0.39.$$

The galaxies in our sample lie systematically slightly below, although individually they fall well within one standard deviation of the Condon relation. This is a remarkable success of Condon's relation, particularly if we consider the systematic effects involved in the way the relation was derived (Section 3.1). The spread in the ratio \mathcal{R}_{int} ranges from 0.31 (IC 2574) to 1.74 (NGC 5194). The first galaxy is a dwarf irregular Galaxy and the second one is a galaxy that is interacting with its nearby neighbor. The standard deviation of 0.38 is about half of the ratio \mathcal{R}_{int} ; hence, an individual galaxy

can be either radio dim or radio bright by a factor of $\pm 50\%$. This is identical to the lower limit for the uncertainty that is inherent to the hybrid SF tracers as well when used for integrated SFRs (Leroy et al. 2012). We can thus conclude that for integrated SFRs the RC luminosity measurements are of similar accuracy as SF values derived on the basis of other tracers. In the next sections we investigate whether this holds also locally in galaxies.

4.2. Radial Profiles of Radio and Hybrid Σ_{SFR}

As we have seen in Section 4.1, the integrated RC luminosity and the SFR from the hybrid SF tracers are directly proportional, as expected from the Condon relation. We next proceed to investigate the behavior of the two SF tracers averaged in elliptical annuli (Figure 2). We see that the two Σ_{SFR} agree quite well, with the radio Σ_{SFR} offset by an almost constant distance above the hybrid Σ_{SFR} . This means that the ratio of the radio to the hybrid Σ_{SFR} is almost constant with galactocentric radius; this is shown in a separate plot. We define the local ratio of the radio Σ_{SFR} to the hybrid Σ_{SFR} as

$$\mathcal{R} \equiv \frac{(\Sigma_{\text{SFR}})_{\text{RC}}}{(\Sigma_{\text{SFR}})_{\text{hyb}}}, \quad (7)$$

equivalent to the integrated SFRs in Equation (6). If the Condon relation were fulfilled, then the ratio should be equal to one. In the sample galaxy shown, NGC 6946, the ratio is $\mathcal{R} \approx 1.4$ and is remarkably constant as a function of galactocentric radius. There are some sinusoidal fluctuations with a period of ≈ 3 kpc in radius. These may be caused by the prominent spiral arms that are located at 2.4 and 5.4 kpc in the hybrid Σ_{SFR} map. The radii of the spiral arms agree with the minima in \mathcal{R} , because locally the hybrid SF tracer is proportionally higher than the more diffuse RC-based tracer. There is a further minimum at 8 kpc where no obvious spiral arm is located, although there are some SF regions in a northwestern direction (P.A. = -45°) at that distance from the nucleus. For NGC 6946 we find a radially arithmetic average ratio of $\langle \mathcal{R} \rangle = 1.35 \pm 0.25$, where the error is the standard deviation of all data points. For this galaxy the relative deviation of the ratio from its average is thus only 18%. The integrated ratio as determined in Sect. 4.1 is $\mathcal{R}_{\text{int}} = 1.32$, so these two are identical. The non-thermal radially averaged ratio is $\langle \mathcal{R}_{\text{nt}} \rangle = 1.28 \pm 0.26$, identical within the error to the value for the total RC emission, with a relative variation around the mean of 20%.

This trend of a constant ratio \mathcal{R} as a function of galactocentric radius is also found in the other galaxies. In Table 2 we present the integrated values of the SFR both from the radio (SFR_{RC}) and from the hybrid data (SFR_{hyb}) and their ratio (\mathcal{R}_{int}). We also list the radially averaged ratio of the local ratio $\langle \mathcal{R} \rangle$. It is instructive to compare the radially averaged ratio with the integrated ratio for all of our sample galaxies (Figure 5(a)). Both ratios agree remarkably well, and the radial ratios agree within the errors with the integrated ones. We can also see from that figure that the radial variation compared to the average is small for most of the galaxies. The mean standard deviation is 25% of the radially averaged ratio. NGC 6946 is thus a typical example with respect to the amplitude of its radial variation of the ratio. In Figure 5(b) we show the relation between the radially averaged radio SFR and the SFR as measured from the hybrid SF tracers, which can be compared with Figure 4(a). The agreement between the two figures is striking, underlining our conclusion that the

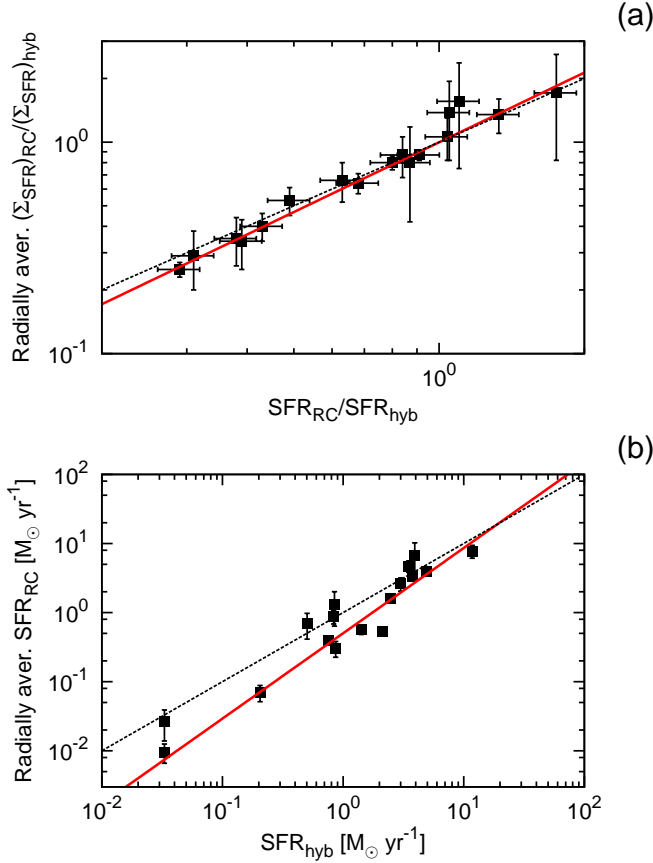


Figure 5. (a) Comparison between the radially averaged ratio $\langle \mathcal{R} \rangle$ and the integrated ratio \mathcal{R}_{int} . The black dashed line shows the one-to-one relation, and the red line is a fit to the data points. (b) Comparison between the radially averaged ratio $\langle \text{SFR}_{\text{RC}} \rangle$ (which is defined by $\langle \text{SFR}_{\text{RC}} \rangle \equiv \langle \mathcal{R} \rangle \cdot \text{SFR}_{\text{hyb}}$) and the integrated hybrid SFR_{hyb} . The black dashed line indicates a one-to-one relation, and the red line is a fit to the data points. The shown error bars are derived from the standard deviation of the radial data points from the arithmetic average.

azimuthally averaged ratios behave very similarly to the integrated ones.

The radial variation is mostly changing quasi-periodic, which means it cannot be described by a simple common function like a constant slope. Generally speaking, the ratio tends to increase with galactocentric radius rather than decrease. The best example for this is NGC 628, where the ratio increases almost monotonically with galactocentric radius. A more step-like increase is seen in NGC 2403, where the ratio jumps at a radius of 3 kpc from 0.3 to 0.45. There are no prominent cases where the ratio drops as a function of galactocentric radius, although NGC 2976 shows a monotonic decrease beyond a maximum at 1.5 kpc. Three galaxies have a relative ratio variation close to 50%, which is the largest variation in our sample. These are Holmberg II, NGC 628, and NGC 5194. At the other end of the scale are NGC 2841, NGC 3198, and NGC 3627, where the relative radial ratio variation is close to 10%.

In conclusion, we find that the radial variation appears to be quasi-periodic and cannot be easily described by a linear fit, for instance. We do not find any obvious candidate for a second parameter that could explain this behavior. Relative variations are small, however, and the arithmetic average of the radial data points agrees, within the standard deviation, with integrated ratios of RC to hybrid SFRs.

4.3. Local RC–SFR Relation

Next we turn to the local correlation between the Σ_{SFR} as measured from the RC emission and hybrid SF tracers. For this we use the pixel-by-pixel data measured as described in Section 3.4. In Figure 3 we show the result for NGC 6946. We plot the Σ_{SFR} of the RC emission as a function of the hybrid Σ_{SFR} at scales of both 1.2 kpc and 0.7 kpc. We chose these scales to maximize the numbers of galaxies for each scale, depending on their distance and angular resolution, so that we can test whether our results are sensitive to the actual spatial resolution used. Both Σ_{SFR} are shown on a logarithmic scale. In this double logarithmic plot a clear correlation between the radio and hybrid Σ_{SFR} is visible at both scales. The correlation as expected from the Condon relation is shown as a black dashed line. For NGC 6946 most data points lie above the Condon relation. This is expected as this galaxy is radio bright, i.e., has a ratio of radio to hybrid Σ_{SFR} of $\mathcal{R}_{\text{int}} = 1.3$ as measured in Section 4.1.

Motivated by the observation of a correlation between the radio and hybrid Σ_{SFR} , we use the following representation of the radio Σ_{SFR} as a function of the hybrid Σ_{SFR} :

$$\log_{10}((\Sigma_{\text{SFR}})_{\text{RC}}) = \delta \cdot \log_{10}((\Sigma_{\text{SFR}})_{\text{hyb}}) + \epsilon, \quad (8)$$

where δ and ϵ are constants. This definition is equivalent to the one given in Section 4.2 (Equation (5)).

In Figure 3 we show the result of a fit to the pixel-by-pixel data for NGC 6946 as a red solid line in both the 1.2 and 0.7 kpc scale plots. The line is a fit to the data: the deviation of the data points represents typically a factor of two from the fit. The measured slope for the data in NGC 6946 is $\delta = 0.79 \pm 0.03$ at a scale of 1.2 kpc and $\delta = 0.71 \pm 0.01$ at 0.7 kpc. The fit has a slope significantly smaller than one, the value expected from the Condon relation.

The results for the rest of our sample are similar to NGC 6946 in the sense that they all have sub-linear slopes. The average of all galaxies at 1.2 kpc scale is $\langle \delta \rangle = 0.63 \pm 0.25$ for the total emission and $\langle \delta_{\text{nt}} \rangle = 0.61 \pm 0.29$ for the non-thermal emission alone. Errors are standard deviation and give thus the typical deviation of the slope for a particular galaxy from the mean. At a scale of 0.7 kpc we find $\langle \delta \rangle = 0.63 \pm 0.22$ for the total emission and $\langle \delta_{\text{nt}} \rangle = 0.58 \pm 0.22$ for the non-thermal emission alone. The results for the two scales thus virtually agree. We also note that the results for the non-thermal emission alone show only marginally more shallow slopes than for the total emission.

We found a slope δ between 0.22 and 1.21 for the 12 galaxies in our sample for which we have 1.2 kpc spatial resolution. The flattest slopes are found in NGC 3198 (0.22) and Holmberg II (0.26), whereas the steepest (and the only super-linear slope) is found in IC 2574 (1.21).

The sub-linear slopes mean that within an individual galaxy data points at low hybrid Σ_{SFR} are slightly more radio bright than expected from a linear correlation. In Figure 1 we color coded all data points in NGC 6946 depending on their radio spectral index between $\lambda\lambda$ 22 and 18 cm. Data points with “young” non-thermal spectral indices ($\alpha \geq -0.75$), color coded in red, are lying predominantly to the right-hand side at high Σ_{SFR} ; data points with “old” non-thermal spectral indices ($\alpha < -1.2$), color coded in blue, are lying almost exclusively at the left-hand side at low Σ_{SFR} . Green data points with intermediate spectral indices ($-0.75 > \alpha \geq -1.2$) lie in between at medium Σ_{SFR} . It is remarkable how well the data points separate depending on their radio spectral index, at both 1.2

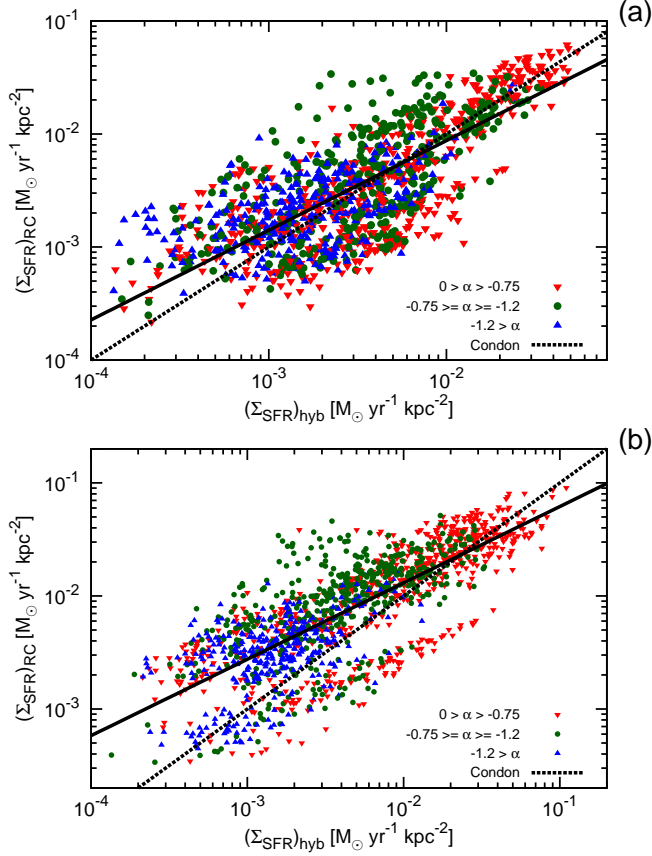


Figure 6. Cumulative pixel-by-pixel plot of all galaxies at 1.2 kpc (upper panel a) and 0.7 kpc (lower panel b) resolution, where we present the radio Σ_{SFR} as function of hybrid Σ_{SFR} . The dashed line shows the one-to-one Condon relation and the solid line is a linear least-square fit to the data points. Red data points indicate a “young” non-thermal spectral index ($\alpha > -0.75$), blue data points an “old” non-thermal spectral index ($\alpha < -1.2$) and green data points a non-thermal spectral index of intermediate age ($-0.75 \geq \alpha \geq -1.2$). The typical uncertainties for the radio spectral index are 0.4, 0.2 and 0.1 for the blue, green, and red data points respectively.

and 0.7 kpc scales. Combined with our result of sub-linear slopes, for NGC 6946 we have $\delta = 0.79 \pm 0.03$, and we find that data points dominated by old CREs have large ratios \mathcal{R} compared to the average, whereas data points dominated by young CREs have low ratios \mathcal{R} . This result should be taken only in a relative sense, as NGC 6946 is radio bright overall with respect to integrated RC emission ($\mathcal{R}_{\text{int}} = 1.3$), most data points lying above the Condon relation.

In our sample at 1.2 kpc scale, with 12 galaxies, four are showing this clear separation of the data points in the pixel-by-pixel plots depending on the radio spectral index. These are NGC 2403, NGC 4736, NGC 5194, and NGC 6946. A fifth galaxy, NGC 2976, has data points that may be separated a bit less clearly than in the other galaxies. In all cases, data points with young non-thermal spectral indices are relatively radio dim, whereas data points with “old” non-thermal spectral indices are radio bright. CREs diffusing away from SF sites undergo spectral aging, resulting in a steeper observed radio spectral index. This could explain our observed results, which we will discuss in more detail in Section 5.2.

In Figure 6(a) we show the cumulative pixel-by-pixel plot for all galaxies combined at a scale of 1.2 kpc. We have color coded the radio spectral index as before, with red data points indicating a “young” non-thermal radio spectral index, green

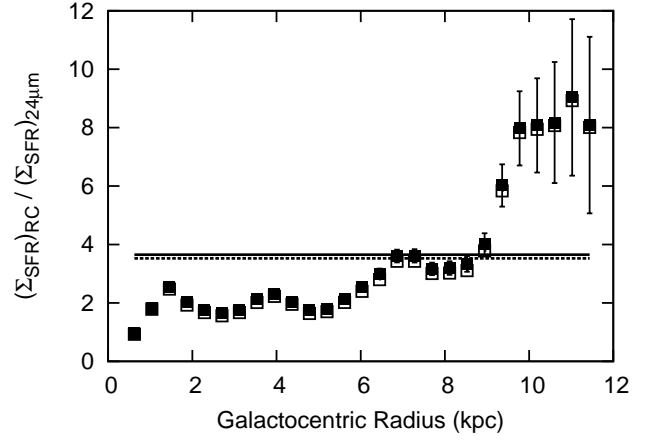


Figure 7. NGC 6946. Ratio $\mathcal{R}_{24\mu\text{m}}$ of radio Σ_{SFR} to the Σ_{SFR} as derived from *Spitzer* 24 μm alone. Open symbols represent the non-thermal RC emission alone. The solid (dashed) line shows the least-squares fit assuming a constant ratio (for the non-thermal RC alone). To be compared with Figure 2(b).

data indicating an intermediate age, and blue data points indicating an “old” non-thermal spectral index. We show the relation as expected from Condon’s relation as a solid black line. We fitted the data shown as a dashed line where we found $\delta = 0.79 \pm 0.02$ and $\epsilon = -0.47 \pm 0.04$. Obviously, the spread around the fit is significantly larger than within individual galaxies. This is due to galaxies having integrated ratios \mathcal{R}_{int} that vary by a factor of 2. For hybrid Σ_{SFR} of $\approx 10^{-2} M_{\odot} \text{ yr}^{-1} \text{ kpc}^{-2}$, the spread becomes smaller, though, and the data points mostly agree within a factor of 2–3 with the Condon relation. For these high Σ_{SFR} the radio spectral index is predominantly of a “young” non-thermal radio spectral index with $\alpha \geq -0.75$. We note that the radio spectral index of most young supernova remnants is between -0.5 and -0.6 (Green 2009), so that even in these areas we have some contribution from an aged population of CREs.

Figure 6(b) shows the cumulative pixel-by-pixel plot for all galaxies at a scale of 0.7 kpc, which is otherwise identical to Figure 6(a). Due to the smaller number of galaxies, there is a gap where one galaxy (NGC 2403) is clearly radio dim in comparison to the other galaxies. A least-squares fit to the data gives $\delta = 0.68 \pm 0.01$ and $\epsilon = -0.53 \pm 0.03$. Hence, the slope is less steep than at 1.2 kpc resolution. This can possibly be explained by cosmic-ray transport within the disk, which we discuss in Section 5.2.

4.4. The Importance of FUV as an SF Tracer

The 24 μm MIR emission can be used as an SF indicator in regions dominated by molecular gas where the associated dust absorbs the UV photons from young stars. This is predominantly the case in the inner H_2 dominated parts of galaxies. In the outer parts, where the dust column density is lower, young stars can be better traced directly by their UV emission as traced by the *GALEX* FUV maps. This is shown in Leroy et al. (2008), where the Σ_{SFR} maps of NGC 6946 based on MIPS 24 μm only and on *GALEX* FUV emission only are presented (their Appendix F).

To quantify the importance of FUV as an SF tracer in addition to MIR emission, we carried out the same analysis as explained in Sections 4.2 and 4.3, namely, that of the radial and pixel-by-pixel behavior of the SF based on the MIPS 24 μm emission alone. This is in principle equivalent to measuring the local ratio of RC to 24 μm MIR intensities,

$$q_{24} \equiv \log_{10}(I_{22\text{ cm}}/I_{24\text{ }\mu\text{ m}}).$$

Figure 2 shows that the hybrid Σ_{SFR} based on a linear combination of FUV and $24\text{ }\mu\text{ m}$ follows much better the radio Σ_{SFR} than the $24\text{ }\mu\text{ m}$ emission alone. The MIR starts to drop considerably at larger radii beyond 8 kpc where the FUV emission becomes important out to a galactocentric radius of 12 kpc. At small radii, within 5 kpc, $24\text{ }\mu\text{ m}$ emission dominates over FUV, and at intermediate radii between 5 and 8 kpc both contribute similar amounts to the hybrid Σ_{SFR} . The ratio of RC to $24\text{ }\mu\text{ m}$ emission shown in Figure 7 is thus not constant to the same degree with galactocentric radius as is the ratio of radio to hybrid Σ_{SFR} . The relative radial variation is only 18% for the RC to hybrid ratio, whereas it is 66% for the RC to $24\text{ }\mu\text{ m}$ ratio. This difference is also found in the galaxies in the rest of the sample. The averaged relative radial variation of the RC to $24\text{ }\mu\text{ m}$ ratio is 35% for the total RC emission and reaches 40% for the non-thermal emission alone. This compares with 25% (28%) for the radio (non-thermal) to hybrid Σ_{SFR} ratio.

MIR $24\text{ }\mu\text{ m}$ emission on its own is not sufficient for use as an SF tracer. The ratio of RC to $24\text{ }\mu\text{ m}$ MIR emission, q_{24} , is not constant and, if used at all, is only a valid tracer within the H_2 dominated region in a galaxy.

5. DISCUSSION

5.1. Global RC–SFR Relation

The RC–SFR relation holds globally, and the RC emission derived SFR is to a good approximation linearly proportional to the SFR as measured by the hybrid SF tracers (Section 4.1). This essentially implies that the ratio \mathcal{R}_{int} of SFRs measured by the RC to hybrid SF tracers is constant within our entire sample of galaxies. We do not find any obvious correlation with any of the fundamental global galaxy parameters as shown in Appendix A. We note that we only find a factor of $\pm 50\%$ variation in the integrated ratio \mathcal{R}_{int} across our galaxy sample. This factor could be easily accounted for by the uncertainty in the hybrid SF tracer as discussed in detail in Leroy et al. (2012).

As has been mentioned in Section 1, the Condon relation is based on a calorimetric model. In this case the RC emission is proportional to the CRE production rate, which is proportional to the frequency of Type II supernovae and hence also proportional to the SFR. Cosmic rays are assumed to be trapped long enough within a galaxy so that their radiation timescale (set by synchrotron and IC losses) is shorter than their escape time. Also, it is assumed that CRE emit a constant fraction of synchrotron relative to IC radiation. Furthermore, one has to account for the various timescales that can influence the validity of the RC–SFR relation. The fastest timescale is that of O stars with a few 10^6 yr that emit the ionizing UV radiation and are responsible for creating and sustaining the H II regions. The thermal RC emission has hence the same short timescale. Similarly, the $24\text{ }\mu\text{ m}$ MIR emission stems from heating by O stars and has the same short timescale. The *GALEX* emission traces FUV emission as emitted by O and B stars with a timescale of 10–100 Myr. The RC emission has the longest timescale, assuming that stars above a mass of $\approx 8\text{ }M_{\odot}$ evolve into a Type II supernova (Heger et al. 2003), which do have a lifetime of a few 10^7 yr. This is the time the RC emission needs to ramp up after a single starburst. Furthermore, in contrast to the other tracers that vanish once the O and B stars have gone off as a Type II supernova, the RC emission decays slowly. For a

typical magnetic field strength of $B = 8\text{ }\mu\text{G}$, the CRE lifetime due to synchrotron radiation is 3×10^7 yr. In order for the RC–SFR relation to work, there has to be a quasi-steady state resulting in a constant or slowly varying SFR over time. In most galaxies this condition is fulfilled when averaging over areas that are ≈ 1 kpc or larger, which ensures an ensemble of SF regions at any one time. This assumption of course definitely holds in spiral galaxies, when investigated globally. It becomes, however, an issue with dwarf irregular galaxies, which have a more burst-like SF history.

Galaxies can differ from the idealized calorimetric model in several ways. Firstly, cosmic rays can escape in a galactic wind or by diffusion along vertical magnetic field lines (e.g., Heesen et al. 2009a,b). Secondly, the ratio of the magnetic to photon energy density may vary, resulting in a change of synchrotron to IC radiation losses. The non-calorimetric model by Niklas & Beck (1997) addresses the escape of CREs in an elegant way. They assume that the strength of the magnetic field is related to the gas mass and hence to the SFR, assuming a Kennicutt–Schmidt SF law. The magnetic field regulates the energy content that is stored in the CREs. This makes sense, as it is known that the cosmic-ray energy density (including CREs and the dominating proton component) and the magnetic field energy density are approximately in energy equipartition (e.g., Beck et al. 1996; Beck & Krause 2005). This is motivated by the fact that too large a cosmic-ray energy density would give rise to a Parker instability where the relativistic gas with its buoyancy escapes from the disk. Also, the total energy stored in the magnetic field and cosmic rays together is close to the minimum value in case of energy equipartition.

Energy equipartition is a hotly debated subject. The best evidence in support of it comes from gamma-ray observations, which allow us to directly derive the CRE spectrum and hence measure the CRE energy density. Strong et al. (2011) used *Fermi*–LAT observations to determine the magnetic field strength at the position of the Sun as $B_{\text{ran}} = 7.5\text{ }\mu\text{G}$ (for the dominating random component). The non-thermal RC model of the Milky Way by Beuermann et al. (1985) can be used to derive the magnetic field strength assuming equipartition as $6 \pm 2\text{ }\mu\text{G}$ at the solar radius (Berkhuijsen, in Beck 2001). Sun et al. (2008) found $4\text{ }\mu\text{G}$ using rotation measures of polarized background sources. For external galaxies there are only a handful of detections in gamma-ray emission, which do suggest energy equipartition in the Large Magellanic Cloud (Mao et al. 2012), a dwarf irregular galaxy, and in the starburst galaxies NGC 253 (Rephaeli et al. 2010) and M82 (Yoast-Hull et al. 2013). For starburst galaxies the assumption of energy equipartition may give the true magnetic field strength only by sheer coincidence (Lacki & Beck 2013), but staying away from those, for our sample of normal star-forming galaxies the assumption of equipartition is a reasonable one. In the following we will discuss aspects of the calorimetric model by Völk (1989) and the non-calorimetric model by Niklas & Beck (1997).

5.1.1. Inverse Compton Losses

The calorimetric model predicts that the ratio \mathcal{R}_{int} of radio to hybrid SFR is proportional to the inverse of $1 + U_{\text{rad}}/U_{\text{B}}$, where U_{rad} is the radiation energy density and U_{B} the magnetic field energy density. This is motivated by the fact that the ratio of IC to synchrotron radiation of CREs is proportional to the ratio of radiation to magnetic field energy density, $U_{\text{rad}}/U_{\text{B}}$. We calculated the radiation energy density U_{rad} us-

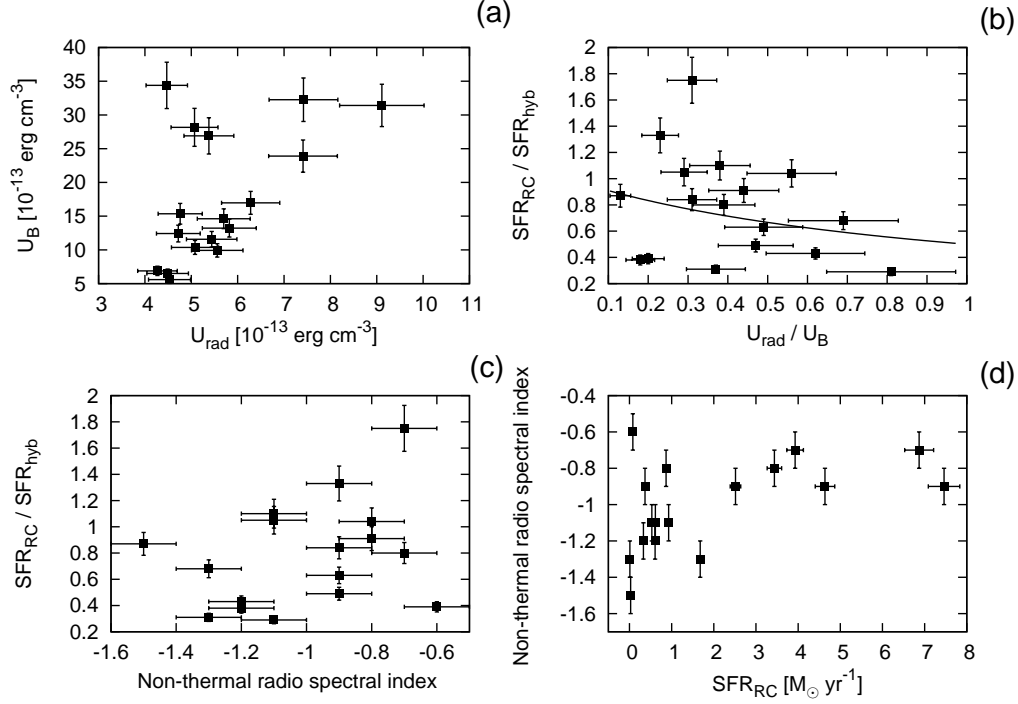


Figure 8. Test of the calorimetric model. (a) Magnetic field energy density U_B as a function of radiation energy density U_{rad} . (b) Ratio \mathcal{R}_{int} of integrated radio to hybrid SFR as a function of ratio of radiation energy density to magnetic field energy density. The solid line shows the theoretical expectation. (c) Ratio \mathcal{R}_{int} of integrated radio to hybrid SFR as a function of the integrated non-thermal radio spectral index. (d) Non-thermal radio spectral index as a function of the radio SFR.

Table 3
Data to Test the Calorimetric Model.

Galaxy	U_{rad} ($10^{-13} \text{ erg cm}^{-3}$)	U_{rad}/U_B	α_{nt}
(1)	(2)	(3)	(4)
Ho II	5.2	0.11	-1.5 ± 0.1
IC 2574	1.0	0.29	-1.3 ± 0.1
NGC 628	5.9	0.35	-1.1 ± 0.1
NGC 925	4.7	0.58	-1.2 ± 0.1
NGC 2403	6.9	0.16	-1.2 ± 0.1
NGC 2841	5.3	0.65	-1.3 ± 0.1
NGC 2903	6.0	0.30	-0.9 ± 0.1
NGC 2976	7.7	0.19	-0.6 ± 0.1
NGC 3184	8.2	0.53	-0.8 ± 0.1
NGC 3198	5.4	0.79	-1.1 ± 0.1
NGC 3627	8.6	0.38	-0.7 ± 0.1
NGC 4736	1.8	0.27	-1.1 ± 0.1
NGC 4826	7.9	0.44	-0.9 ± 0.1
NGC 5055	8.9	0.43	-0.8 ± 0.1
NGC 5194	1.3	0.31	-0.7 ± 0.1
NGC 6946	1.3	0.22	-0.9 ± 0.1
NGC 7331	6.9	0.48	-0.9 ± 0.1

Note. — Column 1: galaxy name; Column 2: radiation energy density; Column 3: ratio of radiation energy density to magnetic field energy density; Column 4: non-thermal radio spectral index between $\lambda\lambda$ 22 and 18 cm.

ing the FIR luminosity L_{FIR} from Galametz et al. (2013). For NGC 2403 and NGC 5194 we obtained the FIR luminosity from Draine et al. (2007) and for NGC 2903 from Sanders et al. (2003). After correcting for our distances and excluding nuclear starbursts and background galaxies, the FIR radiation energy density can be calculated as $U_{\text{rad,FIR}} = L_{\text{FIR}} / (2\pi r_{\text{int}}^2 c)$. Here, r_{int} is the galactocentric radius of the galaxy to which we integrated the radio flux densities, and c is the speed of light. We have to add $U_{\text{CMB}} = 4.1 \times 10^{-13} \text{ erg cm}^{-3}$, the radiation en-

ergy density of the cosmic microwave background (CMB) at redshift zero, and the stellar radiation energy density $U_{\text{rad,stars}}$. Following Tabatabaei et al. (2013b), we scaled $U_{\text{rad,stars}}$ to the FIR radiation energy density via $U_{\text{rad,stars}} = 1.73 \times U_{\text{rad,FIR}}$, which is obtained from the values for the Milky Way in the solar neighborhood (Mathis et al. 1983; Draine 2011). Resulting radiation energy densities are tabulated in Table 3. We calculated the magnetic field energy density using the equipartition approximation between the cosmic-ray and magnetic field energy density (Beck & Krause 2005). We used the usual assumption for the proton-to-electron ratio, $k = 100$, which is the observed value in the solar system as direct measurements of the cosmic-ray proton and electron fluxes show (Adriani et al. 2011; Shikaze et al. 2007). For the integration length (vertical to the galactic plane) we chose 1 kpc and for the non-thermal spectral index $\alpha_{\text{nt}} = -0.85$. Resulting ratios U_{rad}/U_B of radiation energy density to the magnetic field energy density are tabulated in Table 3.

The average magnetic field energy density is $\langle U_B \rangle = 2.8 \times 10^{-12} \text{ erg cm}^{-3}$ (corresponding to $\langle B \rangle = 8.4 \mu\text{G}$), the average radiation energy density is $\langle U_{\text{rad}} \rangle = 8.4 \times 10^{-13} \text{ erg cm}^{-3}$, and the average ratio is $\langle U_{\text{rad}}/U_B \rangle = 0.38$. This is a similar result to that of Niklas (1995), who found an average magnetic field energy density of $\langle U_B \rangle = 3.2 \times 10^{-12} \text{ erg cm}^{-3}$ in his sample. Firstly, we can test whether the ratio U_{rad}/U_B is constant within our sample. For this we plot in Figure 8(a) the dependence of U_B as a function of U_{rad} . There is no clear correlation between them, resulting in a spread of the ratio U_{rad}/U_B , which ranges between 0.11 (Holmberg II) and 0.79 (NGC 3198). Because of the rather small ratio $\langle U_{\text{rad}}/U_B \rangle = 0.38$, we expect only a spread of $\pm 40\%$ in the RC luminosity. This is comparable to the uncertainty of $\pm 50\%$ in the integrated SFRs from the hybrid SF tracer. Hence, we cannot expect to detect a clear influence of IC radiation on the RC

in comparison to the hybrid SFR. In Figure 8(b) we present the ratio \mathcal{R}_{int} of radio to hybrid SFR as a function of the ratio $U_{\text{rad}}/U_{\text{B}}$ and as a line the theoretical expectation from the inverse of $1 + U_{\text{rad}}/U_{\text{B}}$ normalized to our observed averaged ratio $\langle \mathcal{R}_{\text{int}} \rangle = 0.8$. We can see that the scatter of the ratio \mathcal{R}_{int} is indeed too high to be solely explained by a variation of the IC radiation in comparison to synchrotron radiation.

5.1.2. Cosmic-ray Escape

The other possibility to explain a variation in the RC luminosity in comparison to the SFR is the escape of CREs in a galactic wind. This can be tested by using the non-thermal radio spectral index as a tracer for the CRE escape fraction (Lisenfeld & Völk 2000). Radiation losses (synchrotron and IC) steepen the spectral index with time, because electrons with the highest energies lose their energy fastest. In contrast, adiabatic losses that occur in an accelerated outflow where the relativistic cosmic-ray gas loses energy by PdV work on the interstellar medium leave the radio spectral index unchanged as these losses are directly proportional to the cosmic-ray energy. In our sample of galaxies the gas densities are not high enough to cause cosmic-ray ionization losses that are important in starburst galaxies (Thompson et al. 2006). Hence, if CREs are contained within a galaxy, radiation losses should be important and the non-thermal radio spectral index should be steep, $\alpha_{\text{nt}} < -1.2$. On the other hand, if adiabatic losses are important or CREs can escape freely, the observed electron spectral index should be identical to the injection spectral index (Lisenfeld & Völk 2000). In this case we expect a “young” non-thermal radio spectral index of $\alpha_{\text{nt}} \approx -0.6$.

Our galaxies have an averaged radio spectral index of $\alpha = -0.88 \pm 0.22$, and the averaged non-thermal radio spectral index is $\alpha_{\text{nt}} = -0.99 \pm 0.22$. This is steeper than what Niklas et al. (1997) found in their sample with $\alpha_{\text{nt}} = -0.83$, who used integrated un-resolved flux densities. However, their measurements are between $\lambda\lambda$ 20 and 3 cm, so that their non-thermal radio spectral index is more appropriate for intermediate wavelengths such as λ 6 cm. A non-thermal radio spectral index of $\alpha_{\text{nt}} = -1.0$ would be indicative of almost no escape of CREs, so that the galaxy is an effective electron calorimeter. However, some of our galaxies have spectral indices that are in agreement with a “young” non-thermal spectral index ($\alpha \geq -0.7$), possibly indicative of an almost free CRE escape, whereas other galaxies have a fairly steep spectral index $\alpha \leq -1.1$ possibly caused by high CRE radiation losses. Hence, we can test whether this spread has an influence on RC–SFR correlation. This is shown in Figure 8(c), where we present the ratio \mathcal{R}_{int} as a function of the non-thermal radio spectral index. It can be seen that there is no correlation between them. The calorimetric model predicts that for higher SFRs the radio spectral index should be steeper. This is tested in Figure 8(d), where no such correlation is detected. In summary, the non-thermal spectral indices suggest that CREs can indeed escape from galaxies in a galactic wind. This argues against the calorimetric model.

5.1.3. Magnetic Field–Gas Relation

Niklas & Beck (1997) found a correlation between the non-thermal RC luminosity and the integrated mass of atomic hydrogen M_{HI} . Assuming equipartition, they concluded that the magnetic field correlates with the mass surface density as $B \propto \Sigma_{\text{HI}}^{0.48 \pm 0.05}$. Using $I_{\nu} \propto B^{3-\alpha_{\text{nt}}}$, we expect a relation between the RC luminosity (and thus the radio SFR) and

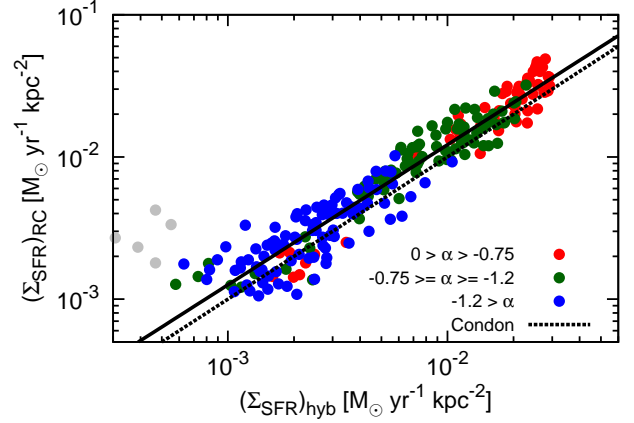


Figure 9. Resolved RC–SFR relation in NGC 6946 with a pixel size of 1.2 kpc. The hybrid Σ_{SFR} map was convolved with a Gaussian kernel of 3.4 kpc to simulate cosmic-ray diffusion. The dashed line shows the one-to-one Condon relation, and the solid line is a linear least-squares fit to the data points. Red data points indicate a “young” non-thermal spectral index ($\alpha > -0.75$), blue data points an “old” non-thermal spectral index ($\alpha < -1.2$), and green data points a non-thermal spectral index of intermediate age ($-0.75 \geq \alpha \geq -1.2$). The typical uncertainties for the radio spectral index are 0.4, 0.2, and 0.1 for the blue, green, and red data points, respectively. Gray data points were excluded from the least-squares fit.

the atomic hydrogen mass as $\text{SFR}_{\text{RC}} \propto M_{\text{HI}}^{1.8}$, a significantly super-linear relation. This is in agreement with the Kennicutt–Schmidt relation, which predicts a super-linear relation between the integrated SFR and the atomic hydrogen (and possibly also dense molecular hydrogen) mass as $\text{SFR} \propto M_{\text{HI,H2}}^{1.5}$ (Kennicutt & Evans 2012).

We tested for our sample the relation between the radio SFR and the masses of atomic and molecular hydrogen (separately and for the sum of both; see Appendix A), but we find no clear correlation with a dispersion much larger than what we observe for the RC–SFR relation. Our sample is probably too small to test the integrated SFR–gas relation, where the spread in the data points is dominating the estimate of the slope. However, since we find a tight integrated RC–SFR relation, we can derive a magnetic field–gas relation, if we assume a local Kennicutt–Schmidt relation between the gas mass surface density Σ_{gas} and Σ_{SFR} (Section 5.4).

5.2. RC–SFR Relation on a 1 kpc Scale

The RC–SFR relation when integrating over entire galaxies is almost linear; however, on a 1 kpc scale we find that the RC–SFR slopes are significantly sub-linear. This is explored in the following.

5.2.1. Cosmic-ray Diffusion

Cosmic rays diffuse away during their Lifetime, while massive stars will be hardly moving from their birth place. We thus expect the RC image to be smeared out with respect to the hybrid Σ_{SFR} map (Murphy et al. 2006a,b, 2008), explaining the sub-linear slopes of our pixel-by-pixel plots: the RC emission is suppressed at the peaks of the SF distribution, because the CREs have diffused away from the SF sites. In contrast, away from the SF sites we see, relatively speaking, more RC emission than we would expect from the hybrid Σ_{SFR} . The former situation we find in spiral arms, whereas the latter situation we find in the inter-arm regions. Berkhuijsen et al. (2013) studied the RC–SFR correlation in M31 and M33 and found also sub-linear slopes. They convolved the thermal

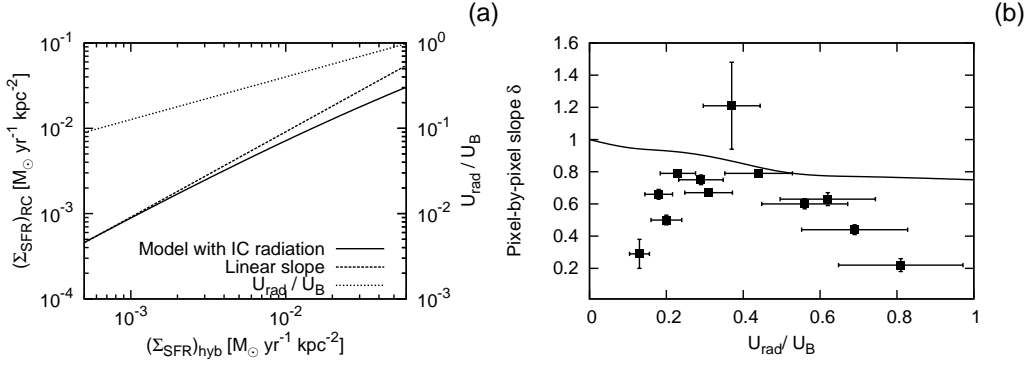


Figure 10. (a) Model for the resolved RC–SFR relation, where the ratio $U_{\text{rad}}/U_{\text{B}}$ of the radiation energy density to the magnetic field energy density is a function of the hybrid Σ_{SFR} . At high $(\Sigma_{\text{SFR}})_{\text{hyb}}$ the RC emission is suppressed, because cosmic-ray electrons emit predominantly inverse Compton (IC) radiation. (b) Slope of the pixel-by-pixel plots as a function of the ratio of radiation energy density to magnetic field energy density. The line shows the predicted slope when including IC radiation.

RC map—assuming it to be a representation of Σ_{SFR} —with a Gaussian kernel, so that the RC–SFR relation becomes linear, and use this as an estimate for the cosmic-ray diffusion length. We tested this by convolving the hybrid Σ_{SFR} map with a Gaussian 3.4 kpc kernel to simulate a diffusion length of 1.7 kpc, half the width of the convolving kernel. This is presented in Figure 9, which shows a slope of 0.99 ± 0.02 , a linear RC–SFR relation within the uncertainty. Our results hence agree with those by Tabatabaei et al. (2013b), who also found a diffusion length of 1.7 kpc in NGC 6946.

The explanation of sub-linear slopes with cosmic-ray transport is corroborated by our finding in Section 4.3, where the pixel-by-pixel plots in about half of our sample show that the data points can be characterized by their radio spectral index: data points at low Σ_{SFR} (radio and hybrid) have steeper non-thermal spectral indices, indicating older CREs. The opposite is true for high Σ_{SFR} , where, at sites of current SF, the radio spectral index is $\alpha \approx -0.6$, similar to that measured in supernova remnants (Green 2009). As CREs lose their energy mainly by synchrotron and IC losses, both processes having loss rates $\propto E^2$, the CREs with the highest energies lose their energy fastest. This results in a steepening of the electron spectral index with time and hence also in the radio spectral index. In the pixel-by-pixel plots we find that data points with steep spectral indices (old CREs) are relatively radio bright and data points with flatter spectral indices (young CREs) are relatively radio dim as expected for cosmic-ray transport.

Our discussion would be incomplete without at least mentioning the influence of the magnetic field structure on cosmic-ray diffusion. The galaxies in our sample have spiral magnetic fields with pitch angles of typically 20° (Heald et al. 2009). In galaxies, the ordered component of the magnetic field has a strength that is comparable to the turbulent component, so that anisotropic diffusion along the ordered magnetic field is the most likely transport scenario (e.g., Tabatabaei et al. 2013a). Thus, we can speculate that radial diffusion may be suppressed in comparison to azimuthal diffusion. This would explain why the ratio \mathcal{R} has only quasi-periodic fluctuations as a function of galactocentric radius (Section 4.2). However, a more quantitative study of the influence of the magnetic field structure on the cosmic-ray diffusion would be necessary in order to affirm this conclusion.

5.2.2. Inverse Compton Radiation

As we have seen in Section 5.1, the variation of radiation energy density to magnetic field energy density, $U_{\text{rad}}/U_{\text{B}}$, is

globally not large enough to explain the fluctuations in the integrated ratio \mathcal{R}_{int} of RC luminosity to hybrid SFR. Locally, however, this may be different as the variation of $U_{\text{rad}}/U_{\text{B}}$ within an individual galaxy can be much larger.

As a first-order approximation, the radiation energy density scales with the hybrid Σ_{SFR} as $U_{\text{rad}} \propto (\Sigma_{\text{SFR}})_{\text{hyb}}$. The radiation energy density from dust is proportional to the hybrid Σ_{SFR} , and the stellar radiation field is assumed to scale also with the hybrid Σ_{SFR} and neglecting the constant background radiation field of CMB. On the other hand, the magnetic field energy density scales with the hybrid Σ_{SFR} as $U_{\text{B}} \propto (\Sigma_{\text{SFR}})_{\text{hyb}}^{2\zeta/(3-\alpha_m)}$. With $\alpha_m = -0.85$ and $\zeta = 1.11$ we have $U_{\text{B}} \propto (\Sigma_{\text{SFR}})_{\text{hyb}}^{0.58}$. The ratio $U_{\text{rad}}/U_{\text{B}}$ hence scales approximately as $U_{\text{rad}}/U_{\text{B}} \propto (\Sigma_{\text{SFR}})_{\text{hyb}}^{0.5}$. We note that this is an upper limit, as the stellar radiation field probably does not depend as much on the hybrid Σ_{SFR} as the re-radiated FIR emission from dust. The typical range of the hybrid Σ_{SFR} is a factor of 100, between the peak Σ_{SFR} and the lowest Σ_{SFR} in outskirts and inter-arm regions, so that the ratio $U_{\text{rad}}/U_{\text{B}}$ may change by as much as a factor of 10 within a single galaxy. As the RC luminosity scales with the inverse of $1 + U_{\text{rad}}/U_{\text{B}}$, we expect a variation of the RC–SFR relation. At the peaks of the hybrid Σ_{SFR} the RC intensity will be slightly suppressed, because some of the energy of the CREs is radiated via IC radiation.

In Figure 10(a) we show the expected RC intensity as a function of the hybrid Σ_{SFR} for average ratio across our sample $\langle U_{\text{rad}}/U_{\text{B}} \rangle = 0.38$ and a typical Σ_{SFR} range. It can be seen that $U_{\text{rad}}/U_{\text{B}}$ varies between 10% at the lowest Σ_{SFR} and 100% at the highest Σ_{SFR} , resulting in an RC decrease of a factor of two as compared to a linear extrapolation. For higher ratios of $U_{\text{rad}}/U_{\text{B}}$ we expect an increased effect on the pixel-by-pixel slopes. This is tested in Figure 10(b), where we plot the pixel-by-pixel slopes as a function of integrated ratio $U_{\text{rad}}/U_{\text{B}}$ within individual galaxies. For comparison, we also plot the expected slopes for our model including IC radiation. The model can explain a small fraction of the sub-linear slopes but not all of it. For $U_{\text{rad}}/U_{\text{B}} = 0.1$, as in NGC 6946, we find a slope of 0.9, and only for ratios $U_{\text{rad}}/U_{\text{B}} > 0.5$ we do find slopes of 0.8. IC losses alone therefore cannot explain the sub-linear slopes, but they reduce the required cosmic-ray transport lengths.

5.3. Cosmic-ray Transport

5.3.1. Disk-parallel Cosmic-ray Transport

We can now try to parameterize the cosmic-ray transport as a function of the hybrid Σ_{SFR} . The CRE lifetime scales as $t_{\text{syn}} \propto E^2 B^2$, assuming that synchrotron losses dominate as shown in Section 5.1. The synchrotron emission of a single CRE has a broad peak at the critical frequency, so that we can relate the CRE energy via $E \propto B^{-1/2}$ to the magnetic field strength, resulting in $t_{\text{syn}} \propto B^{-3/2}$. On the other hand, cosmic rays are transported by diffusion as long as there is no galactic wind, which is important for transport in the vertical direction only. For cosmic-ray diffusion one has $L_{\text{diff}}^2/t_{\text{syn}} = D$, where L_{diff} is the transport length and D is the diffusion coefficient. The energy dependence of the diffusion coefficient is normally assumed to be $D \propto E^\kappa$ with $\kappa = 0.5$ for Kolmogorov-type turbulence. The diffusion length $L_{\text{diff}} = (D \cdot t_{\text{syn}})^{1/2}$ scales hence as $L_{\text{diff}} \propto B^{-(3+\kappa)/4}$. In Section 5.4 we will find the relation $B \propto \text{SFR}_{\text{hyb}}^{0.30}$, so that we find for dependence of the diffusion length $L_{\text{diff}} \propto \text{SFR}_{\text{hyb}}^{-0.26}$, where we take the global magnetic field strength for the average value of the CRE lifetime.

This can be compared with observations such as of Murphy et al. (2008), who measured the diffusion length in the WSRT SINGS galaxy sample. They studied the dependence of L_{diff} on the radiation energy density, which they derived from the FIR luminosity divided by the physical area of the galaxy disk (similar to our approach in Section 5.1). Following for this part of the discussion their assumption of a direct proportionality between the hybrid SFR and FIR luminosity (although probably not strictly true), their result is $L_{\text{diff}} \propto (\Sigma_{\text{SFR}})_{\text{hyb}}^{-0.5}$, significantly steeper than what our simple estimate above indicates. However, Tabatabaei et al. (2013a) find no such strong dependence on Σ_{SFR} and argue that the diffusion length is mainly determined by the magnetic field structure. This is a sensible assumption, observing that diffusion along magnetic field lines is faster and measured diffusion coefficients can be large such as $2.0 \times 10^{29} \text{ cm}^2 \text{ s}^{-1}$ (in NGC 253, Heesen et al. 2009a). On the other hand, Heesen et al. (2011) found a much smaller diffusion coefficient of $3.0 \times 10^{28} \text{ cm}^2 \text{ s}^{-1}$ in the same galaxy but for perpendicular diffusion, which is in agreement with theoretical considerations (Buffie et al. 2013). Murphy et al. (2012) found an even smaller diffusion coefficient of $1.0 \times 10^{27} \text{ cm}^2 \text{ s}^{-1}$ in the vicinity of 30 Doradus, a massive SF region in the Large Magellanic Cloud. This is probably due to the high degree of turbulence in the magnetic field structure.

5.3.2. Cosmic-ray Transport within Galaxy Halos

Krause (2009) notes that in her sample of edge-on galaxies the scale height of the RC emission at $\lambda 6 \text{ cm}$ is 1.8 kpc, across an SFR span in her sample of a factor of 10. For the same sample, Krause (2011) finds $B = 6 \mu\text{G}$ and a scale height of 1.8 kpc for NGC 3628, whereas in NGC 253 she finds $B = 12 \mu\text{G}$ and a scale height of 1.7 kpc. Our predicted diffusion length of $L_{\text{diff}} \propto B^{-0.88}$, using $\kappa = 0.5$, would predict that the scale height of NGC 253 should be only about half of that of NGC 3628. But the scale height is almost independent of the magnetic field strength, in contrast to our expectation from cosmic-ray diffusion. Tabatabaei et al. (2013a) find that the diffusion lengths in the disks of galaxies do not depend on Σ_{SFR} , which they interpret as support for the non-calorimetric model of Niklas & Beck (1997). If the diffusion length is not a function of Σ_{SFR} and hence the magnetic field strength, the timescale over which the CRE are transported within the disk is not given by the CRE lifetime t_{syn} as measured from synchrotron losses, but by the CRE escape time t_{esc} from the

disk. In this case we have $t_{\text{esc}} < t_{\text{syn}}$ and the electrons escape freely into the halo. The CRE scale heights in the halo are also constant and independent of the magnetic field strength (Krause 2009), further strengthening this argument.

However, the alternative explanation of the larger than predicted vertical scale height in NGC 253 is a galactic wind, which transports cosmic rays convectively from the disk into the halo. This can happen in addition to any transport by diffusion. A distinction whether transport happens via diffusion or convection is the predicted dependence of the scale height on the magnetic field strength. The transport length for convection is $L_{\text{conv}} \propto v_{\text{wind}} \cdot B^{-3/2}$, because the transport length depends in this case only on the electron cooling time here assumed to be dominated by synchrotron radiation losses. So that the global scale height of the RC emission does not depend on the magnetic field strength and thus the SFR, for convective transport the wind speed v_{wind} thus has to increase with $B^{3/2}$ in order to compensate for the shorter loss timescale. To distinguish between convective and diffusive cosmic-ray transport from the disk into the halo, Heesen et al. (2009a) studied the local correlation between the CRE scale height in NGC 253 and the CRE lifetime. In the northeastern halo they favored convection and in the southwestern part diffusion as the dominant mode of transport. Most importantly, they found that the CRE lifetime indeed regulates the local scale height as is expected when synchrotron and IC losses are dominating over the escape of CRE, so that one has in this case $t_{\text{syn}} < t_{\text{esc}}$, which would mean that NGC 253 is a CRE calorimeter. But the non-thermal spectral index of the diffuse RC emission, excluding the nuclear starburst region, is -1.0 between $\lambda \lambda 90$ and 3.6 cm , indicative that some fraction of the CREs still do escape.

NGC 253 seems to be close to the hybrid Σ_{SFR} value where convection in a wind becomes an important transport mode. At even higher hybrid Σ_{SFR} in the nuclear starburst of NGC 253 and in the starburst galaxy M82, the RC scale height is smaller with $\approx 150 \text{ pc}$ at $\lambda 6 \text{ cm}$, indicating that the wind speed does not increase sufficiently to compensate for the shorter electron cooling times (Heesen et al. 2011; Adebahr et al. 2013). These galaxies are supposed to be electron calorimeters as inferred from a comparison of RC and gamma-ray observations (Yoast-Hull et al. 2013). In summary, the cosmic-ray diffusion lengths in the disk and scale heights in the halo argue in favor of a non-calorimetric model. However, it needs more investigation whether the vertical scale heights are at least partially explained by a galactic wind, which may explain the constant vertical scale heights by an increased wind speed due to a higher SFR, compensating the shorter CRE lifetimes.

5.4. Magnetic Field–SFR Relation

As we have seen, the relation between RC emission and the hybrid SFR is markedly different for integrated measurements, where it is a slightly super-linear relation, and resolved measurements on a 1 kpc scale, where it is a significantly sub-linear relation. We attributed this finding largely to the diffusion of CREs within galaxies. We now attempt to reconcile these two findings by proposing a relation between the magnetic field strength and the SFR. Our model can be seen as a variety of the non-calorimetric model by Niklas & Beck (1997), which is based on a magnetic field–gas relation. We assume (1) that the total cosmic-ray energy content of a galaxy relates to the magnetic field strength, so that there is energy equipartition between the cosmic rays and the mag-

netic field and (2) that the magnetic field strength is proportional to the SFR. The second assumption is supported by the theory that magnetic fields are amplified by a turbulent dynamo, and turbulence is mostly stemming from supernovae and hence the SFR (e.g., Cho et al. 2009). Our model is a close corollary of the models of Dumas et al. (2011) and Tabatabaei et al. (2013b), who assume a local magnetic field–gas relation.

Using the assumption of a global energy equipartition between the cosmic rays and the magnetic field, we can express the magnetic field strength by the hybrid SFR as $B \propto \text{SFR}_{\text{hyb}}^{\zeta/(3-\alpha_{\text{nt}})}$, where $\zeta_{\text{nt}} = 1.16 \pm 0.08$ (for the non-thermal RC emission; Section 4.1) and $\alpha_{\text{nt}} = -0.85$. Our result is thus $B \propto \text{SFR}_{\text{hyb}}^{0.30 \pm 0.02}$. This is within the errors consistent with the results of Niklas & Beck (1997), who found $B \propto \text{SFR}^{0.34 \pm 0.08}$, and those of Chyży et al. (2011) who found $B \propto \text{SFR}^{0.25 \pm 0.06}$, for dwarf irregular galaxies. We now assume that this relation holds also locally on a 1 kpc scale, so that we have $B \propto (\Sigma_{\text{SFR}})_{\text{hyb}}^{0.30 \pm 0.02}$. But we have to drop the assumption of local energy equipartition: because of cosmic-ray diffusion, the cosmic-ray energy density is smoothed to a scale of several kpc, depending on the diffusion length scale, which presumably varies in our sample galaxies. In the following, we use the extreme assumption of a constant cosmic-ray energy density on a 1 kpc scale, in order to estimate the minimum expected slope of the non-thermal RC– Σ_{SFR} correlation.

We hence expect a non-thermal RC– Σ_{SFR} correlation as $I_{\text{syn}} \propto B^{1-\alpha_{\text{nt}}} \propto (\Sigma_{\text{SFR}})_{\text{hyb}}^{0.56 \pm 0.04}$. This indeed agrees within the errors with the observed value of $\delta_{\text{nt}} = 0.61 \pm 0.22$. We notice that the slope of 0.56 is a lower limit, because the cosmic-ray energy density probably does still depend slightly on the $(\Sigma_{\text{SFR}})_{\text{hyb}}$.

We can now also relate the magnetic field to the local gas surface density, Σ_{gas} , if we use the known relations between $(\Sigma_{\text{SFR}})_{\text{hyb}}$ and Σ_{gas} (Leroy et al. 2008; Bigiel et al. 2008). They have shown that if the gas is predominantly molecular, $(\Sigma_{\text{SFR}})_{\text{hyb}}$ is directly proportional to the mass surface density Σ_{gas} . If the gas is predominantly atomic, $(\Sigma_{\text{SFR}})_{\text{hyb}}$ depends on Σ_{gas} in a super-linear relation with a slope of 1.5. Thus, we find $B \propto \Sigma_{\text{gas}}^{0.30 \dots 0.45}$, the lower slope for predominantly molecular gas and the higher slope for predominantly atomic gas. This is indeed in good agreement with the result of Niklas & Beck (1997), who found for atomic hydrogen $B \propto M_{\text{HI}}^{0.48 \pm 0.05}$. We notice that a small difference in the slope of either the magnetic field–gas or the magnetic field–SFR relation has a large impact on the slope of the RC–SFR relation, because the non-thermal RC emission depends on the equipartition magnetic field strength as $I_{\text{syn}} \propto B^{3-\alpha_{\text{nt}}}$. Schleicher & Beck (2013) derive a magnetic field–SFR relation of $B \propto \text{SFR}^{1/3}$. This would result in a super-linear RC–SFR relation with $\text{SFR}_{\text{RC}} \propto \text{SFR}_{\text{hyb}}^{1.28}$. Our observed non-thermal slope of $\zeta_{\text{nt}} = 1.16 \pm 0.08$ is slightly super-linear, but not as much as expected from the theory of turbulent magnetic field amplification. A small change, however, of the magnetic field–SFR relation would be sufficient to observe an only slightly super-linear RC–SFR relation as found for our sample, or possibly even a strictly linear RC–SFR relation, which makes RC emission an excellent SF tracer as we discuss below.

It is important to point out that dropping the assumption of local energy equipartition differentiates our results from those of, e.g., Chyży (2008), Dumas et al. (2011), and Tabatabaei et al. (2013b). Using equipartition, they do find flatter slopes

of the magnetic field–SFR and magnetic field–gas relation, even though the slope of the RC–SFR relation is similar to ours. However, firstly, it is instructive to study the extreme case of a constant cosmic-ray energy density on the above relations. The effect of cosmic-ray transport is a smoothing of the corresponding energy distribution over a kpc scale. No such transport is postulated for the magnetic field, so that away from SF sites equipartition is probably not strictly true anymore. Secondly, the appeal of this model lies in a unique magnetic field–SFR and possibly also magnetic field–gas relation that holds both globally and locally. And thirdly, we notice that in our scenario the cosmic-ray energy density is only constant locally, but not globally across our galaxy sample, where it varies as a function of SFR. A constant cosmic-ray energy density, independent of SFR, would require a calorimetric model, which our observations and that of others disfavor (Section 5.1).

5.5. Radio continuum as an SF Tracer

We will now try to summarize what we have learned from our study on how we can use RC emission to determine integrated SFRs or spatially resolved Σ_{SFR} . Firstly, we notice that the Condon relation holds for the integrated RC emission in comparison to the measured SFR from the hybrid SF tracer, the combination of GALEX FUV and *Spitzer* 24 μm MIR emission (Section 4.1). This contains two important sub-results: (1) the radio derived SFR agrees within one standard deviation with the SFR as derived from the state-of-the-art hybrid tracer, (2) the RC luminosity of a galaxy is almost linearly dependent on the SFR as predicted by the Condon relation. We did not find any galaxy parameter, which clearly influences the ratio \mathcal{R}_{int} of radio to hybrid SFR (Section 5.1 and Appendix A). The integrated radio SFR varies by $\pm 50\%$ with respect to the hybrid SFR. As the hybrid SFR has a similar calibration error, we can conclude that for integrated galaxy-wide measurements, the RC emission provides an SFR with similar accuracy as the hybrid FUV/MIR tracer.

For resolved studies, the situation is more complicated. If averaging azimuthally, the profiles of the radio Σ_{SFR} have almost exactly the same shape as the radial profile of the hybrid Σ_{SFR} , only offset by an almost constant factor. We did not find any conclusive radial trends; the ratio \mathcal{R} of radio to hybrid Σ_{SFR} changes quasi-periodically. Furthermore, the relative amplitude of the fluctuations is small, on average across our sample only $\pm 25\%$. This means if one is interested in measuring the radial distribution of SF in galaxies only, again the radio-based method provides with a similar accuracy ($\pm 50\%$) as using the hybrid FUV/MIR tracer.

For resolved studies on a 1 kpc scale, however, one has to be somewhat more cautious. Individual data points lie typically a factor of 2–3 off from the best fit to the data points. This is comparable with the small-scale scatter of the hybrid FUV/MIR tracer (Leroy et al. 2012). Hence, on a 1 kpc scale, the scatter of the RC–SFR correlation could be stemming entirely from the calibration uncertainty of the hybrid SF tracer. However, the sub-linear slopes in our pixel-by-pixel plot mean that the local RC–SFR correlation is not linear. Using just one local measurement of the RC emission will hence not provide an accurate estimate of the Σ_{SFR} . As we have discussed in Section 5.2, this is almost entirely due to cosmic-ray transport within the disk, whereas the influence of IC radiation can be neglected. A high- z study of star-forming galaxies may reveal, if spatial resolution is high enough, only the peaks of the Σ_{SFR} within a galaxy, whereas

the fainter RC emission is missed. From our small sample of galaxies, it appears that if one restricts measurements to high radio and hybrid Σ_{SFR} , $(\Sigma_{\text{SFR}})_{\text{RC}} \gtrsim 10^{-2} M_{\odot} \text{ yr}^{-1} \text{ kpc}^{-2}$ and $(\Sigma_{\text{SFR}})_{\text{hyb}} \gtrsim 10^{-2} M_{\odot} \text{ yr}^{-1} \text{ kpc}^{-2}$, the spread around the Condon relation is much reduced, approximately to a factor of 2–3 (Figure 6). In case of only having radio measurements available, one can restrict to areas with “young” non-thermal spectral indices ($\alpha < -0.75$) in order to reduce the spread around the Condon relation. However, we have to caution that this is based only on the measurements of four galaxies (NGC 4736, NGC 5055, NGC 5194, and NGC 6946), which have such high Σ_{SFR} . Therefore, it is not clear, whether this is only a property of our galaxy sample or will indeed hold true for a much larger galaxy sample.

6. CONCLUSIONS

We have studied the resolved RC–SFR relation in a selection drawn from the THINGS sample of galaxies. We have used WSRT maps at $\lambda\lambda$ 22 and 18 cm as RC maps and a combination of *GALEX* FUV and *Spitzer* 24 μm maps as hybrid SF tracers. To estimate the fraction of thermal RC emission, we used maps of Balmer $H\alpha$ emission. We have compared our results with the well-established Condon relation. These are our main conclusions:

1. The integrated RC luminosity is almost directly proportional to the integrated hybrid SFR as expected from the Condon relation. We find $\text{SFR}_{\text{RC}} \propto \text{SFR}_{\text{hyb}}^{1.11 \pm 0.08}$, an only very moderately super-linear relation. The averaged ratio of integrated radio to hybrid SFR is $\langle \mathcal{R}_{\text{int}} \rangle = 0.8 \pm 0.4$, where the error reflects the standard deviation in our sample. The Condon relation hence predicts also the numerical value of the SFR correctly, within the uncertainty of our measurements. Because the integrated hybrid SFR has an intrinsic uncertainty of $\pm 50\%$, we conclude that the radio SFR has a similar accuracy if used for integrated measurements.
2. We have averaged the RC emission and hybrid SF tracers azimuthally in radial annuli to determine the radial profiles of both Σ_{SFR} . The ratio \mathcal{R} of radio to hybrid Σ_{SFR} stays remarkably constant as a function of galactocentric radius and undergoes only quasi-periodic variations. The relative variation of \mathcal{R} as a function of galactocentric radius is only 25%. We fitted a constant function to the profile of the ratio to measure the radial average $\langle \mathcal{R} \rangle$ within a galaxy. We find that $\langle \mathcal{R} \rangle$ agrees within the uncertainty with the integrated ratio \mathcal{R}_{int} . Again, we can conclude that the radio SFR has a similar accuracy as the hybrid SFR if used on azimuthally averaged data, i.e., radial profiles.
3. We have locally averaged the RC emission and hybrid SF tracers in pixels of 1.2 and 0.7 kpc resolution. We find a clear correlation between the Σ_{SFR} as derived from the RC emission and hybrid SF tracers. Averaged over our sample, the result is $(\Sigma_{\text{SFR}})_{\text{RC}} \propto (\Sigma_{\text{SFR}})_{\text{hyb}}^{0.63 \pm 0.25}$, where the uncertainty is the standard deviation of the sample galaxies. Results for the two resolutions are almost identical compared to the variation across our sample. The spread around the least-squares fit is a factor of 2–3, comparable with the uncertainty of the local hybrid Σ_{SFR} . However, because the relation of radio to

hybrid Σ_{SFR} is sub-linear, one cannot derive the local Σ_{SFR} from the radio emission alone.

4. Diffusion of CRE is responsible for flattening the local RC–SFR relation, resulting in a sub-linear relation. This is supported by our finding that at low radio and hybrid Σ_{SFR} , the non-thermal spectral index is predominantly steeper than -1.2 , indicative of an aged CRE population. At high Σ_{SFR} , the non-thermal radio spectral index is flatter than -0.75 , as expected from young CRE. At low Σ_{SFR} we hence have an excess of CRE, resulting in an excess of RC emission, which is dominated by non-thermal synchrotron emission around $\lambda 20$ cm.
5. We have compared the ratio \mathcal{R}_{int} of integrated radio to hybrid SFR with various fundamental galaxy parameters. We did not find any obvious dependence on any parameter we have tested for. The same result was found for the slope in the pixel-by-pixel plots. We find no indication of the escape of cosmic rays in a galactic wind as traced by the radio spectral index or influence of IC radiation dependent on the ratio of radiation to magnetic field energy density $U_{\text{rad}}/U_{\text{B}}$.
6. We have shown the importance of FUV as an SF tracer. In the outer parts of galaxies, where the amount of dust is low, *Spitzer* 24 μm emission alone is not a reliable SF tracer as it is not sensitive to the unobscured SF as measured by *GALEX* FUV emission. Thus, the ratio \mathcal{R} is constant when using the hybrid SF tracer from a combination of FUV and 24 μm , but rises significantly at larger radii when using 24 μm emission alone.
7. When restricting to the highest Σ_{SFR} , both $(\Sigma_{\text{SFR}})_{\text{RC}} \gtrsim 10^{-2} M_{\odot} \text{ yr}^{-1} \text{ kpc}^{-2}$ and $(\Sigma_{\text{SFR}})_{\text{hyb}} \gtrsim 10^{-2} M_{\odot} \text{ yr}^{-1} \text{ kpc}^{-2}$, the spread around the Condon relation reduces to a factor of 3, similar to the local uncertainty of the hybrid tracers, allowing the sole use of RC emission as an SF tracer. However, this result is based only on a sub-set of four galaxies that fulfill the above requirement. It hence has to be taken with caution.
8. We can explain the almost linear RC–SFR relation and the sub-linear resolved (on a 1 kpc scale) RC– Σ_{SFR} relation by proposing a non-linear magnetic field–SFR relation, which holds both globally and locally (1 kpc scale). Assuming energy equipartition between the cosmic rays and the magnetic field, we find $B \propto \text{SFR}_{\text{hyb}}^{0.30 \pm 0.02}$. Magnetic field amplification by a small-scale dynamo, powered by SF-driven turbulence, can explain our result.

V.H. is funded as a Postdoctoral Research Assistant by the UK’s Science and Technology Facilities Council (STFC). This research has made use of the NASA/IPAC Extragalactic Database (NED), which is operated by the Jet Propulsion Laboratory, California Institute of Technology, under contract with the National Aeronautics and Space Administration. The authors thank the anonymous referee for a detailed reading of the manuscript and for comments that have led to improvements in its clarity and presentation. Elly Berkhuijsen is thanked for carefully reading the almost finished manuscript and providing further comments and suggestions.

APPENDIX

FURTHER PARAMETER STUDIES

As we have seen in Section 4.1 the RC luminosity is a good tracer for the SF as measured from hybrid tracers. We have shown that the ratio \mathcal{R}_{int} of the integrated SFRs as measured from the RC to that from the hybrid SF tracers has an average close to one, as expected for the Condon relation, and a standard deviation of 0.4. It would be very important to know whether this ratio can be related to any global parameter of the galaxies in our sample. If we cannot find such a parameter, then the ratio would be a *universal* number and can be assumed to be equal for all galaxies, albeit with some uncertainty. Tables 1 and 2 contain the literature and measured data we plot the ratio \mathcal{R}_{int} against.

We now compare the ratio \mathcal{R}_{int} with various galaxy parameters and look for possible trends. We applied a standard least-squares fit with error weighting of \mathcal{R}_{int} as a function of all parameters and show them for those, where hints of a correlation with \mathcal{R}_{int} can be seen. The results are shown in Figures 11–13. We will discuss them in the following. We note that we have discussed the correlation between the ratio \mathcal{R}_{int} and both the radiation energy density and non-thermal radio spectral index already in Section 5.1.

SFR. As we have discussed in Section 4.1 the ratio \mathcal{R}_{int} of integrated radio to hybrid SFRs is rising slightly with increasing SFRs. This can be seen by the fact that the power-law index in Equation (5), ζ , is larger than one. In Figure 11(a) we plot the ratio \mathcal{R}_{int} as a function of the SFR as derived from the RC luminosity. There is no clear correlation with a significant spread in the data points. But the ratio appears to be indeed rising with increasing radio SFR as expected. We also have tested the relation with the hybrid SFR (Figure 11(c)), where the correlation is, if anything, weaker than for the radio SFR. This is of course expected, because the radio SFR is in the numerator of the ratio $\mathcal{R}_{\text{int}} = \text{SFR}_{\text{RC}}/\text{SFR}_{\text{hyb}}$, whereas the hybrid SFR is in the denominator.

SFR density. We have made the same plots for the SFR averaged over the physical area of the galaxies. For this we chose the galactocentric radius that we used for the integrations with IRING as described in Section 3.3. The plots are presented in Figures 11(b) and (d). The data points show again a large scatter, but the ratio rises with higher Σ_{SFR} , particularly for the radio Σ_{SFR} . For the hybrid Σ_{SFR} the correlation is less pronounced than for the radio Σ_{SFR} , as it is for the integrated SFRs.

Molecular hydrogen mass. In galaxies, there is a well-pronounced correlation between the mass of the molecular hydrogen and the integrated SFR, known as the “molecular Schmidt law” (Bigiel et al. 2008; Kennicutt et al. 2007). For higher masses of molecular hydrogen we have higher SFRs and thus as shown before higher ratios \mathcal{R}_{int} . Therefore, we expect the ratio \mathcal{R}_{int} rising not only with the SFR but also with the mass of the molecular hydrogen. We plot the correlation in Figures 11(e) and (f) for the integrated molecular hydrogen mass and mass surface density. We indeed find some weak correlation, where the ratio \mathcal{R}_{int} rises with both the molecular hydrogen mass and mass surface density.

Atomic hydrogen mass. We have compared the ratio \mathcal{R}_{int} with the atomic hydrogen mass, but found no obvious correlation either for the mass or for the mass surface density as shown in Figures 12(a) and (b).

Total hydrogen mass. The ratio \mathcal{R}_{int} is shown also as a function of the total hydrogen mass in Figures 12(c) and (d), the sum of atomic and molecular hydrogen. No correlation is found for either the mass or the mass surface density.

Inclination angle. We found a dependence of the ratio \mathcal{R}_{int} on the inclination angle of the galaxy as shown in Figure 12(e). With increasing inclination angle, i.e., the galaxy is seen closer to an edge-on position, the ratio \mathcal{R}_{int} drops. This dependence is not easily understood. We adjusted the size of the ellipses of integration to include any RC halo emission (Section 3.3), so deficiency in RC emission can be excluded. It could be that we overestimate the hybrid Σ_{SFR} , because in an edge-on position the diffuse “cirrus” emission at 24 μm may add up to levels such that it exceeds the detection threshold due to longer lines of sight.

Galaxy type. We tested whether the ratio \mathcal{R}_{int} depends on the type of galaxy, e.g. whether it is an early or late type galaxy. This plot is shown in Figure 12f with no correlation visible.

B-band magnitude. The B-band magnitude is a coarse tracer for SF showing mainly the young, blue population of massive stars. We find again a slight dependence of higher ratios \mathcal{R}_{int} toward higher SFRs as traced by the B-band as shown in Figure 13(a).

Thermal RC fraction. We compare the ratio \mathcal{R}_{int} with the thermal fraction of the RC emission as measured from H α emission in Figure 13(b). We do not find any clear correlation. The two galaxies with the largest thermal fraction, NGC 2403 and IC 2574, have low ratios with $\mathcal{R}_{\text{int}} \approx 0.35$.

Fractional polarization. We used the values of Heald et al. (2009), who measured the fractional polarization of the WSRT SINGS galaxies at λ 22 cm. No correlation with the ratio \mathcal{R}_{int} was found as shown in Figure 13(c). The fractional polarization is a measure of how ordered the magnetic field orientation is within a resolution element. However, one has to caution that at this long wavelength of λ 22 cm the polarized emission mostly comes from the near side of the halo, because of Faraday depolarization by the disk magnetic field (Braun et al. 2010).

Metallicity. Metallicity values of Walter et al. (2008) were used to study the dependence of the ratio \mathcal{R}_{int} on metallicity. Our sample galaxies do not show any obvious correlation (Figure 13(d)).

Redshift. The galaxies in our sample are all nearby within 25 Mpc and thus have only small redshifts. The ratio \mathcal{R}_{int} as a function of redshift is shown in Figure 13(e). No obvious correlation is visible.

Stellar mass. Figure 13(f) shows the plot of the ratio as a function of stellar mass. A weak correlation appears that larger ratios \mathcal{R}_{int} are found at higher stellar masses.

We have also tested the above correlation with the slope of the pixel-by-pixel plots as measured in Section 4.3. These plots are shown in Figures 11–13, overlaid as open circles. We found no obvious correlation for any of the parameters. In conclusion to this section we find that the ratio \mathcal{R}_{int} appears to be indeed a universal parameter, as we do not find any obvious correlation with any galaxy parameter. There appears to be a weak correlation of a rising ratio \mathcal{R}_{int} with SFR, Σ_{SFR} , or SF tracer. But the scatter is substantial and we cannot be confident at this stage if any relation would become evident when dealing with a larger sample. We particularly note that we do not find any dependence of the integrated ratio \mathcal{R}_{int} on either the ratio of radiation energy density to magnetic field energy density or the non-thermal radio spectral index. This points to the fact that neither high IC radiation losses

nor CRE escape are responsible for radio dim galaxies, as we have discussed in Section 5.1.

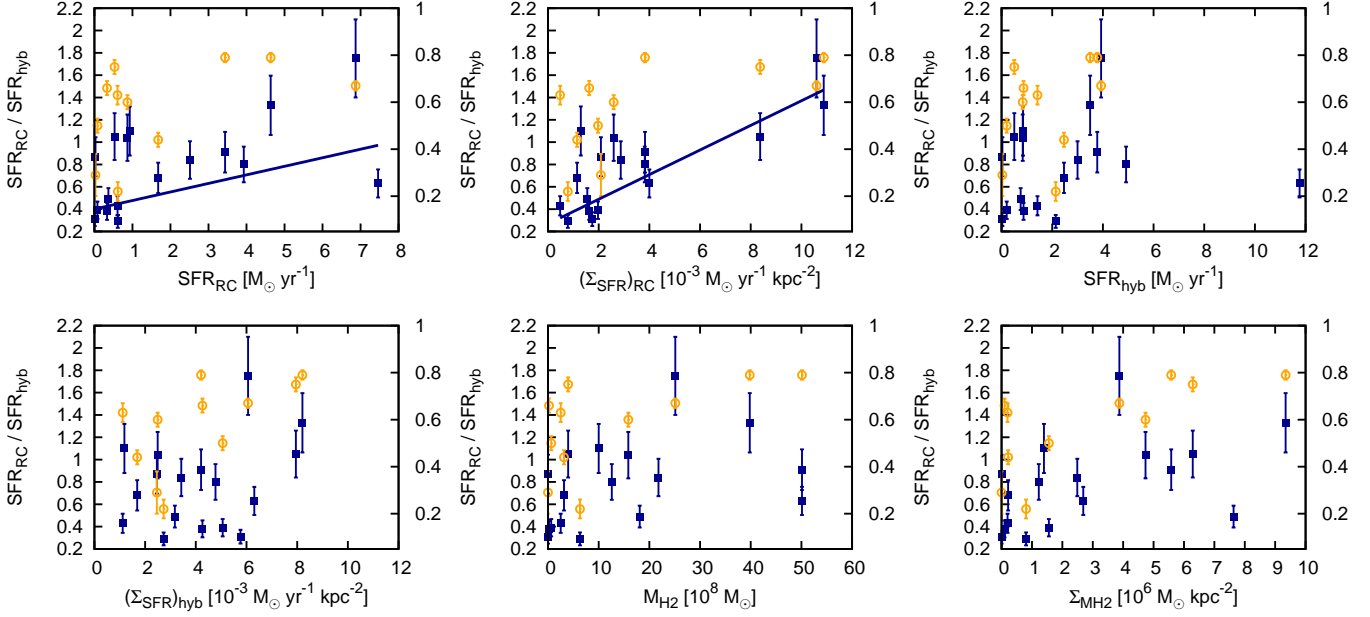


Figure 11. Parameter studies — I. We compare the ratio of the SFRs as derived by the RC emission and hybrid SF tracers as a function of various galaxy parameters (filled squares). Solid lines represent least-squares fits to the filled squares. We also plot the pixel-by-pixel slopes as measured at 1.2 kpc resolution (open circles), where the scale is on the right axis. (a) SFR from RC luminosity. (b) Σ_{SFR} as calculated from integrated radio SFR divided by physical area. (c) Integrated SFR from hybrid SF tracers. (d) Σ_{SFR} as calculated from integrated hybrid SF tracers divided by physical area. (e) Molecular hydrogen mass. (f) Molecular hydrogen mass surface density.

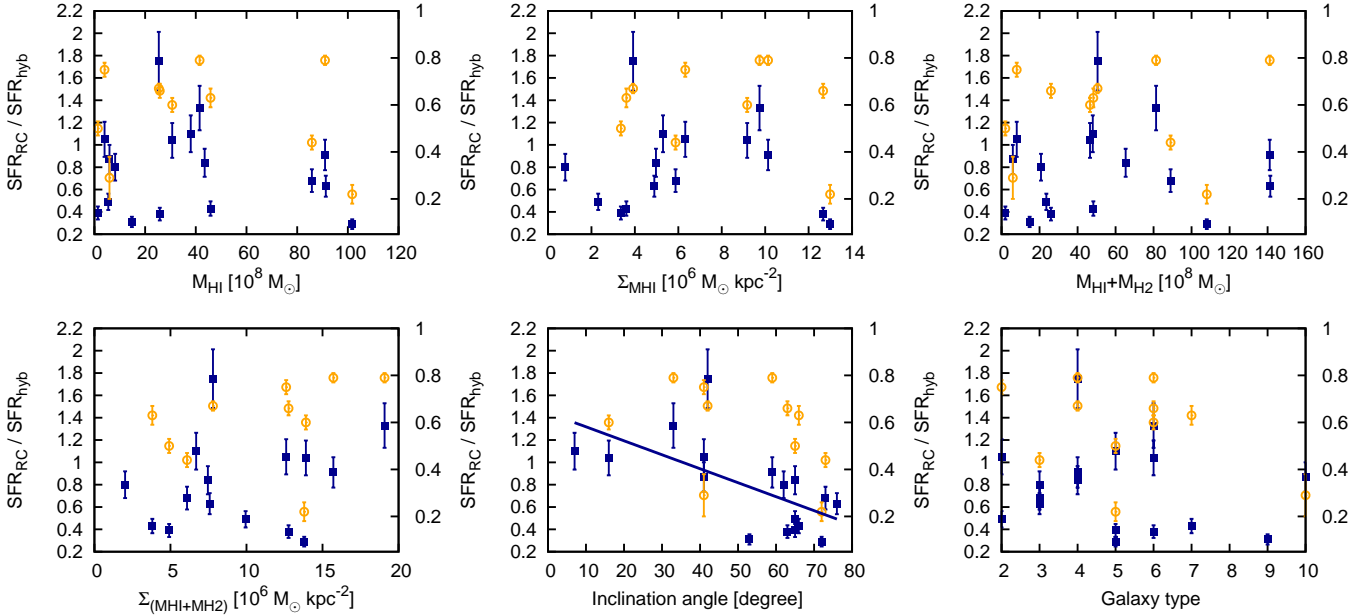


Figure 12. Parameter studies — II. We compare the ratio of the SFRs as derived by the RC emission and hybrid SF tracers as a function of various galaxy parameters (filled squares). Solid lines represent least-squares fits to the filled squares. We also plot the pixel-by-pixel slopes as measured at 1.2 kpc resolution (open circles), where the scale is on the right axis. (a) Atomic hydrogen mass. (b) Atomic hydrogen mass divided by physical area. (c) Total hydrogen mass. (d) Total hydrogen mass divided by physical area. (e) Inclination angle. (f) Galaxy type.

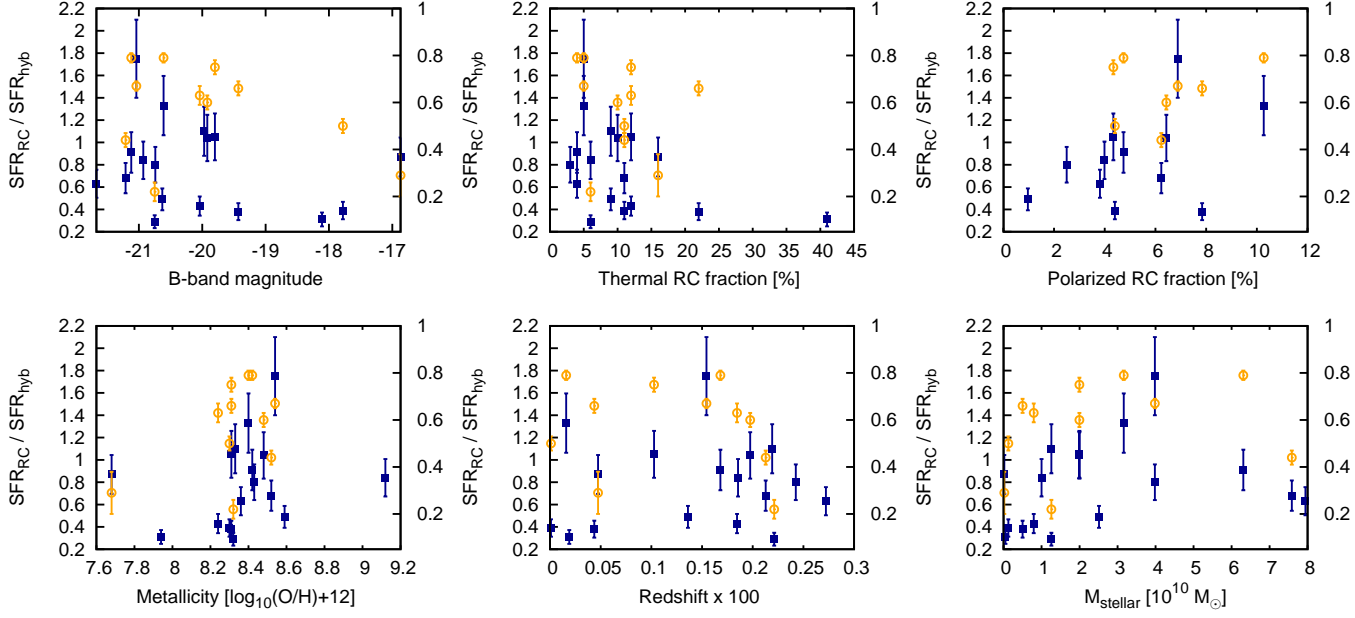


Figure 13. Parameter studies — III. We compare the ratio of the SFRs as derived by the RC emission and hybrid SF tracers as a function of various galaxy parameters (filled squares). We also plot the pixel-by-pixel slopes as measured at 1.2 kpc resolution (open circles), where the scale is on the right axis. (a) *B*-band magnitude. (b) Thermal RC fraction. (c) Linearly polarized RC fraction. (d) Metallicity. (e) Redshift. (f) Stellar mass.

ATLAS OF MAPS AND PROFILE PLOTS

In Figures 14–30, we present maps and radial profiles for individual galaxies. Each page shows results for one galaxy. The top row shows maps of RC emission at $\lambda 22$ cm, hybrid SFR density ($\Sigma_{\text{SFR}}_{\text{hyb}}$), and thermal RC emission at $\lambda 22$ cm. In the second row at the right, we show the thermal RC fraction at $\lambda 22$ cm. These maps use a gray-scale linear transfer function, where a bar at the top illustrates the gray tones used. The ellipse indicates the area we have used for integrating the RC emission and studying radial profiles. A bar in the middle panel of the top row indicates the spatial scale in each galaxy. The size of the FWHM, the angular resolution of our maps, is shown in the left bottom corner by the open circle. Please note that each galaxy has a different angular and spatial resolution.

In the second row at the left, we show profiles of the azimuthally averaged star formation rate surface density based on RC emission at $\lambda 22$ cm (dark blue), based on the hybrid prescription of *GALEX* FUV and *Spitzer* 24 μm (orange), based on *Spitzer* 24 μm only (green), and based on *GALEX* FUV only (violet). Open dark blue symbols show the SFR surface density based on the non-thermal RC emission at $\lambda 22$ cm only. The latter one is shown for comparison in order to highlight the different behavior of thermal and non-thermal RC emission. In the second row, the middle panel shows the profile of the ratio of RC to hybrid SFR surface density. Open symbols show this ratio for the non-thermal RC emission only. The solid line shows the constant ratio of a linear least-squares fit to the data and the dashed line shows the same for the non-thermal RC only.

The following plots are only shown if our maps of an individual galaxy has sufficient spatial resolution. In the left panel of the third row, we show the pixel-by-pixel plots at 1.2 kpc spatial resolution. The SFR surface density based on the RC emission at $\lambda 22$ cm is plotted as a function of the hybrid SFR surface density. The solid line shows a least-squares fit to the data and the dashed line shows the relation as predicted by Condon (1992). The color of the data points depends on the radio spectral index: spectral indices $\alpha < -0.75$ are color coded in red, spectral indices $-1.2 \leq \alpha \leq -0.75$ are color coded in green, and spectral indices $\alpha < -1.2$ are color coded in blue. The middle panel in the third row shows the pixel-by-pixel plots for the non-thermal RC emission only. The right panel in the third row shows the map of the radio spectral index between $\lambda\lambda$ 22 and 18 cm, where we have color coded the data as in the pixel-by-pixel plots (with the exception of Holmberg II and NGC 4736). The fourth row shows the same plots as the third row but for a spatial resolution of 0.7 kpc.

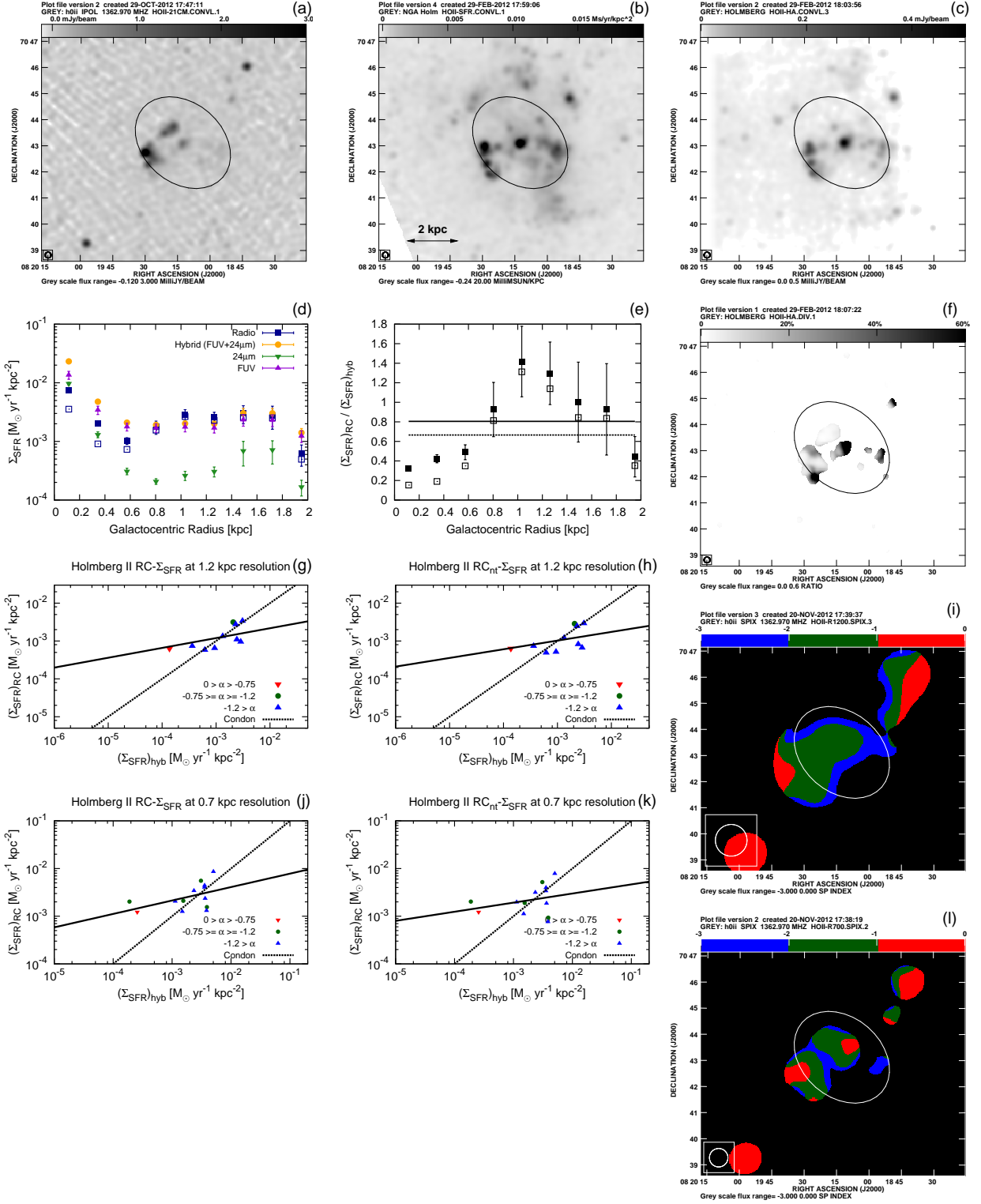


Figure 14. Holmberg II. (a) RC emission at $\lambda 22$ cm. (b) Hybrid SFR surface density ($\Sigma_{\text{SFR}}^{\text{hyb}}$). (c) Thermal RC emission as derived from $\text{H}\alpha$. (d) Radio Σ_{SFR} (dark blue) and hybrid Σ_{SFR} (orange) as a function of galactocentric radius. (e) Ratio \mathcal{R} of radio to hybrid Σ_{SFR} . Open symbols represent the non-thermal RC emission alone. (f) Predicted thermal RC fraction. (g) Radio Σ_{SFR} as a function of hybrid Σ_{SFR} at 1.2 kpc resolution. (h) Same as (g) but with thermal emission subtracted. (i) Radio spectral index at 1.2 kpc resolution. (j-l) Same as (g-i) but at 0.7 kpc resolution. The typical uncertainty of the radio spectral index is 0.6.

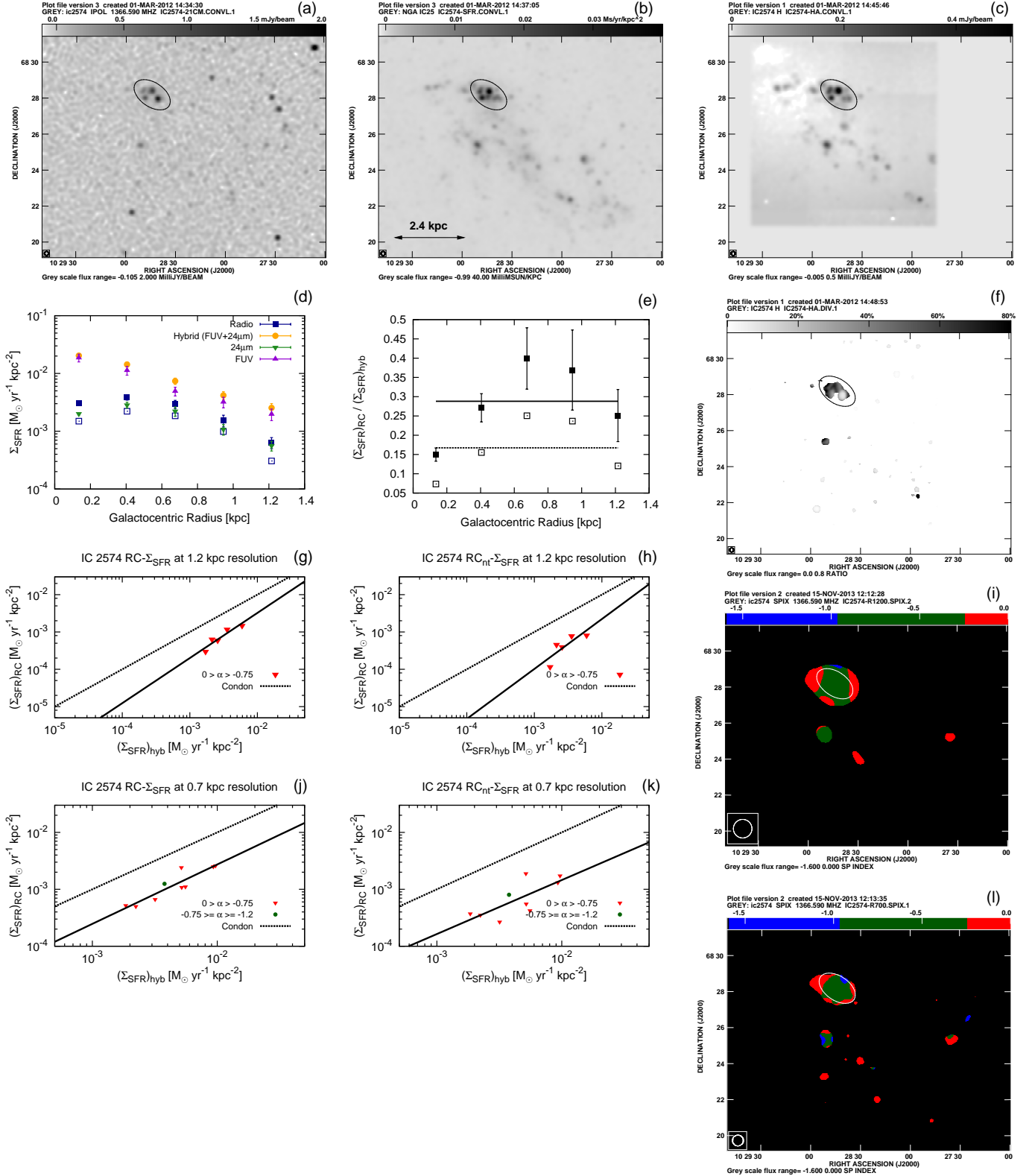


Figure 15. IC 2574. (a) RC emission at $\lambda 22$ cm. (b) Hybrid SFR surface density ($\Sigma_{\text{SFR}}_{\text{hyb}}$). (c) Thermal RC emission as derived from H α . (d) Radio Σ_{SFR} (dark blue) and hybrid Σ_{SFR} (orange) as a function of galactocentric radius. (e) Ratio \mathcal{R} of radio to hybrid Σ_{SFR} . Open symbols represent the non-thermal RC emission alone. (f) Predicted thermal RC fraction. (g) Radio Σ_{SFR} as a function of hybrid Σ_{SFR} at 1.2 kpc resolution. (h) Same as (g) but with thermal emission subtracted. (i) Radio spectral index at 1.2 kpc resolution. (j–l) Same as (g–i) but at 0.7 kpc resolution. The typical uncertainty of the radio spectral index is 0.6.

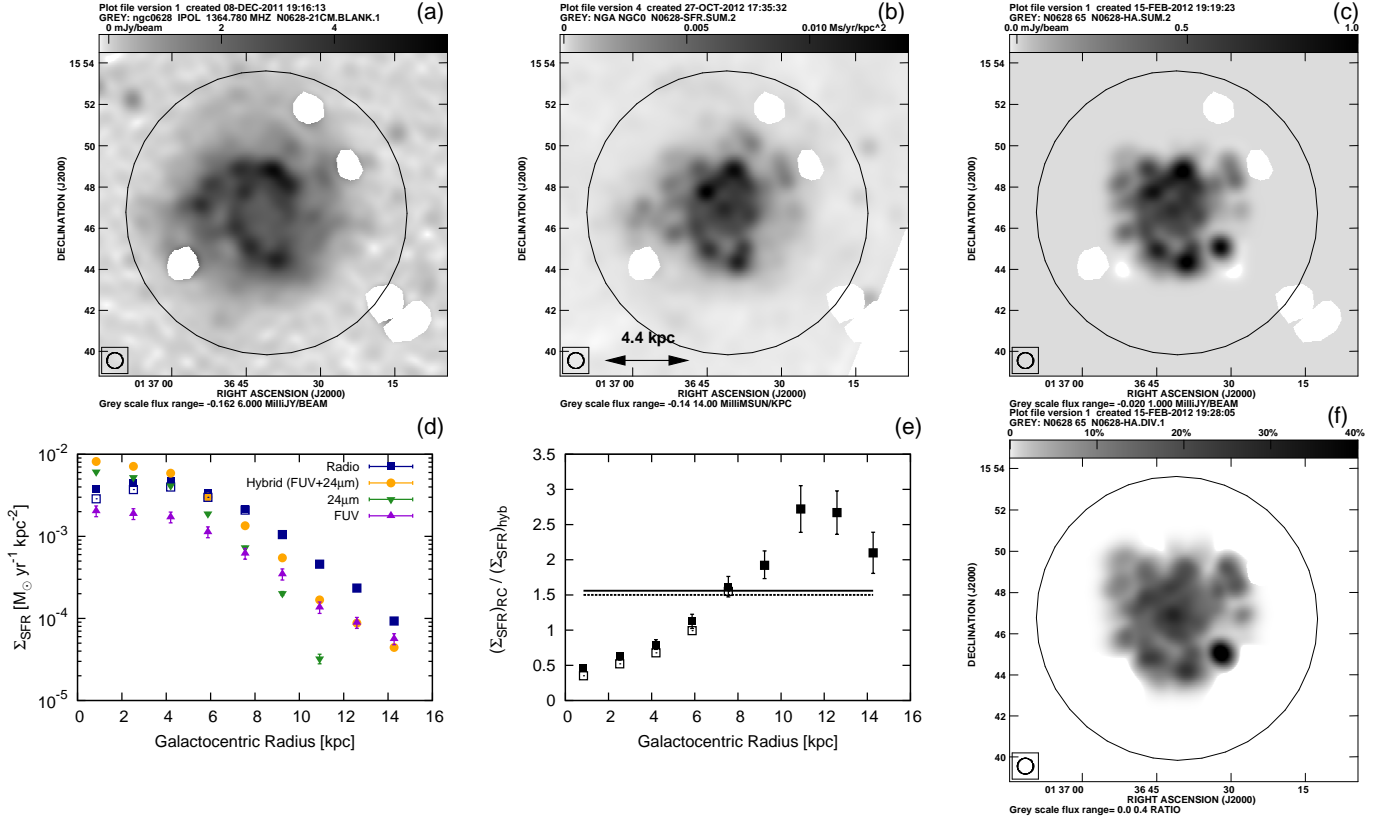


Figure 16. NGC 628. (a) RC emission at $\lambda 22$ cm. (b) Hybrid SFR surface density $(\Sigma_{\text{SFR}})_{\text{hyb}}$. (c) Thermal RC emission as derived from H α . (d) Radio Σ_{SFR} (dark blue) and hybrid Σ_{SFR} (orange) as a function of galactocentric radius. (e) Ratio \mathcal{R} of radio to hybrid Σ_{SFR} . Open symbols represent the non-thermal RC emission alone. (f) Predicted thermal RC fraction.

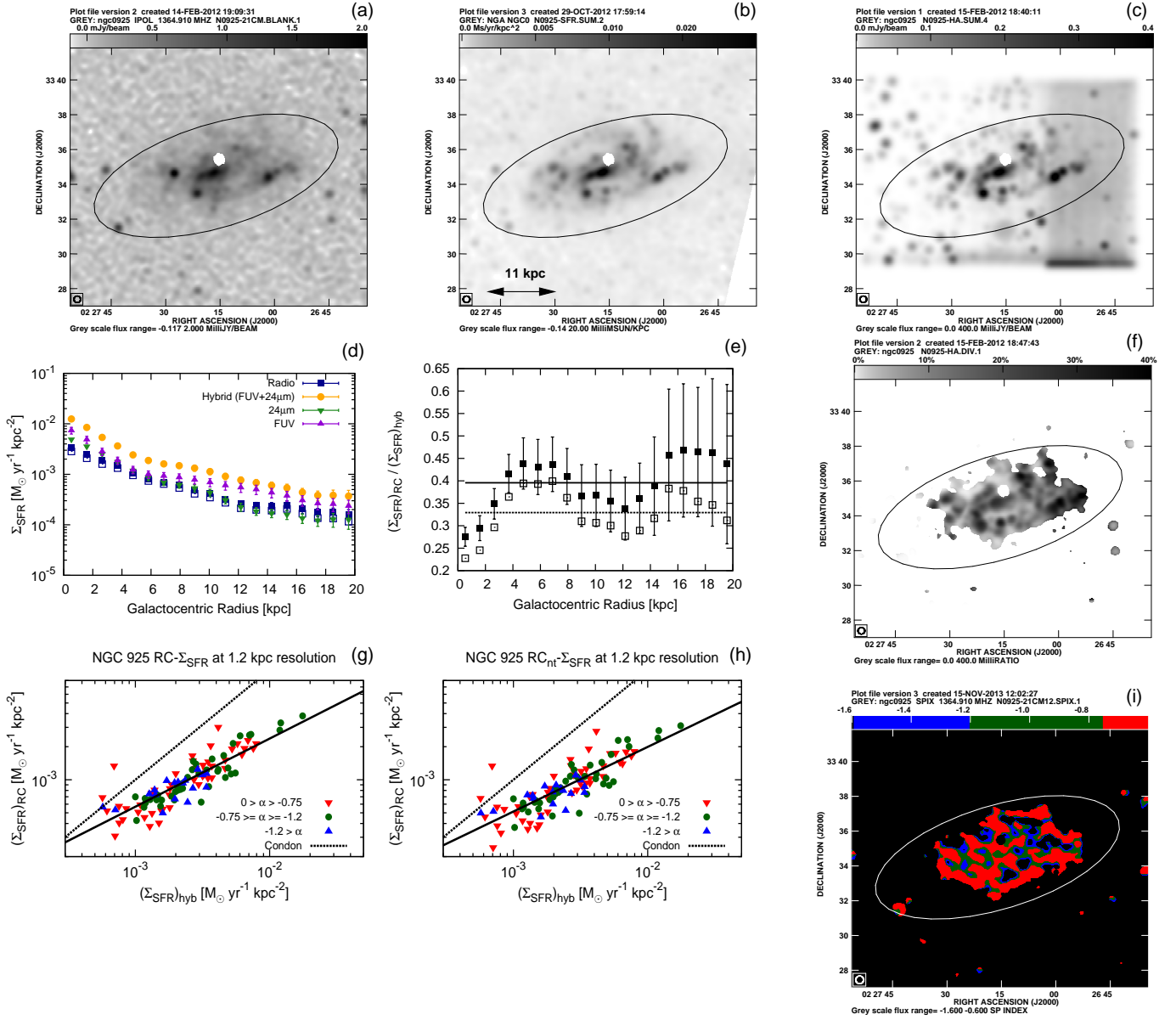


Figure 17. NGC 925. (a) RC emission at $\lambda 22$ cm. (b) Hybrid SFR surface density $(\Sigma_{\text{SFR}})_{\text{hyb}}$. (c) Thermal RC emission as derived from $\text{H}\alpha$. (d) Radio Σ_{SFR} (dark blue) and hybrid Σ_{SFR} (orange) as a function of galactocentric radius. (e) Ratio \mathcal{R} of radio to hybrid Σ_{SFR} . Open symbols represent the non-thermal RC emission alone. (f) Predicted thermal RC fraction. (g) Radio Σ_{SFR} as a function of hybrid Σ_{SFR} at 1.2 kpc resolution. (h) Same as (g) but with thermal emission subtracted. (i) Radio spectral index at 1.2 kpc resolution. The typical uncertainty of the radio spectral index is 1.5 and 0.6 for radio Σ_{SFR} of 10^{-3} and $3 \times 10^{-3} M_{\odot} \text{ yr}^{-1} \text{ kpc}^{-2}$, respectively.

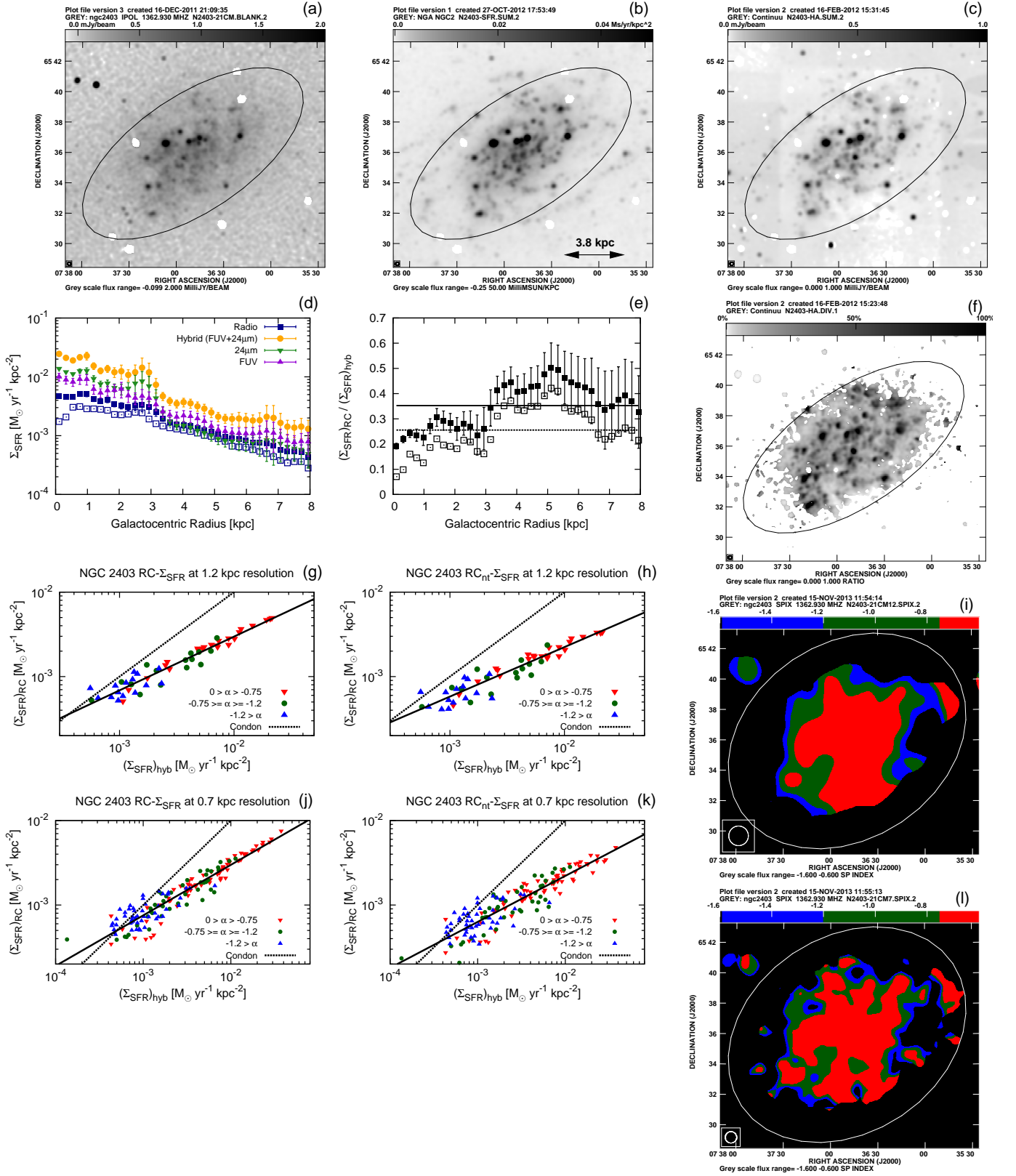


Figure 18. NGC 2403. (a) RC emission at $\lambda 22$ cm. (b) Hybrid SFR surface density ($\Sigma_{\text{SFR}}_{\text{hyb}}$). (c) Thermal RC emission as derived from H α . (d) Radio Σ_{SFR} (dark blue) and hybrid Σ_{SFR} (orange) as a function of galactocentric radius. (e) Ratio \mathcal{R} of radio to hybrid Σ_{SFR} . Open symbols represent the non-thermal RC emission alone. (f) Predicted thermal RC fraction. (g) Radio Σ_{SFR} as a function of hybrid Σ_{SFR} at 1.2 kpc resolution. (h) Same as (g) but with thermal emission subtracted. (i) Radio spectral index at 1.2 kpc resolution. (j–l) Same as (g–i) but at 0.7 kpc resolution. The typical uncertainty of the radio spectral index is 1.2, 0.6, and 0.3 for the blue, green, and red data points, respectively.

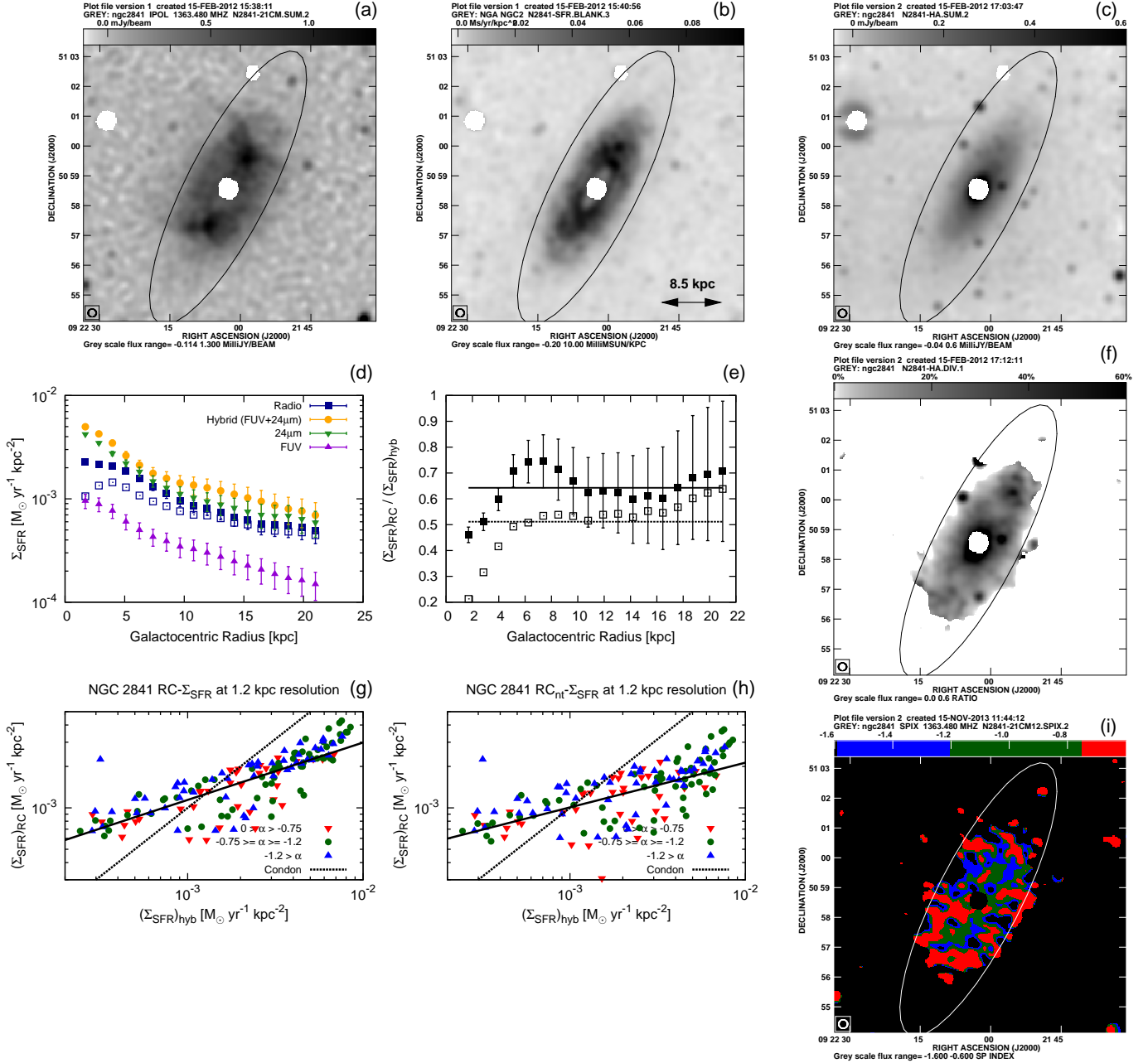


Figure 19. NGC 2841. (a) RC emission at $\lambda 22$ cm. (b) Hybrid SFR surface density $(\Sigma_{\text{SFR}})_{\text{hyb}}$. (c) Thermal RC emission as derived from H α . (d) Radio Σ_{SFR} (dark blue) and hybrid Σ_{SFR} (orange) as a function of galactocentric radius. (e) Ratio \mathcal{R} of radio to hybrid Σ_{SFR} . Open symbols represent the non-thermal RC emission alone. (f) Predicted thermal RC fraction. (g) Radio Σ_{SFR} as a function of hybrid Σ_{SFR} at 1.2 kpc resolution. (h) Same as (g) but with thermal emission subtracted. (i) Radio spectral index at 1.2 kpc resolution. The typical uncertainty of the radio spectral index is 1.2 and 0.6 for radio Σ_{SFR} of 2×10^{-3} and $4 \times 10^{-3} M_{\odot} \text{ yr}^{-1} \text{ kpc}^{-2}$, respectively.

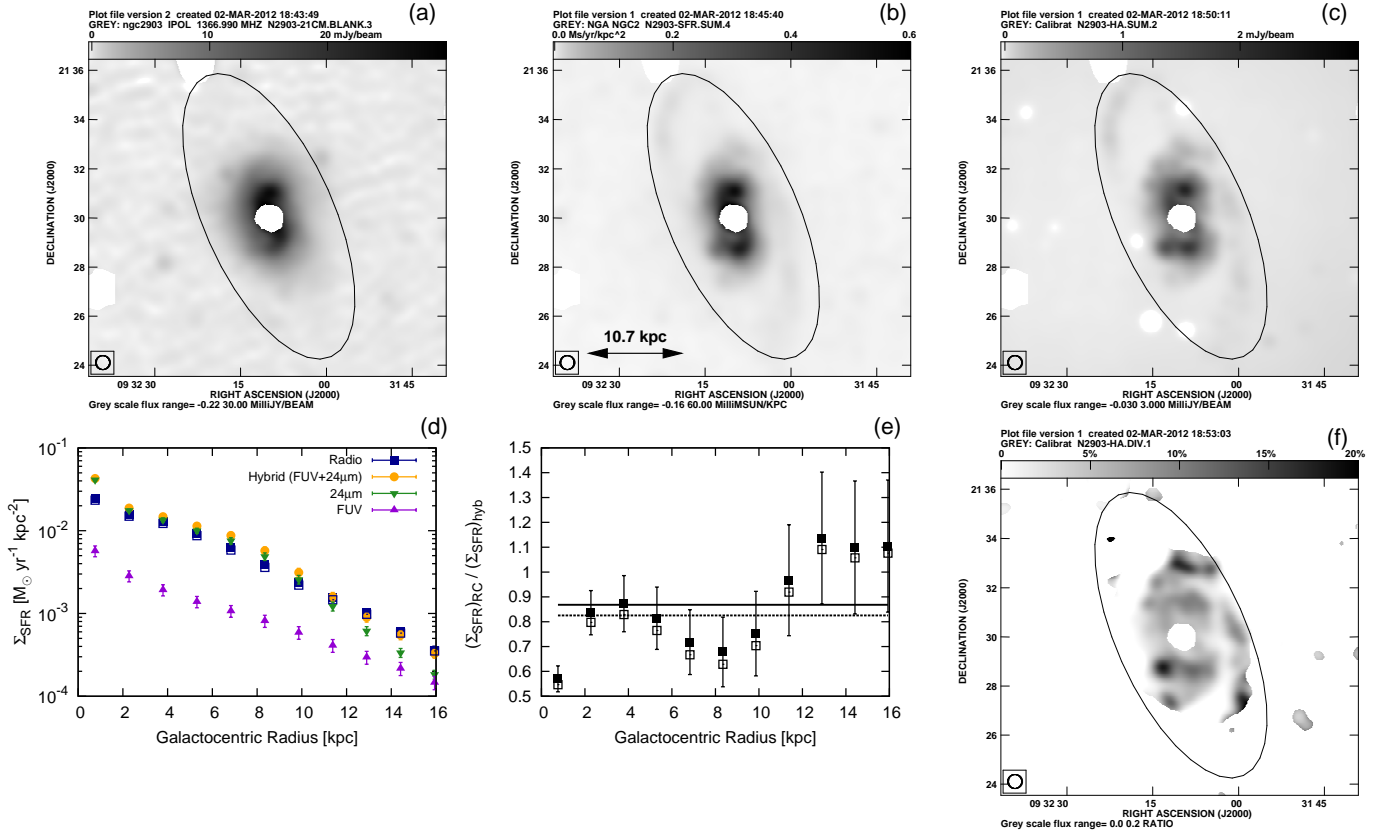


Figure 20. NGC 2903. (a) RC emission at $\lambda 22$ cm. (b) Hybrid SFR surface density ($\Sigma_{\text{SFR}}_{\text{hyb}}$). (c) Thermal RC emission as derived from H α . (d) Radio Σ_{SFR} (dark blue) and hybrid Σ_{SFR} (orange) as a function of galactocentric radius. (e) Ratio \mathcal{R} of radio to hybrid Σ_{SFR} . Open symbols represent the non-thermal RC emission alone. (f) Predicted thermal RC fraction.

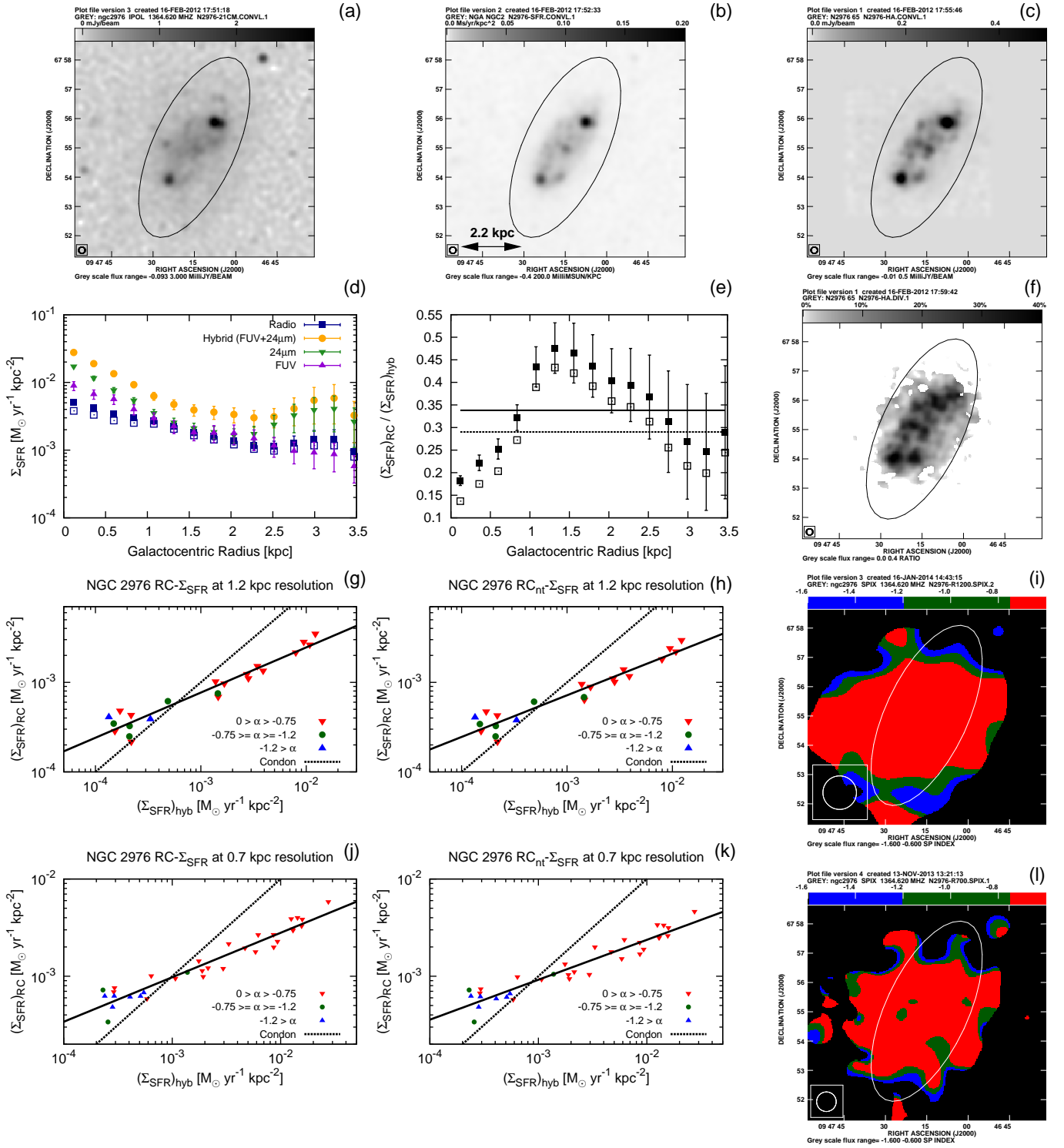


Figure 21. NGC 2976. (a) RC emission at $\lambda 22$ cm. (b) Hybrid SFR surface density ($\Sigma_{\text{SFR}}_{\text{hyb}}$). (c) Thermal RC emission as derived from H α . (d) Radio Σ_{SFR} (dark blue) and hybrid Σ_{SFR} (orange) as a function of galactocentric radius. (e) Ratio \mathcal{R} of radio to hybrid Σ_{SFR} . Open symbols represent the non-thermal RC emission alone. (f) Predicted thermal RC fraction. (g) Radio Σ_{SFR} as a function of hybrid Σ_{SFR} at 1.2 kpc resolution. (h) Same as (g) but with thermal emission subtracted. (i) Radio spectral index at 1.2 kpc resolution. (j–l) Same as (g–i) but at 0.7 kpc resolution. The typical uncertainty of the radio spectral index is 0.8 and 0.3 for radio Σ_{SFR} of 7×10^{-4} and $2 \times 10^{-3} M_{\odot} \text{ yr}^{-1} \text{ kpc}^{-2}$, respectively.

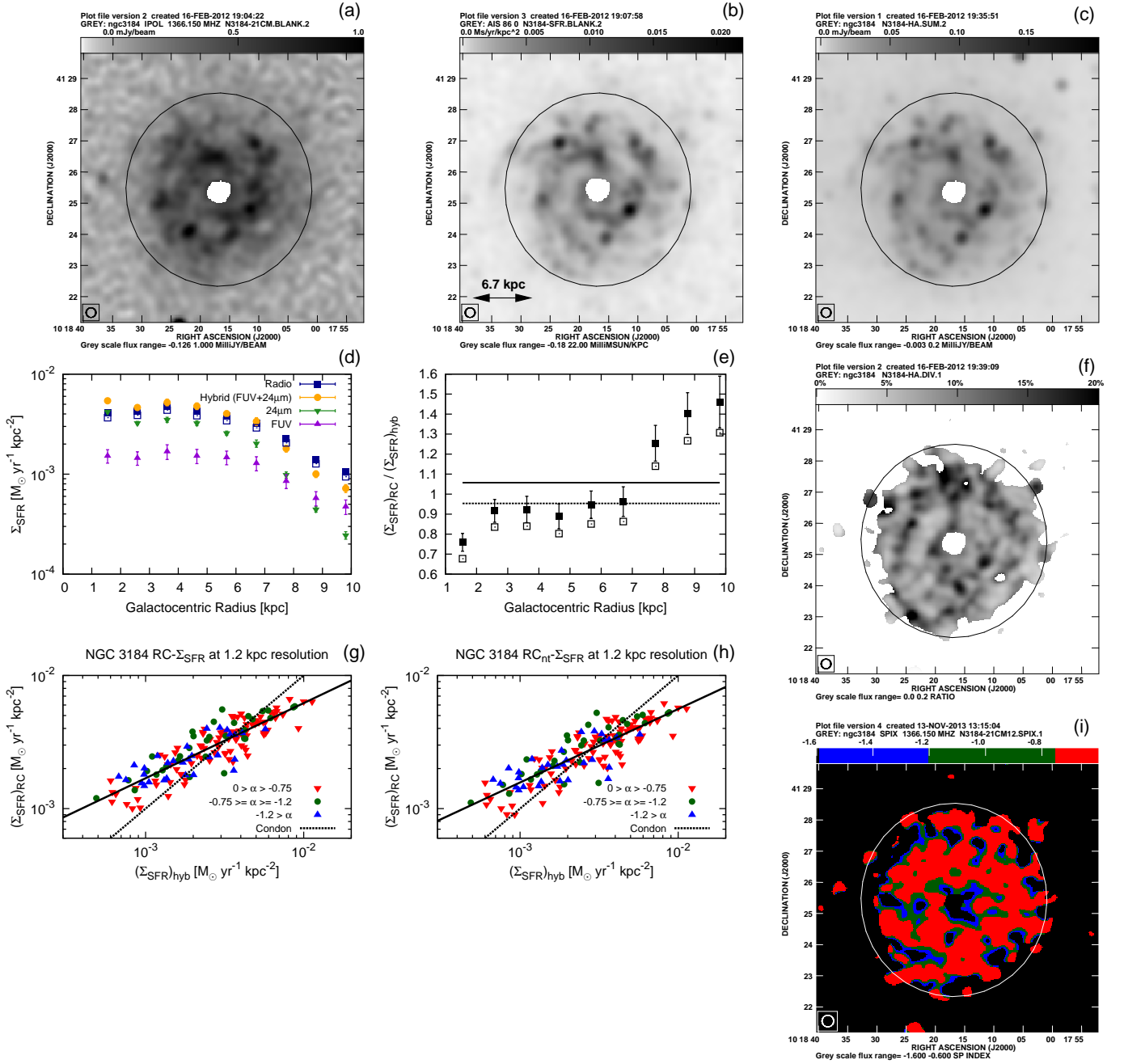


Figure 22. NGC 3184. (a) RC emission at $\lambda 22$ cm. (b) Hybrid SFR surface density ($\Sigma_{\text{SFR}}_{\text{hyb}}$). (c) Thermal RC emission as derived from H α . (d) Radio Σ_{SFR} (dark blue) and hybrid Σ_{SFR} (orange) as a function of galactocentric radius. (e) Ratio \mathcal{R} of radio to hybrid Σ_{SFR} . Open symbols represent the non-thermal RC emission alone. (f) Predicted thermal RC fraction. (g) Radio Σ_{SFR} as a function of hybrid Σ_{SFR} at 1.2 kpc resolution. (h) Same as (g) but with thermal emission subtracted. (i) Radio spectral index at 1.2 kpc resolution. The typical uncertainty of the radio spectral index is 1.2 and 0.5 for radio Σ_{SFR} of 3×10^{-3} and $8 \times 10^{-3} M_{\odot} \text{ yr}^{-1} \text{ kpc}^{-2}$, respectively.

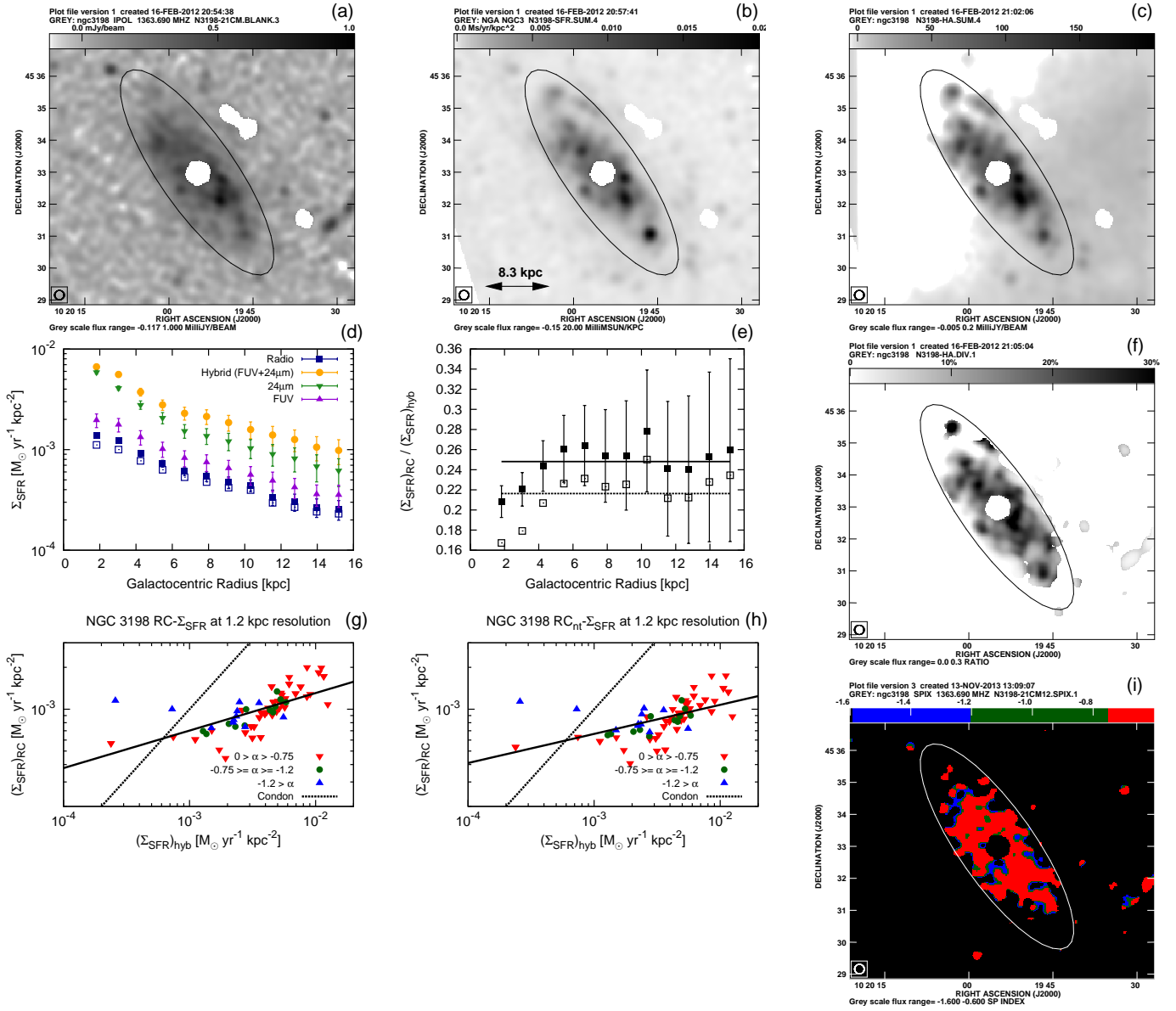


Figure 23. NGC 3198. (a) RC emission at 122 cm. (b) Hybrid SFR surface density $(\Sigma_{\text{SFR}})_{\text{hyb}}$. (c) Thermal RC emission as derived from H α . (d) Radio Σ_{SFR} (dark blue) and hybrid Σ_{SFR} (orange) as a function of galactocentric radius. (e) Ratio \mathcal{R} of radio to hybrid Σ_{SFR} . Open symbols represent the non-thermal RC emission alone. (f) Predicted thermal RC fraction. (g) Radio Σ_{SFR} as a function of hybrid Σ_{SFR} at 1.2 kpc resolution. (h) Same as (g) but with thermal emission subtracted. (i) Radio spectral index at 1.2 kpc resolution. The typical uncertainty of the radio spectral index is 1.2 for radio Σ_{SFR} of $1 \times 10^{-3} M_{\odot} \text{ yr}^{-1} \text{ kpc}^{-2}$.

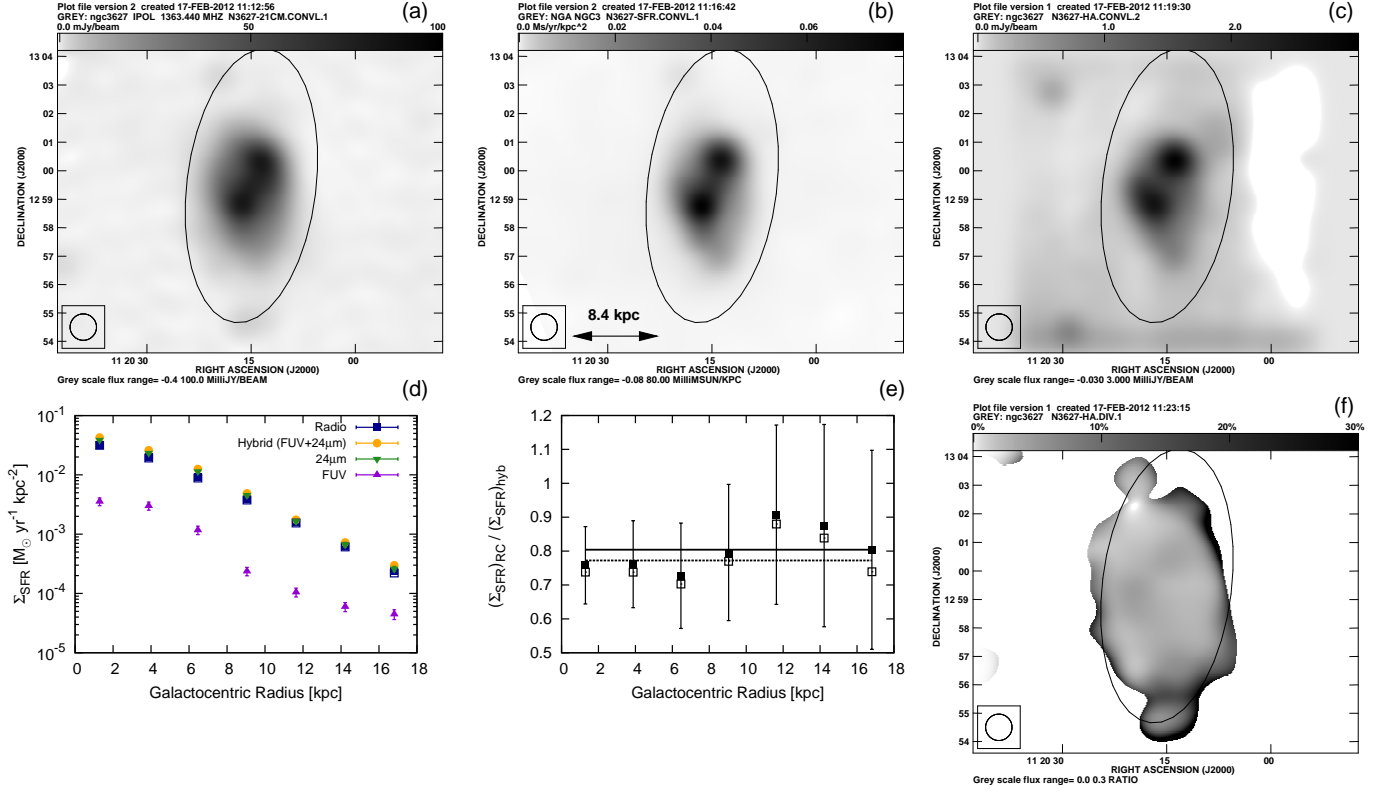


Figure 24. NGC 3627. (a) RC emission at $\lambda 22$ cm. (b) Hybrid SFR surface density $(\Sigma_{\text{SFR}})_{\text{hyb}}$. (c) Thermal RC emission as derived from H α . (d) Radio Σ_{SFR} (dark blue) and hybrid Σ_{SFR} (orange) as a function of galactocentric radius. (e) Ratio \mathcal{R} of radio to hybrid Σ_{SFR} . Open symbols represent the non-thermal RC emission alone. (f) Predicted thermal RC fraction.

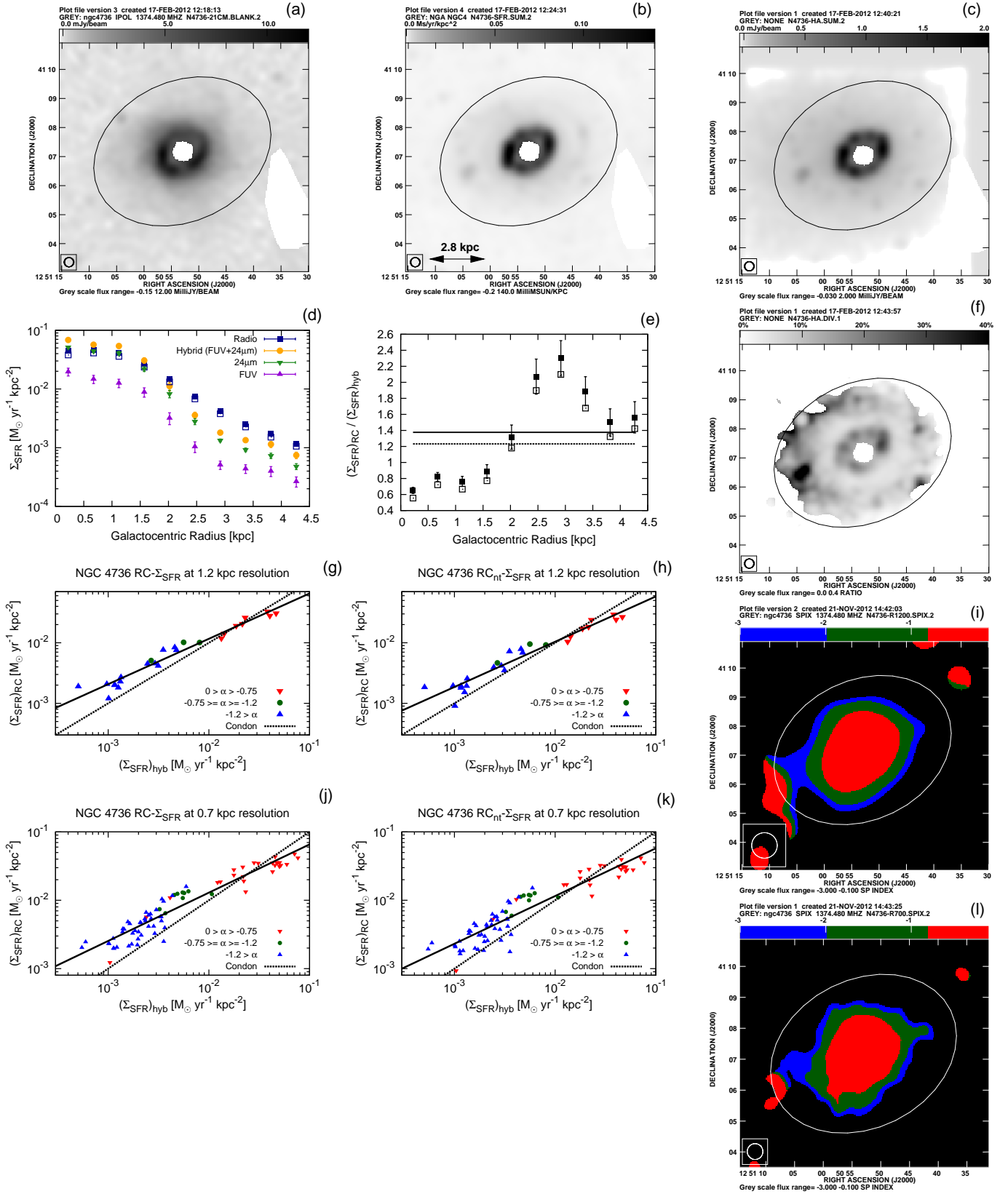


Figure 25. NGC 4736. (a) RC emission at $\lambda 22$ cm. (b) Hybrid SFR surface density $(\Sigma_{\text{SFR}})_{\text{hyb}}$. (c) Thermal RC emission as derived from H α . (d) Radio Σ_{SFR} (dark blue) and hybrid Σ_{SFR} (orange) as a function of galactocentric radius. (e) Ratio \mathcal{R} of radio to hybrid Σ_{SFR} . Open symbols represent the non-thermal RC emission alone. (f) Predicted thermal RC fraction. (g) Radio Σ_{SFR} as a function of hybrid Σ_{SFR} at 1.2 kpc resolution. (h) Same as (g) but with thermal emission subtracted. (i) Radio spectral index at 1.2 kpc resolution. (j–l) as (g–i) but at 0.7 kpc resolution. The typical uncertainty of the radio spectral index is 0.5, 0.1, and 0.05 for the blue, green, and red data points, respectively.

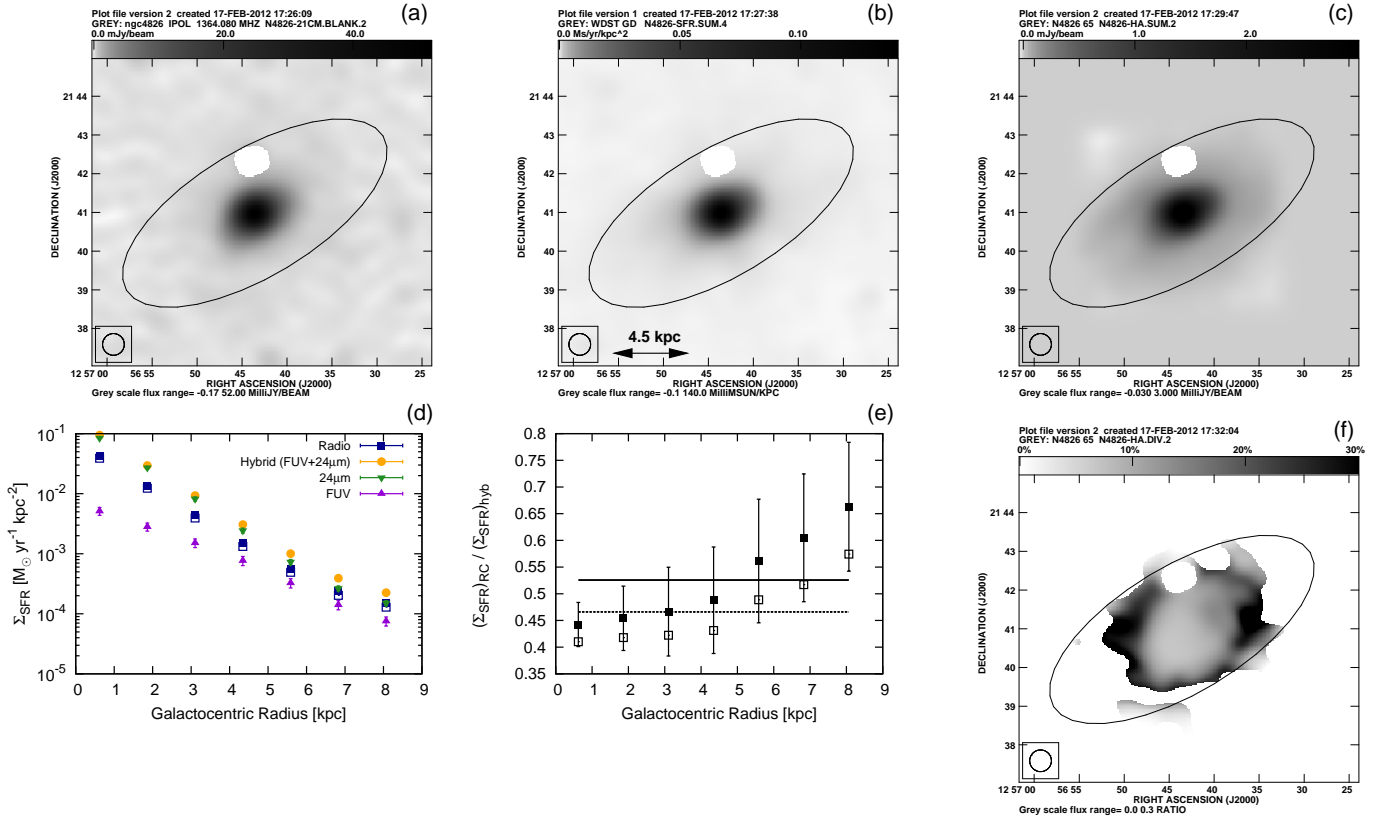


Figure 26. NGC 4826. (a) RC emission at 122 cm. (b) Hybrid SFR surface density $(\Sigma_{\text{SFR}})_{\text{hyb}}$. (c) Thermal RC emission as derived from H α . (d) Radio Σ_{SFR} (dark blue) and hybrid Σ_{SFR} (orange) as a function of galactocentric radius. (e) Ratio \mathcal{R} of radio to hybrid Σ_{SFR} . Open symbols represent the non-thermal RC emission alone. (f) Predicted thermal RC fraction.

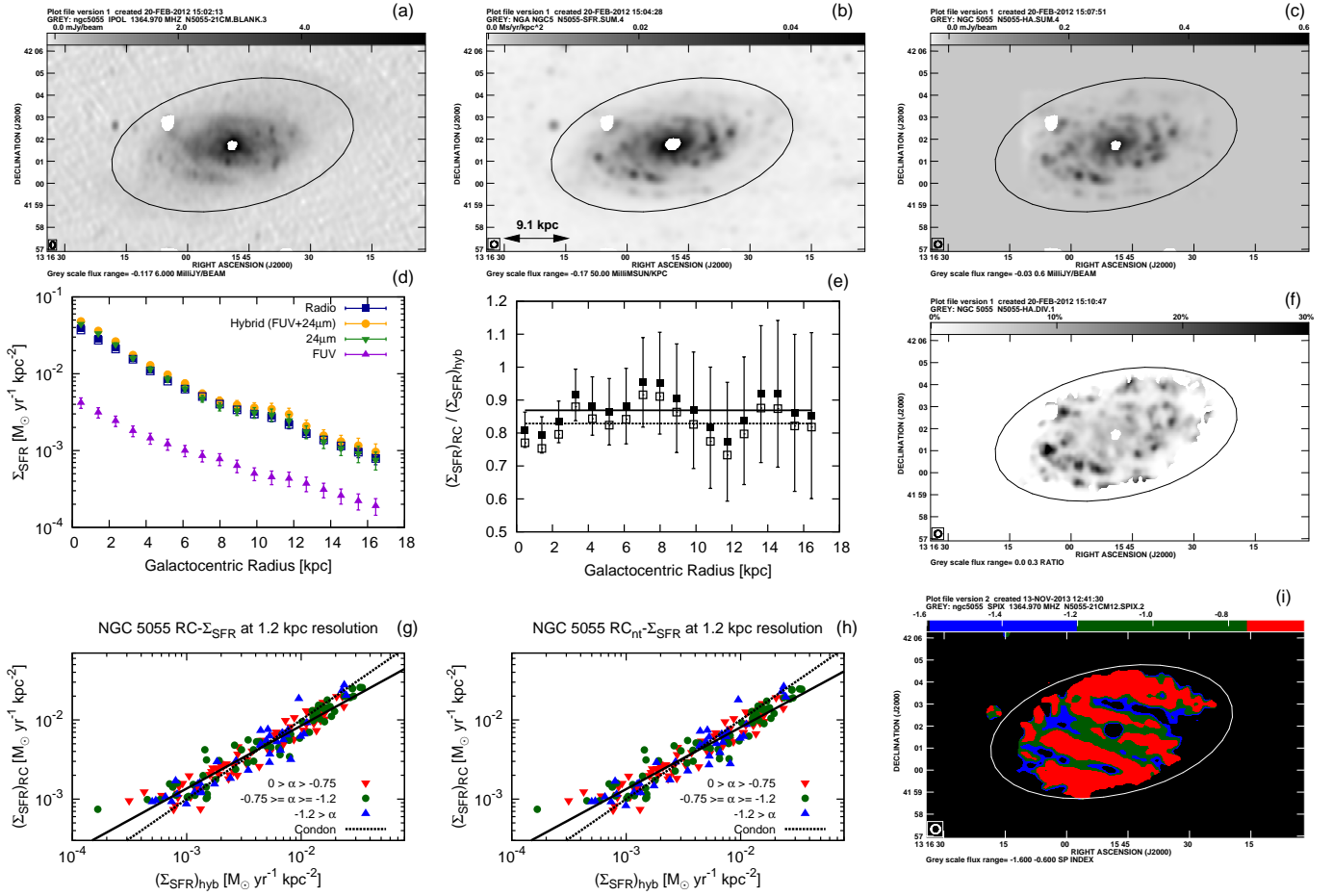


Figure 27. NGC 5055. (a) RC emission at $\lambda 22$ cm. (b) Hybrid SFR surface density $(\Sigma_{\text{SFR}})_{\text{hyb}}$. (c) Thermal RC emission as derived from H α . (d) Radio Σ_{SFR} (dark blue) and hybrid Σ_{SFR} (orange) as a function of galactocentric radius. (e) Ratio \mathcal{R} of radio to hybrid Σ_{SFR} . Open symbols represent the non-thermal RC emission alone. (f) Predicted thermal RC fraction. (g) Radio Σ_{SFR} as a function of hybrid Σ_{SFR} at 1.2 kpc resolution. (h) Same as (g) but with thermal emission subtracted. (i) Radio spectral index at 1.2 kpc resolution. The typical uncertainty of the radio spectral index is 1.2, 0.3, and 0.1 for radio Σ_{SFR} of 2×10^{-3} , 8×10^{-3} , and $3 \times 10^{-2} M_{\odot} \text{ yr}^{-1} \text{ kpc}^{-2}$, respectively.

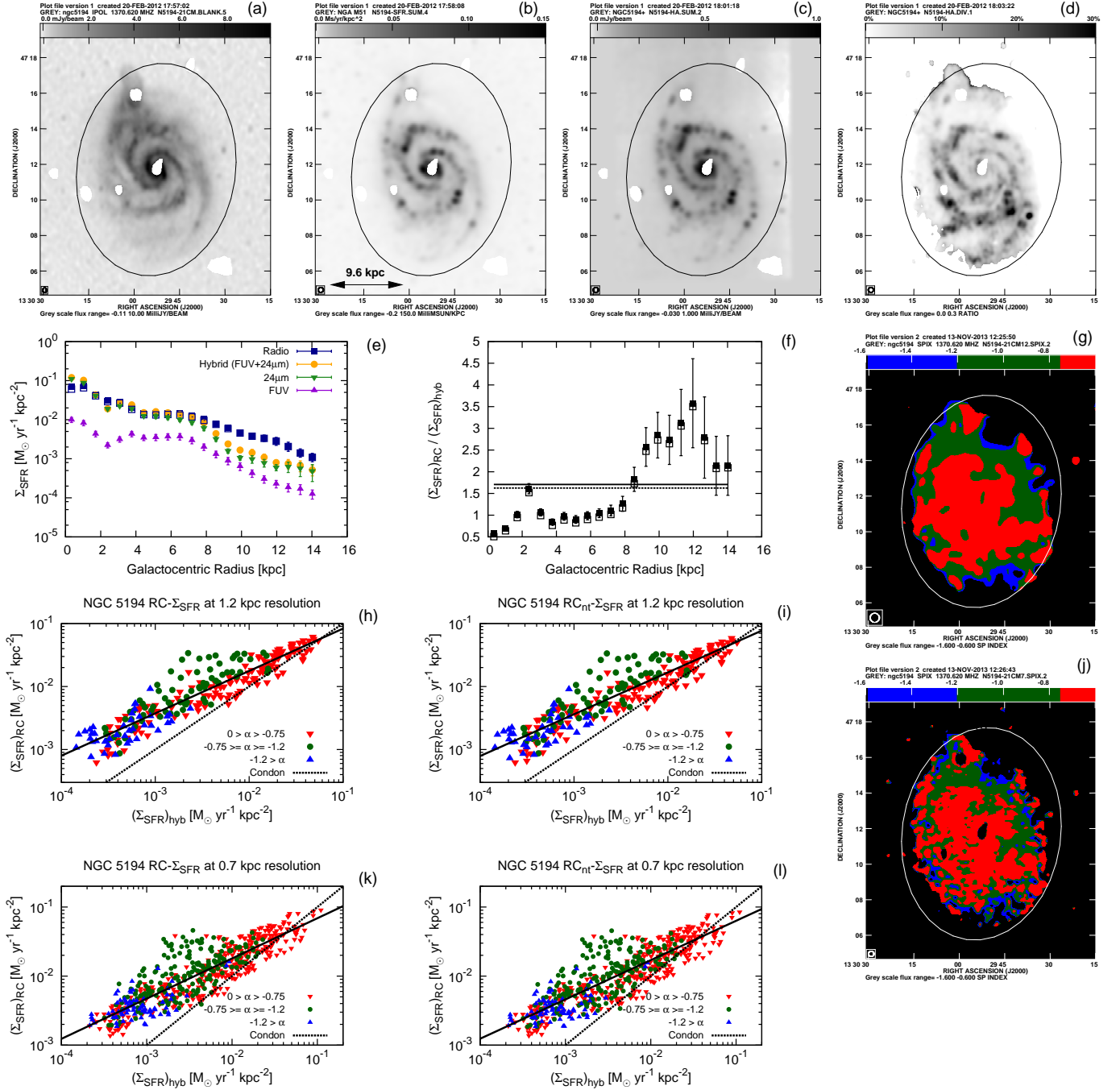


Figure 28. NGC 5194. (a) RC emission at $\lambda 22$ cm. (b) Hybrid SFR surface density ($\Sigma_{\text{SFR}}_{\text{hyb}}$). (c) Thermal RC emission as derived from H α . (d) Predicted thermal RC fraction. (e) Radio Σ_{SFR} (dark blue) and hybrid Σ_{SFR} (orange) as a function of galactocentric radius. (f) Ratio \mathcal{R} of radio to hybrid Σ_{SFR} . Open symbols represent the non-thermal RC emission alone. (g) Radio spectral index at 1.2 kpc resolution. (h) Radio Σ_{SFR} as a function of hybrid Σ_{SFR} at 1.2 kpc resolution. (i) Same as (h) but with thermal emission subtracted. (j–l) Same as (g–i) but at 0.7 kpc resolution. The typical uncertainty of the radio spectral index is 0.8, 0.2, and 0.1 for the blue, green, and red data points, respectively.

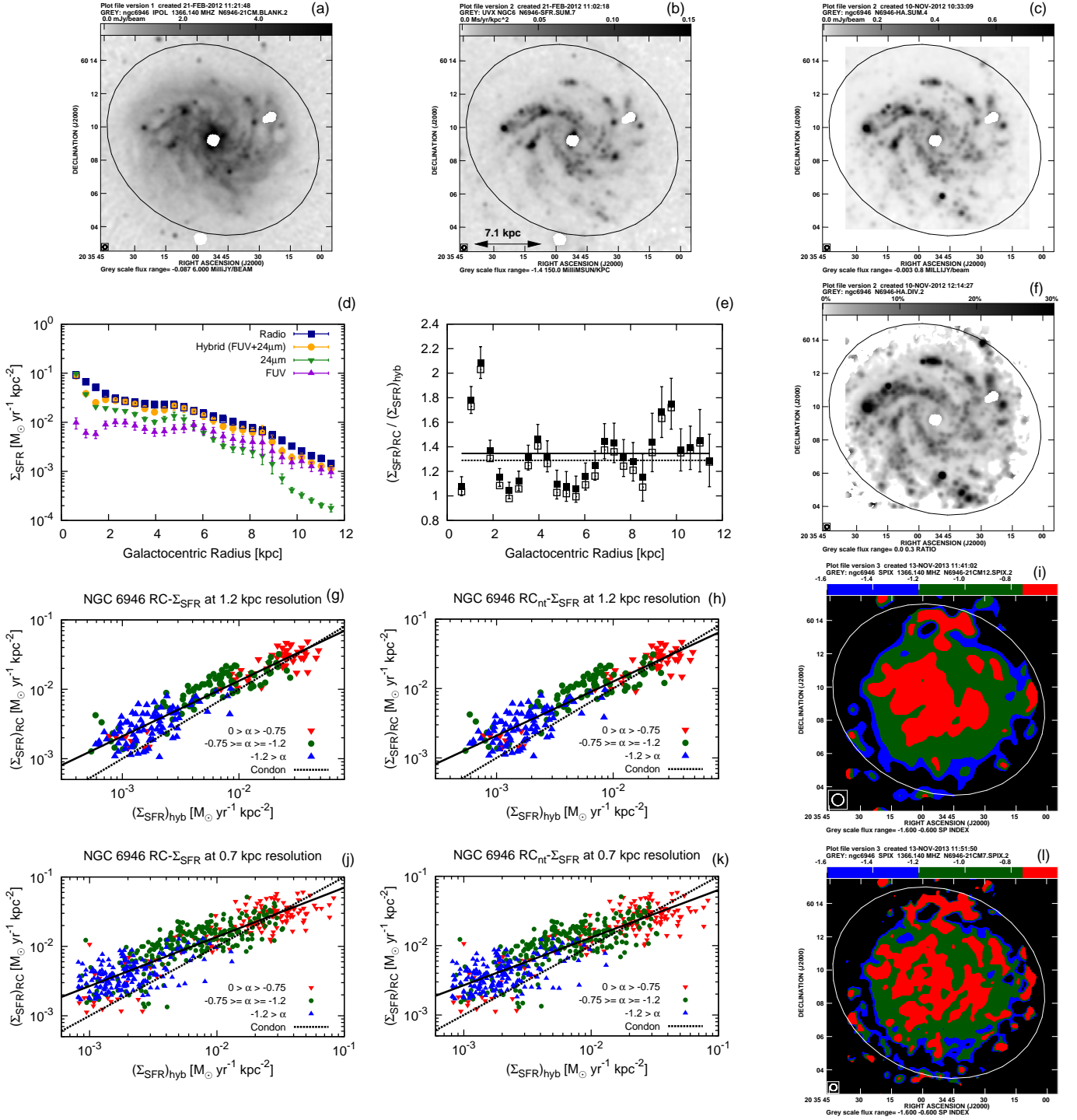


Figure 29. NGC 6946. (a) RC emission at $\lambda 22$ cm. (b) Hybrid SFR surface density ($\Sigma_{\text{SFR}}_{\text{hyb}}$). (c) Thermal RC emission as derived from $\text{H}\alpha$. (d) Radio Σ_{SFR} (dark blue) and hybrid Σ_{SFR} (orange) as a function of galactocentric radius. (e) Ratio \mathcal{R} of radio to hybrid Σ_{SFR} . Open symbols represent the non-thermal RC emission alone. (f) Predicted thermal RC fraction. (g) Radio Σ_{SFR} plotted against hybrid Σ_{SFR} at 1.2 kpc resolution. (h) Same as (g) but with thermal emission subtracted. (i) radio spectral index at 1.2 kpc resolution. (j–l) Same as (g–i) but at 0.7 kpc resolution. The typical uncertainties for the radio spectral index are 0.4, 0.2, and 0.1 for the blue, green, and red data points respectively.

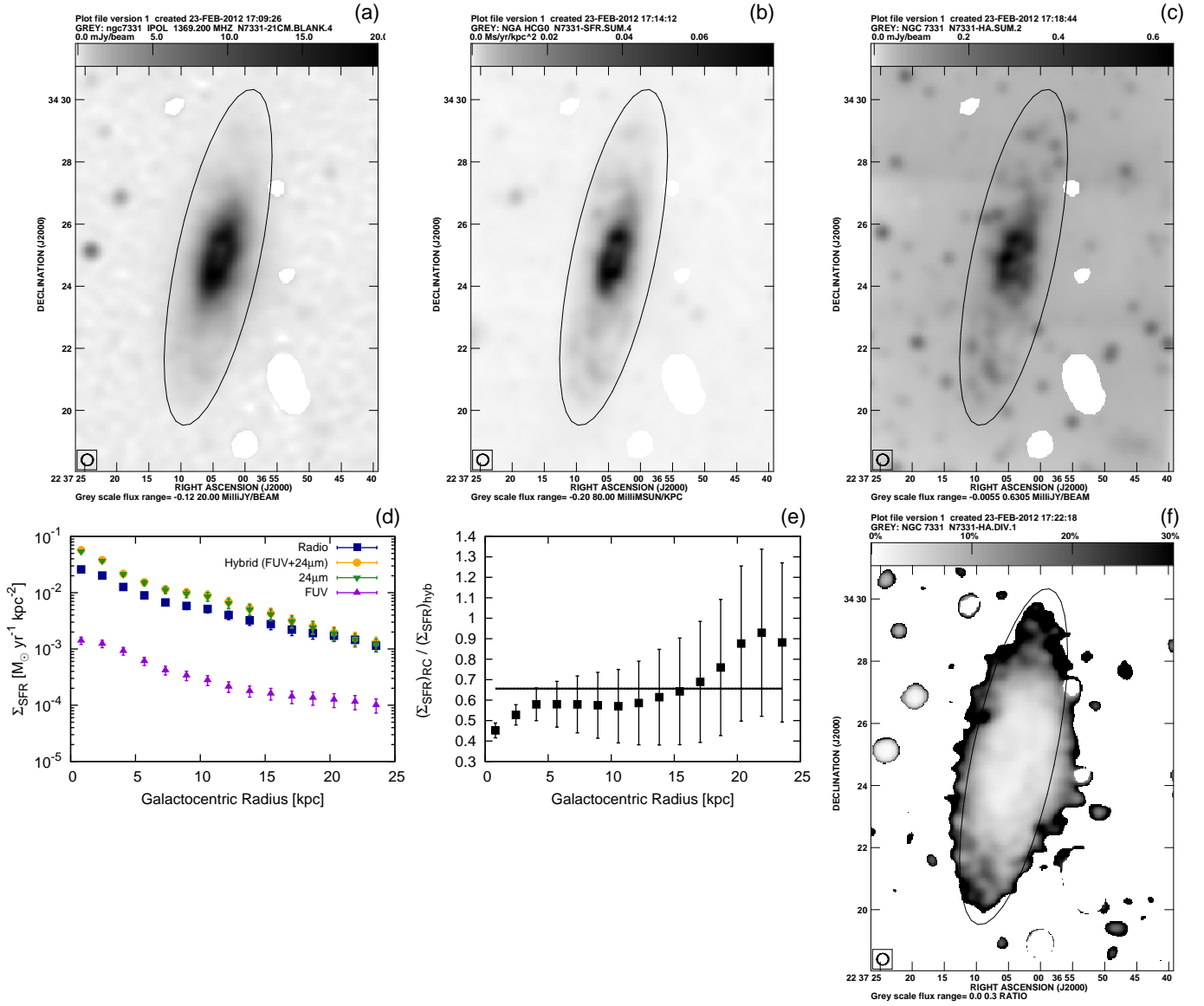


Figure 30. NGC 7331. (a) RC emission at 122 cm. (b) Hybrid SFR surface density ($\Sigma_{\text{SFR}}_{\text{hyb}}$). (c) Thermal RC emission as derived from H α . (d) Radio Σ_{SFR} (dark blue) and hybrid Σ_{SFR} (orange) as function of galactocentric radius. (e) Ratio \mathcal{R} of radio to hybrid Σ_{SFR} . Open symbols represent the non-thermal RC emission alone. (f) Predicted thermal RC fraction.

REFERENCES

- Adebahr, B., Krause, M., Klein, U., et al. 2013, *A&A*, 555, A23
- Adriani, O., Barbarino, G. C., Bazilevskaya, G. A., et al. 2011, *PhRvL*, 106, 201101
- Beck, R. 2001, *SSRv*, 99, 243
- Beck, R. 2007, *A&A*, 470, 539
- Beck, R., Brandenburg, A., Moss, D., Shukurov, A., & Sokoloff, D. 1996, *ARA&A*, 34, 155
- Beck, R., & Krause, M. 2005, *AN*, 326, 414
- Bell, E. F. 2003, *ApJ*, 586, 794
- Berkhuijsen, E. M., Beck, R., & Tabatabaei, F. S. 2013, *MNRAS*, 435, 1598
- Beuermann, K., Kanbach, G., & Berkhuijsen, E. M. 1985, *A&A*, 153, 17
- Bicay, M. D., Helou, G., & Condon, J. J. 1989, *ApJ*, 338, L53
- Bigiel, F., Leroy, A., Seibert, M., et al. 2010, *ApJ*, 720, L31
- Bigiel, F., Leroy, A., Walter, F., et al. 2008, *AJ*, 136, 2846
- Braun, R., Heald, G., & Beck, R. 2010, *A&A*, 514, A42
- Braun, R., Oosterloo, T. A., Morganti, R., Klein, U., & Beck, R. 2007, *A&A*, 461, 455
- Buffie, K., Heesen, V., & Shalchi, A. 2013, *ApJ*, 764, 37
- Calzetti, D., Kennicutt, R. C., Engelbracht, C. W., et al. 2007, *ApJ*, 666, 870
- Cho, J., Vishniac, E. T., Beresnyak, A., Lazarian, A., & Ryu, D. 2009, *ApJ*, 693, 1449
- Chyży, K. T. 2008, *A&A*, 482, 755
- Chyży, K. T., Weżgowiec, M., Beck, R., & Bomans, D. J. 2011, *A&A*, 529, A94
- Condon, J. J. 1992, *ARA&A*, 30, 575
- Condon, J. J., Cotton, W. D., & Broderick, J. J. 2002, *AJ*, 124, 675
- de Blok, W. J. G., Walter, F., Brinks, E., et al. 2008, *AJ*, 136, 2648
- Deeg, H.-J., Duric, N., & Brinks, E. 1997, *A&A*, 323, 323
- Draine, B. T. 2011, *Physics of the Interstellar and Intergalactic Medium*, Princeton, NJ: Princeton Univ. Press
- Draine, B. T., Dale, D. A., Bendo, G., et al. 2007, *ApJ*, 663, 866
- Dumas, G., Schinnerer, E., Tabatabaei, F. S., et al. 2011, *AJ*, 141, 41
- Engelbracht, C. W., Blaylock, M., Su, K. Y. L., et al. 2007, *PASP*, 119, 994
- Ferguson, A. M. N., Gallagher, J. S., & Wyse, R. F. G. 1998, *AJ*, 116, 673
- Galametz, M., Kennicutt, R. C., Calzetti, D., et al. 2013, *MNRAS*, 431, 1956
- Gil de Paz, A., Boissier, S., Madore, B. F., et al. 2007, *ApJS*, 173, 185
- Green, D. A. 2009, *BASI*, 37, 45
- Haslam, C. G. T., Salter, C. J., Stoffel, H., & Wilson, W. E. 1982, *A&AS*, 47, 1
- Heald, G., Braun, R., & Edmonds, R. 2009, *A&A*, 503, 409
- Heesen, V., Beck, R., Krause, M., & Dettmar, R.-J. 2009a, *A&A*, 494, 563
- Heesen, V., Beck, R., Krause, M., & Dettmar, R.-J. 2011, *A&A*, 535, A79
- Heesen, V., Krause, M., Beck, R., & Dettmar, R.-J. 2009b, *A&A*, 506, 1123
- Heger, A., Fryer, C. L., Woosley, S. E., Langer, N., & Hartmann, D. H. 2003, *ApJ*, 591, 288
- Helou, G., & Bicay, M. D. 1993, *ApJ*, 415, 93
- Högbom, J. A. 1974, *A&AS*, 15, 417
- Hoopes, C. G., Waltherbos, R. A. M., & Bothun, G. D. 2001, *ApJ*, 559, 878
- Kennicutt, R. C., & Evans, N. J. 2012, *ARA&A*, 50, 531
- Kennicutt, Jr., R. C. 1983, *ApJ*, 272, 54
- Kennicutt, Jr., R. C., Armus, L., Bendo, G., et al. 2003, *PASP*, 115, 928
- Kennicutt, Jr., R. C., Calzetti, D., Walter, F., et al. 2007, *ApJ*, 671, 333
- Kennicutt, Jr., R. C., Lee, J. C., Funes, José G., et al. 2008, *ApJS*, 178, 247
- Krause, M. 2009, *RMxAC* 36, 25
- Krause, M. 2011, in *Proceedings of Magnetic Fields in the Universe: From Laboratory and Stars to Primordial Structures*, ed. M. Soida, K. Otmianowska-Mazur, E. M. de Gouveia Dal Pino & A. Lazarian (arXiv:1111.7081)
- Lacki, B. C., & Beck, R. 2013, *MNRAS*, 430, 3171
- Lacki, B. C., & Thompson, T. A. 2010, *ApJ*, 717, 196
- Lacki, B. C., Thompson, T. A., & Quataert, E. 2010, *ApJ*, 717, 1
- Leroy, A. K., Bigiel, F., de Blok, W. J. G., et al. 2012, *AJ*, 144, 3
- Leroy, A. K., Walter, F., Bigiel, F., et al. 2009, *AJ*, 137, 4670
- Leroy, A. K., Walter, F., Brinks, E., et al. 2008, *AJ*, 136, 2782
- Leverenz, H., & Filipović, M. D. 2013, *Ap&SS*, 343, 301
- Lisenfeld, U., Voelk, H. J., & Xu, C. 1996, *A&A*, 306, 677
- Lisenfeld, U., & Völk, H. J. 2000, *A&A*, 354, 423
- Mao, S. A., McClure-Griffiths, N. M., Gaensler, B. M., et al. 2012, *ApJ*, 759, 25
- Mathis, J. S., Mezger, P. G., & Panagia, N. 1983, *A&A*, 128, 212
- Moustakas, J. 2006, PhD thesis, The Univ. of Arizona, U.S.A.
- Murphy, E. J. 2009, *ApJ*, 706, 482
- Murphy, E. J., Braun, R., Helou, G., et al. 2006a, *ApJ*, 638, 157
- Murphy, E. J., Condon, J. J., Schinnerer, E., et al. 2011, *ApJ*, 737, 67
- Murphy, E. J., Helou, G., Braun, R., et al. 2006b, *ApJ*, 651, L111
- Murphy, E. J., Helou, G., Kenney, J. D. P., Armus, L., & Braun, R. 2008, *ApJ*, 678, 828
- Murphy, E. J., Porter, T. A., Moskalenko, I. V., Helou, G., & Strong, A. W. 2012, *ApJ*, 750, 126
- Niklas, S. 1995, PhD thesis, Univ. of Bonn, Germany
- Niklas, S., & Beck, R. 1997, *A&A*, 320, 54
- Niklas, S., Klein, U., & Wielebinski, R. 1997, *A&A*, 322, 19
- Paglionie, T. A. D., & Abrahams, R. D. 2012, *ApJ*, 755, 106
- Rephaeli, Y., Arieli, Y., & Persic, M. 2010, *MNRAS*, 401, 473
- Sánchez-Gallego, J. R., Knapen, J. H., Wilson, C. D., et al. 2012, *MNRAS*, 422, 3208
- Sanders, D. B., Mazzarella, J. M., Kim, D.-C., Surace, J. A., & Soifer, B. T. 2003, *AJ*, 126, 1607
- Sault, R. J., Teuben, P. J., & Wright, M. C. H. 1995, in *ASP Conf. Ser. 77, Astronomical Data Analysis Software and Systems IV*, ed. R. A. Shaw, H. E. Payne, & J. J. E. Hayes (San Francisco, CA: ASP), 433
- Schlegel, D. J., Finkbeiner, D. P., & Davis, M. 1998, *ApJ*, 500, 525
- Schleicher, D. R. G., & Beck, R. 2013, *A&A*, 556, A142
- Shikaze, Y., Haino, S., Abe, K., et al. 2007, *APH*, 28, 154
- Strong, A. W., Orlando, E., & Jaffe, T. R. 2011, *A&A*, 534, A54
- Sun, X. H., Reich, W., Waelkens, A., & Enßlin, T. A. 2008, *A&A*, 477, 573
- Tabatabaei, F. S., Beck, R., Krause, M., et al. 2007a, *A&A*, 466, 509
- Tabatabaei, F. S., Beck, R., Krügel, E., et al. 2007b, *A&A*, 475, 133
- Tabatabaei, F. S., Berkhuijsen, E. M., Frick, P., Beck, R., & Schinnerer, E. 2013a, *A&A*, 557, A129
- Tabatabaei, F. S., Krause, M., & Beck, R. 2007c, *A&A*, 472, 785
- Tabatabaei, F. S., Schinnerer, E., Murphy, E. J., et al. 2013b, *A&A*, 552, A19
- Tammann, G. A. 1982, in *NATO ASIC Proc. 90, Supernovae: A Survey of Current Research*, ed. M. J. Rees & R. J. Stoneham (Dordrecht: Reidel), 371
- Thilker, D. A., Bianchi, L., Boissier, S., et al. 2005, *ApJ*, 619, L79
- Thompson, T. A., Quataert, E., Waxman, E., Murray, N., & Martin, C. L. 2006, *ApJ*, 645, 186
- Völk, H. J. 1989, *A&A*, 218, 67
- Walter, F., Brinks, E., de Blok, W. J. G., et al. 2008, *AJ*, 136, 2563
- Wilson, C. D., Warren, B. E., Israel, F. P., et al. 2012, *MNRAS*, 424, 3050
- Yost-Hull, T. M., Everett, J. E., Gallagher, III, J. S., & Zweibel, E. G. 2013, *ApJ*, 768, 53